POLITECNICO DI TORINO

Collegio di Ingegneria Chimica e dei Materiali

Master of Science Course in Chemical and Sustainable Processes Engineering

Master of Science Thesis

Safety distances estimation for hydrogen blended natural gas jet fires using neural network methods



Tutors Candidate

Prof. Micaela Demichela

Prof. Alba Àgueda Costafreda

Giovanni Nalin

A.a 2024/2025 Section of October 2025

Abstract

The global trend towards hydrogen as a key low-carbon energy vector is rapidly increasing worldwide, due to its high gravimetric energy density. Following this current, there were analysed different ways to produce it, overall, the ones powered by renewable energy sources (green H₂), which represents a bridge between today and a zero-emission future. All the types of H₂ could be transported with several strategies and in different forms, for example in trucks through liquid or compressed gas state. However, these last two methods need sophisticated structures and elevated costs. At the same time, existing natural gas (NG) transmission and distribution pipelines represent a vast infrastructure that could carry hydrogen blended natural gas (HBNG) over long distances more economically than pure hydrogen pipelines too. Indeed, blending hydrogen into NG networks avoids massive costs for new infrastructures, but raises questions about mixing behaviour, energy transmission, compressor work and material integrity, particularly due to hydrogen embrittlement (HE) of steels under high pressure.

HE could be the cause of HBNG leaks from a pressurized pipeline or vessel, and the small molecular size and low ignition energy of hydrogen can lead rapidly to turbulent jet flames. These high-momentum diffusion flames emit heat that can impinge on nearby structures and can trigger catastrophic domino events. Their behaviour is studied nowadays, because the presence of H₂ modifies which could be the classic NG one. Accurate prediction of jet-fire flame geometry (length and lift-off) and radiative heat flux is therefore essential for defining safe separation distances. PHAST is a simulating software with semi-empirical models implemented that could offer optimal prevision of HBNG jet fires, Configurating these type of scenarios in simulative software like PHAST could be really useful, for evaluating the jet fire mass flowrate, the flame length and the safety distances and to study the influence of parameters such as orifice diameter, storage temperature and pressure, meteorological conditions and the volumetric concentration of the blended hydrogen.

In this work, a Neural Network (NN) is developed to estimate the effects of jet fires. Firstly, jet fire scenarios of HBNG from transmission pipeline were simulated using PHAST software. A database was constructed by configuring accidental jet fire scenarios for obtaining the jet fire mass flowrate, the flame length and the safety distances (Alert zone, Intervention zone, Domino Effect zone) for different combinations of input parameters such as orifice diameter, storage

temperature and pressure, meteorological conditions and volumetric concentration of the blended hydrogen. A pseudo-validation was performed to ensure that PHAST could be used for the specific ranges of parameters and compared to literature experimental cases. Before developing the NN, the database results are analysed and standardized, as pre-processing steps. A Multilayer Feedforward Neural Network with Backpropagation was trained and optimized on the database constructed and the hyperparameters were tuned to minimize the loss function. MAE, MSE and R² metrics were used to evaluate the performance. In the end the optimized version of this NN model could successfully reproduce the original database with MSE errors in the millesimal range.

Astratto

La tendenza globale verso l'idrogeno come un vettore energetico chiave a basse emissioni sta aumentando rapidamente in tutto il mondo, grazie alla sua elevata densità energetica gravimetrica. Seguendo questa tendenza, sono stati analizzati diversi metodi per produrlo, soprattutto quelli alimentati da fonti energetiche rinnovabili (H2 verde), che rappresentano un ponte tra il presente e un futuro a senza emissioni. I vari tipi di H2 potrebbero essere trasportati con diverse strategie e in diverse forme, ad esempio su camion allo stato liquido od in forma di gas compresso. Tuttavia, questi ultimi due metodi richiedono strutture sofisticate ed hanno costi elevati. Allo stesso tempo, il già esistente sistema di condutture per il trasporto e la distribuzione del gas naturale (GN) rappresenta una vasta infrastruttura che potrebbe trasportare gas naturale miscelato con idrogeno (HBNG) anche su lunghe distanze, in maniera più economica rispetto alla distribuzione di idrogeno puro. Infatti, la miscelazione dell'idrogeno nelle reti di GN evita i costi ingenti legati alla costruzione di nuove infrastrutture, ma solleva interrogativi sul comportamento della miscela, sulla trasmissione di energia, sul funzionamento dei compressori e sull'integrità dei materiali, in particolare a causa dell'infragilimento da idrogeno (HE) degli acciai ad alta pressione.

HE potrebbe essere la causa di perdite di HBNG da una tubazione o da un serbatoio pressurizzato, e le piccole dimensioni molecolari, insieme alla bassa energia di accensione dell'idrogeno possono portare rapidamente a fiamme turbolenti a getto. Queste fiamme a diffusione ad alto momento emettono calore che può incidere sulle strutture vicine e innescare catene di eventi catastrofici. Il loro comportamento è oggetto di studio al giorno d'oggi, perché la presenza di H₂ modifica quello che potrebbe essere il classico comportamento del NG. Una previsione accurata della geometria della fiamma a getto (lunghezza e sollevamento) e del flusso di calore radiativo sono quindi essenziali per definire le distanze di sicurezza. PHAST è un software di simulazione con modelli semi-empirici implementati che potrebbe offrire una previsione ottimale delle fiamme composte da HBNG. Configurare questo tipo di scenari in un software di simulazione come PHAST potrebbe essere davvero utile per valutare la portata massica della fiamma, la sua lunghezza e le distanze sopracitate e per studiare l'influenza di parametri quali il diametro dell'orifizio, la temperatura e la pressione di stoccaggio, le condizioni meteorologiche e la concentrazione volumetrica dell'idrogeno miscelato.

In questo lavoro è stata sviluppata una rete neurale (NN) per stimare gli effetti delle fiamme a getto. Innanzitutto, sono stati simulati scenari di lingue di fuoco di HBNG da condotti di trasmissione utilizzando il software PHAST. È stato creato un database configurando differenti scenari accidentali per ottenere la portata massica del getto, la lunghezza della fiamma e le distanze di sicurezza (zona di allerta, zona di intervento, zona di effetto domino) per diverse combinazioni di input quali diametro dell'orifizio, temperatura e pressione di stoccaggio, condizioni meteorologiche e concentrazione volumetrica dell'idrogeno miscelato. È stata eseguita una pseudo-convalida per confermare che PHAST potesse essere utilizzato per intervalli specifici di questi parametri ed è stata confrontata con casi sperimentali trovati in letteratura. Prima di sviluppare la NN, i risultati del database sono stati analizzati e standardizzati, nella fase di antecedente all'elaborazione. Una rete neurale feedforward multistrato con retro-propagazione è stata addestrata e ottimizzata sul database costruito e gli iper-parametri sono stati regolati per minimizzare la funzione di perdita. Per valutare le prestazioni sono state utilizzate le metriche MAE, MSE e R₂. Alla fine, la versione ottimizzata di questo modello NN è riuscita a riprodurre con successo il database originale con errori MSE nell'ordine dei millesimi.

Resumen

La tendencia global hacia el hidrógeno como vector energético clave y bajo en carbono está aumentando rápidamente en todo el mundo, en parte debido a su alta densidad energética gravimétrica. Siguiendo esta corriente, se han analizado diferentes métodos para su producción, especialmente aquellos impulsados por fuentes de energía renovables. El hidrógeno producido, posteriormente, se transporta siguiendo diversas estrategias y en distintas formas, como en estado líquido o como gas comprimido. Sin embargo, estos dos últimos métodos requieren estructuras sofisticadas y costes elevados. Al mismo tiempo, las redes existentes de transporte y distribución de gas natural (GN) representan una vasta infraestructura que podría utilizarse para transportar gas natural mezclado con hidrógeno (HBNG por sus siglas en inglés) a largas distancias de forma más económica que mediante tuberías exclusivas para hidrógeno. De hecho, mezclar hidrógeno en las redes de GN evita costes masivos asociados a nuevas infraestructuras, pero plantea cuestiones sobre el comportamiento de la mezcla, la transmisión de energía, el trabajo de los compresores y la integridad de los materiales, especialmente debido al fenómeno de fragilización por hidrógeno de los aceros a alta presión.

El fenómeno de fragilización por hidrógeno podría ser la causa de fugas de HBNG desde una tubería o recipiente presurizado, y el pequeño tamaño molecular y la baja energía de ignición del hidrógeno pueden provocar rápidamente la formación de llamas turbulentas de tipo dardo de fuego. Estas llamas de difusión de alto momento emiten calor que puede impactar en estructuras cercanas y desencadenar eventos catastróficos en cadena. Su comportamiento está siendo actualmente estudiado, ya que la presencia de H2 modifica el que sería el comportamiento clásico del GN. Por tanto, la predicción precisa de la geometría de los dardos de fuego (longitud y altura de elevación) y del flujo de calor radiactivo es esencial para definir las distancias de seguridad. PHAST es un software comercial con modelos semi-empíricos implementados que puede ofrecer una predicción óptima de los dardos de fuego de HBNG. Configurar este tipo de escenarios en PHAST puede ser muy útil para evaluar el caudal másico del dardo, la longitud de la llama y las distancias de seguridad, así como para estudiar la influencia de parámetros como el diámetro del orificio, la temperatura y presión de almacenamiento, las condiciones meteorológicas y la concentración volumétrica de hidrógeno en la mezcla.

En este trabajo, se desarrolla una Red Neuronal (NN por sus siglas en inglés) para estimar los efectos de los dardos de fuego. En primer lugar, se simularon escenarios de dardos de fuego de HBNG provenientes de tuberías de transmisión utilizando el software PHAST. Se construyó una base de datos configurando escenarios accidentales para obtener el caudal másico, la longitud de la llama y las distancias de seguridad para diferentes combinaciones de parámetros de entrada, como el diámetro del orificio, la temperatura y presión de almacenamiento, las condiciones meteorológicas y la concentración volumétrica de hidrógeno en la mezcla. Se realizó una pseudo-validación para garantizar que PHAST podía utilizarse dentro de los rangos específicos de los parámetros y se comparó con casos experimentales presentes en la literatura. Antes de desarrollar la red neuronal, los resultados de la base de datos fueron analizados y estandarizados como pasos de preprocesamiento. Se entrenó y optimizó una Red Neuronal Feedforward Multicapa (MLFFNN) sobre la base de datos construida, ajustando los iperparámetros para minimizar la función de pérdida. Se utilizaron las métricas MAE, MSE y R² para evaluar su rendimiento. El modelo entrenado fue capaz de reproducir con éxito la base de datos original, con errores MSE en el rango de las milésimas.

Glossary

AZ = Alert Zone

ATR = Autothermal Reforming

BLEVE = Boiling Liquid Expanding Vapor Explosion

 $\mathbf{BP} = \mathbf{Backpropagation}$

CCS = Carbon Capture and Storage

CERTEC = Centre for Technological Risk Studies

CFD = Computational Fluid Dynamics

DL = Deep learning

DNV = Det Norske Veritas

DOT = United States Department of Transportation

DZ = Domino Zone

EA = European Commission

EI = Emission Index

EIA = US Energy Information Administration

ENTSOG = European Network of Transmission System Operators for Gas

EOS = Equation of State

GHG = Greenhouse Gases

GWP = Global Warming Potential

 $H_2 = Hydrogen$

HBNG = Hydrogen Blended Natural Gas

HE = Hydrogen Embrittlement

HEE = Hydrogen-Environment Embrittlement

H2GEU = Hydrogen Grid Entry Unit

HTHA = High Temperature Hydrogen Attack

IEA = International Energy Agency

IZ = Intervention Zone

LHV = Lower Heating Value

LNG = Liquified Natural Gas

LR = Learning rate

 $CH_4 = Methane$

ML = Machine Learning

MLFFNN = Multilayer Feedforward Neural Network

MMPS = Miller Multi Point Source

MSE= Mean Square Error

NG = Natural Gas

NN = Neural Network

NTS = Notched Tensile Strength

PEM = Proton Exchange Membrane

PHAST = Process Hazard Analysis Software Tool

PID = Proportional-integral-derivative

PSA = Pressure Swing Adsorption

 \mathbf{R}^2 = Coefficient of Determination

RBF = Radial Based Functions

ReLU = Rectified Linear Unit

SDG =Sustainable Development Goals

SMR = Steam Methane Reforming

SOEC = Solid Oxide Electrolyte

SRK = Soave-Redlich-Kwong

TEA = Techno Economic Analysis

W = Wobbe Index

Contents

AB	STRA	ACT _		· · · · · · · · · · · · · · · · · · ·
				II
RE	SUM	EN		IV
GL	OSSA	ARY		VI
				VIII
LIS	т оғ	FIGU	URES	XI
LIS	T OF	TARI	LFS	XV
1			LES	
1	1.1		Ogen trends	
	1.1	1.1.1	Global and European hydrogen demand	
		1.1.1	Hydrogen production	
		1.1.2	Hydrogen transportation	
		1.1.3	Hydrogen Blended Natural Gas (HBNG)	
	1.2		ors to consider with HBNG	
	1.2	1.2.1	H ₂ vs. CH ₄	
		1.2.2	Characteristic gas flow and compressibility factor	
		1.2.3	Energy transmission	
		1.2.4	Temperature during pressure drops	
		1.2.5	Hydrogen embrittlement	
	1.3	Jet fir	res	23
		1.3.1	HBNG jet fires	26
		1.3.2	Jet fires simulation	
		1.3.3	Safety distances according to vulnerability	32
	1.4	Neura	al Networks (NN)	33
		1.4.1	Multilayer feedforward neural network (MLFFNN)	35
		1.4.2	Activation transfer functions	
2	OB	JECTI	IVES	38
3			DOLOGY	
	3.1		G jet fires simulation	
		3.1.1	PHAST – Process Hazard Analysis Software Tool	
		3.1.2	·	

REF	FERE	INCES	97
ANI		D: RESULTS OF THE SIMULATION IN PHAST CHANGIN DRAGE TEMPERATURE	
ANI		C: GRID CONSEQUENCES FROM PHAST HBNG JETULATIONS	Γ FIRE 91
		Calculation of radiant heat fraction and radiation characteristics	
		Calculation of flame momentum and lift-off distances	
		Calculation of still air flame length parameters for non-hydrocarbons	
	B.1 S	Source models for pressure vessel leaks	85
ANI	NEX :	B: PHAST MODELS	85
	A.4	Relationship with the Sustainable Development Goals	83
	A.3	Ethical implications	83
	A.2	Economic sustainability	82
	A. 1	Environmental sustainability	81
ANI		A: SUSTAINABILITY REPORT	
5	CO	NCLUSIONS	79
	4.4	Further works	78
	4.3	Optimization results of the MLFFNN with BP model	
	4.2	Performance evaluation of the MLFFNN with Backpropagation	70
	4.1	Simulation in PHAST	
4	RES	SULTS	
	3.8	Optimization of the MLFFNN with BP	
	3.7	NN performance evaluation	
	3.6	Training	
		3.5.3 Setting up the DataLoader	
		3.5.2 NN Architecture	
	٥.٥	3.5.1 Division of the data between training, validation and test	
	3.5	3.4.2 Feature selection and Dataset generation	
		3.4.1 Pre-processing	
	3.4	Database preparation	
	3.3	Database construction	
	3.2	Workflow for designing a NN model	

RINGRAZIAMENTI	102

List of figures

Figure 2. Capture of global H_2 pipelines installed in 2016 (IChemE 2025)
Figure 3. H_2 production alternatives and blended H_2 pathways (Cristello et al. 2023)
Figure 4. Scheme of a typical system for blending H_2 into natural gas grids (Cristello et al 2023).
Figure 5. Simulated transmission and distribution pipelines (Cristello et al. 2023)
Figure 6. Map of the European NG network (Carvalho et al. 2009)
Figure 7. Effect of H_2 admixture on the flow rate (Galyas et al. 2023)
Figure 8. The compressibility factor curves of CH_4 and H_2 (Galyas et al. 2023)
Figure 9. Compressibility factor curves for 20 mol% H_2 concentration case (Galyas et al 2023)
Figure 10. Energy transmission by H_2 concentration in the gas mixture (Cristello et al. 2023)
Figure 11. An example of a domino effect originated from a jet fire (Casal 2018b)24
Figure 12. Variation of NO, NOx, and CO EI with % H ₂ in the mixture (Choudhuri and Gollahalli 2002)28
Figure 13. Flame images of mixture of CH_4 and H_2 with H_2 volume fraction from 0% to 30% at $P = 400$ Pa and. Background grid with a cell size of 0.2 m x 0.15 m (Kong et al. 2024) 29
Figure 14 Jet fire for horizontal jet fire model ((Johnson, Brightwell, and Carsley 1994) 3 I
Figure 15. Miller model flame representation for horizontal jet fires (DNV 2023)
Figure 16. Miller model radiation intensity distribution (DNV 2023)
Figure 17. Feedforward NN (Mashhadimoslem et al. 2023)
Figure 18. A multilayer feedforward neural network (MLFFNN) approach with backpropagation for NN structure (Sun et al. 2020)
Figure 19. Illustration of activation transfer functions. (a) Sigmoid activation function; (b) tank activation function; (c) ReLU activation function (Zhong et al. 2024)
Figure 20. Comparison of the predictions by the Miller and the Cone model in PHAST for horizontal releases of H_2 and H_2 mixtures (DNV 2023)
Figure 21. Comparison of the predictions between the Miller and the Cone models in PHAST for hydrocarbon releases (DNV 2023)
Figure 22. Flame length, fraction of emissivity and frustum lift off distance simulated for 20 mm, 35 mm, 50 mm orifice diameters with four different configurations: a horizontal pressure vessel with a control valve (orange; 1), relief valve (green; 2) or leak (light blue; 3); or a long pipeline with a specific location of the break (purple; 4). The rhomboid points are from Cone

model and the squared ones from Miller one. The black dotted line corresponds to the experimental values
Figure 23. Incident radiation crosswind with four different configurations in PHAST for Cone and Miller models: control valve (pressure vessel), relief valve (pressure vessel), leak (pressure vessel), location specific break (long pipeline). The red markers are the experimental values for each orifice diameter: triangles for 20 mm, squares for 35 mm and circles for 50 mm 47
Figure 24. Predicted/observed value for incident radiations for the following configurations in PHAST: leak, control valve and location specific break in a long pipeline simulated with Cone and Miller model
Figure 25. A schematic view of a NN work cycle model design
Figure 26. Main steps of the workflow for designing a NN model with the Python scripts applied in this research
Figure 27. Particular of the JSON script "all_T.json" created by the merged three excel files obtained by Grid consequence command in PHAST
Figure 28. Particular of "Jet_fire_NN.py" script to show the first architecture of the MLFFNN. 58
Figure 29. Training section of "Jet_fire_NN.py" script
Figure 30. Performance evaluation extract of "Jet_fire_NN.py" script
Figure 31. Release mass flow rate (kg/s) results obtained using PHAST for a setup jet fire with storage pressure of 60 barg and storage temperature of -5 °C considering different orifice diameters (1, 5, 10, 20, 35, 50 mm) and different hydrogen compositions (0, 5, 10, 20, 24, 30% vol.) in methane
Figure 32. Flame length (m) results obtained using PHAST for a setup jet fire with storage pressure of 60 barg and storage temperature of -5 °C considering different orifice diameters (1, 5, 10, 20, 35, 50 mm) and different hydrogen compositions (0, 5, 10, 20, 35, 50% vol.) in methane.
Figure 33. Distance crosswind to intensity level of 3 kW/m² (alert zone), 5 kW/m² (intervention zone), 8 kW/m² (domino effect zone) obtained using PHAST for a setup jet fire with storage pressure of 60 barg and storage temperature of -5 °C considering different orifice diameters (1,5, 10, 20, 35, 50 mm) and different hydrogen compositions (0, 5, 10, 20, 35, 50% vol.) in methane.
Figure 34. Release mass flow rate (kg/s) results obtained using PHAST for a setup jet fire with a hydrogen composition of 24% vol. and a storage temperature of -5 °C considering different orifice diameters (1, 5, 10, 20, 35, 50 mm) and different storage pressures (30, 45, 50, 60, 70, 80, 100, 150 barg).
Figure 35. Flame length (m) results obtained using PHAST for a setup jet fire with a hydrogen composition of 24% vol. and a storage temperature of -5 °C considering different orifice diameters (1, 5, 10, 20, 35, 50 mm) and different storage pressures (30, 45, 50, 60, 70, 80, 100, 150 barg).
Figure 36. Distance crosswind to intensity levels of $3 kW/m^2$ (alert zone), $5 kW/m^2$ (intervention zone), $8 kW/m^2$ (domino effect zone) obtained using PHAST for a setup jet fire with a hydrogen

composition of 24% vol. and a storage temperature of -5 °C considering different orifice diameters (1, 5, 10, 20, 35, 50 mm) and different storage pressures (30, 45, 50, 60, 70, 80, 100, 150 barg)
Figure 37. Extract in Visual Code (Python) of the DataFrame
Figure 38. Extract in Visual Code (Python) of the training calculations for the proposed Neural Network
Figure 39. Scatter plots comparing the true values with the from the first version of NN model with: a) Release mass flow rate (kg/s); b) Flame length (m)
Figure 40. Scatter plots comparing the true values with the from the first version of NN model with: a) Distance (m) crosswind to an intensity level of 3 kW/m^2 ; b) Distance (m) crosswind to an intensity level of 5 kW/m^2 ; c) Distance (m) crosswind to an intensity level of 8 kW/m^2 73
Figure 41 . Scatter plots comparing the true values with the predicted ones from the optimized MLFFNN: a) Release mass flow rate (kg/s); b) Flame length (m)
Figure 42. Scatter plots comparing the true values with the predicted ones from the optimized MLFFNN: a) Distance (m) crosswind to an intensity level of 3 kW/m^2 ; b) Distance (m) crosswind to an intensity level of 5 kW/m^2 c) Distance (m) crosswind to an intensity level of 8 kW/m^2
Figure 43. Energy mix of Spain (EMBER 2024.)
Figure 44. SDGs related to the thesis work
Figure 45. Orifice and atmospheric expansion conditions (DNV 2023)
Figure 46. Jet fire mass rate (kg/s) from the grid consequence results of PHAST simulation of a setup jet fire with storage pressure 60 barg and storage temperature 15 °C (a) and 35 °C (b) at different orifice diameter (10, 20, 35, 50 mm) and different H_2 blended compositions (0, 5, 10, 20, 35, 50 %)
Figure 47. Flame length (m) from the grid consequence results of PHAST simulation of a setup jet fire with storage pressure 60 barg and storage temperature 15° C (a) and 35° C (b) at different orifice diameter (10, 20, 35, 50 mm) and different H_2 blended compositions (0, 5, 10, 20, 35, 50 %)93
Figure 48. Distance crosswind to intensity level 3, 5, 8 kW/m² from the grid consequence results of PHAST simulation of a setup jet fire with storage pressure 60 barg and storage temperature 15°C at different orifice diameter (10, 20, 35, 50 mm) and different H₂ blended compositions (0, 5, 10, 20, 35, 50 %)
Figure 49. Distance crosswind to intensity level 3, 5, 8 kW/m² from the grid consequence results of PHAST simulation of a setup jet fire with storage pressure 60 barg and storage temperature 35°C at different orifice diameter (10, 20, 35, 50 mm) and different H₂ blended compositions (0, 5, 10, 20, 35, 50 %)
Figure 50. Jet fire mass rate (kg/s) from the grid consequence results of PHAST simulation of a setup jet fire with hydrogen blended compositions 24 %vol and storage temperature 15°C (a) and 35°C (b) at different orifice diameter (10, 20, 35, 50 mm) and different storage pressure (30, 45, 50, 60, 70, 80, 100, 150 barg)

Figure 51. Flame length (m) from the grid consequence results of PHAST simulation of a setup jet fire with H_2 blended compositions 24 %vol and storage temperature 15°C (a) and 35°C (b) at different orifice diameter (10, 20, 35, 50 mm) and different storage pressure (30, 45, 50, 60, 70, 80, 100, 150 barg).
Figure 52. Distance crosswind to intensity level 3, 5, $8 kW/m^2$ from the grid consequence results of PHAST simulation of a setup jet fire with H_2 blended compositions 24 %vol and storage temperature 15 °C at different orifice diameter (10, 20, 35, 50 mm) and different storage pressure (30, 45, 50, 60, 70, 80, 100, 150 barg)
Figure 53. Distance crosswind to intensity level 3, 5, $8 kW/m^2$ from the grid consequence results of PHAST simulation of a setup jet fire with H_2 blended compositions 24 %vol and storage temperature 35 °C at different orifice diameter (10, 20, 35, 50 mm) and different storage pressure (30, 45, 50, 60, 70, 80, 100, 150 barg)

List of tables

Table 1. Operating specifications for H_2 pipelines worldwide (Cristello et al. 2023)
Table 2. List of major projects regarding H ₂ blended natural gas transportation (Galyas et al 2023)
Table 3. Examples of H_2 blending systems (Cristello et al. 2023)
Table 4. Pipeline operating conditions (Melaina, Antonia, and Penev 2013). 11
Table 5. Typical NG composition. 13
Table 6. Comparison between H_2 and CH_4 in terms of physical properties at $T=0$ °C and $F=1.0125$ bar (Korb, Kawauchi, and Wachtmeister 2016; Goldmeer and Catillaz 2021; Kurz Lubomirsky, and Bainier 2020)
Table 7. Comparison between H_2 and CH_4 in terms of combustion and energy properties (Kurz et al. 2020)
Table 8. Hydrogen embrittlement (HE) severity and HEE Index ranges (Cristello et al. 2023) 21
Table 9. Hydrogen embrittlement (HE) severity and HEE Index for commercialized materials (Cristello et al. 2023)
Table 10. Several cases of jet fire domino effect in parallel pipelines (Foroughi, Casal, and Pastor 2023).
Table 11. Threshold values (thermal radiation dose or intensity) for IZ, AZ, DZ (Casal 2008) 32
Table 12. Test conditions and key results from (Lowesmith and Hankinson 2012)
Table 13. Atmospheric parameters of the validation case Lowesmith and Hankinson (2013) 43. Atmospheric parameters of the validation case Lowesmith and Hankinson (2013)
Table 14. Possible configurations for jet fires in PHAST depending on the discharge type 43
Table 15. Database design (release parameters): $Cat - categorical; N - Numerical; T - Temperature; P - Pressure; MW - Molecular Weight.$
Table 16. Database design (atmospheric parameters): Cat – categorical; N – N umerical; T – T emperature; P – P ressure; MW – M olecular W eight
Table 17. Statistical metrics (MAE, MSE, R^2) obtained using the weights corresponding to the lowest loss function results in the proposed NN
Table 18. Sensitivity analysis performed on the model definition variables for the MLFNN with BP network used. 74
Table 19. Sensitivity analysis performed on the DataLoader for the MLFNN with BP network used. 75
Table 20. Sensitivity analysis performed on the training loop for the MLFNN with BP network used. 75

Table 21. Equivalent CO ₂ emission per kWh during the morning hours	82
Table 22. Selected values of the Jet fire sheet from the grid consequence of a simular Vessel + Leak with Miller/DNV model setup for HBNG horizontal jet fire cases w.	
parameter in section 3.4.3	_

1 Introduction

1.1 Hydrogen trends

1.1.1 Global and European hydrogen demand

Fossil fuels, which are a primary energy source commonly used nowadays, emit GHG during the combustion process necessary for obtaining their thermal energy. They play a significant role in worldwide climate change. In particular they emit molecules such as CO₂, CH₄ and N₂O, which are capable of absorbing a portion of the infrared radiation emitted by the Earth, becoming the main responsible for global temperature rising and posing a significant hazard to the ecological environment (Filonchyk et al. 2024).

For this reason, in the last years, H_2 has started to be considered an alternative energy vector because it produces zero carbon emissions when it is implemented in combustion and electrochemical processes. It must be consider also for its high gravimetric energy density: according to the International Energy Agency (IEA), the world consumed approximately 70 million tons of H_2 in 2020, and the demand was expected to steadily increase up to 2050 reaching about $80 \cdot 10^{18}$ J of energy (18% of the global energy demand) (IEA 2021).

Following this argument, the European Commission's communication "A Hydrogen Strategy for a Climate-Neutral Europe", published in July 2020, highlights the key role of H₂ in achieving the EU's 2050 decarbonization targets (European Commission 2020). In the mentioned report, H₂ is expected to play a significant role in reducing GHG emissions and in bridging the current gaps in renewable energy storage. One of the most prominent advantages of this gas is that it can be produced via electrolysis powered by electricity from renewables, having a prominent role not only in the decarbonization of fuel system (NG in particular) but also as a cross-sectorial link. Indeed, as an energy vector, it is crucial the opportunity that H₂ offers to avoid the requirements for instantaneous supply-demand balancing thanks to the many possibilities to store it easily at large scale; with promising environmental outcomes if the electricity source can be renewable too.

The growing interest in H₂ was anticipated in the "Clean Planet for All" report, published in November 2018. In this report it was set out the EU's climate-neutral strategic vision that planned to increase the current share of H₂ from less than 2% to 14% of Europe's energy mix

by 2050. Finally, the use of pure H₂ could help the EU achieve its goal of reducing GHG emissions by at least 40% by 2030 compared to 1990 levels (Directorate-General for Climate Action (European Commission) 2019).

Globally, H₂ is increasingly recognized as a pivotal energy vector beyond the European borders (Figure 1). In North America, both the United States and Canada have laid out comprehensive roadmaps to scale up clean H₂ production and deployment, leveraging federal incentives and infrastructure planning (Office Of Energy Efficiency And Renewable Energy 2023). In Asia, China's "2021–2035 Hydrogen Plan" and Japan's "Basic Hydrogen Strategy" set ambitious production and utilization targets, while South Korea plans a huge increase of H₂ fuel-cell vehicles and the country capacity of electrolyzers by 2040. The trend is followed by Australia, Middle East and Asia, and there are also emerging projects in Africa (Remme 2024).

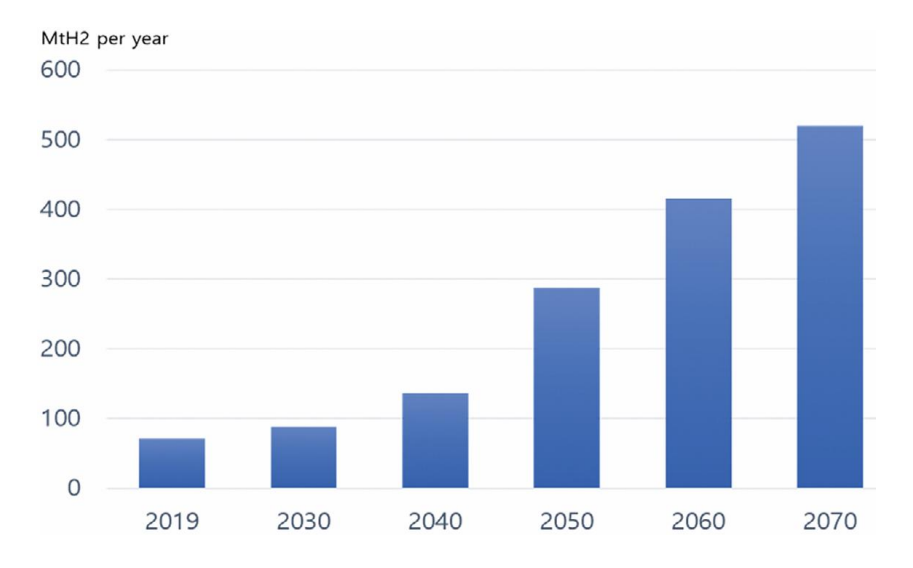


Figure 1. Predicted global H₂ demand (Chae et al. 2022).

1.1.2 Hydrogen production

Hydrogen production can be classified into five categories based on carbon emissions and production methods:

a) **Grey hydrogen** is generated from fossil fuels such as natural gas and coal using Steam Methane Reforming (SMR) or Autothermal Reforming (ATR), both of which emit CO₂. This is the cheapest and most used method, accounting for 76% of global

production and generating 830 Mton of CO₂ per year (Rödl, Wulf, and Kaltschmitt 2018).

- b) **Blue hydrogen** combines the traditional technologies for the grey H₂ with Carbon Capture Utilization and Storage (CCUS) methods. The CO₂ generated during SMR passes through a process of purification, which could be, for example, natural gas (NG) sweeting using various alkanolamines (absorption by MEA, DEA, MDEA) or membrane separation of syngas. Producing H₂ from fossil fuels is likely only appropriate when carbon capture and sequestration opportunities are low-cost and readily available near the site of H₂ production (AlHumaidan et al. 2023).
- c) **Green hydrogen** is produced through the environmentally friendly process of water electrolysis powered by renewable energy sources (mainly wind and Sun). This method generates minimal carbon emissions during production. It uses electricity to split water into H₂ and O₂ via an electrochemical reaction.
- d) **Purple hydrogen** is obtained via electrolysis powered by nuclear energy.
- e) **Proton hydrogen** production involves membrane-based separation applied to oil reservoirs. This technique selectively filters H₂ gas from fossil fuel-based gas mixtures or vapours but requires expensive catalysts, such as platinum.

Among all these methods, low carbon-intensity hydrogens, such as green, purple, or proton H_2 , are essential for achieving long-term carbon neutrality in energy consumption (Speirs et al. 2018). However, while different electrolysis methods exist, including those relying on proton exchange membranes (PEM), alkaline water electrolyzers, and solid oxide electrolyzer cells (SOEC), their high initial investment costs and significant power consumption renders them uneconomical, inefficient and unsuitable for mass adoption (Topolski et al. 2022). The technology is expected to become more profitable as it matures. Estimates suggest that the current cost of H_2 (ranging from $\mathfrak{C}2.20$ to $\mathfrak{C}5.84$ per kilogram) could potentially be reduced to between $\mathfrak{C}0.62$ and $\mathfrak{C}2.30$ per kilogram by 2050 (MacGregor 2025). Additionally, the production of green or purple H_2 requires significantly more water than blue, grey, or proton hydrogen.

Furthermore, the utilization of H₂ as an energy source can be performed via various technologies, such as fuel cells, combustion and mixing with other fuels. However, H₂ suffers a disadvantage in its volumetric energy density, which is only 3 Wh/L, leading to difficulties in

its storage. In order to store H₂ effectively, different H₂ storage technologies could be used, such as compressed and liquefied form, liquid organic carriers or through ammonia (NH₃). In particular this last chemical vessel has high H₂ density (17.8 %wt), as well as high flexibility in its utilization, including mobile and stationary applications. Due to its stability for long-term storage and transportation, ammonia can fulfil the demand to store the energy in time (stationary energy storage) and in space (energy export and import). NH₃ can be utilized by extracting its stored H₂ via thermal cracking or directly utilized as fuel. Another option is direct use as agricultural fertilizer, refrigerant gas and for the manufacture of explosives, pesticides and other chemicals (Aziz, Wijayanta, and Nandiyanto 2020).

1.1.3 Hydrogen transportation

Apart from the production step, the sustainable economic supply of energy for H₂ conversion is dependent on the availability of local resources and the method of transportation. H₂ supply and demand chains are classified as either off-site or on-site, based on the supply, demand locations and production volume. Off-site facilities produce H₂ at a large-scale intermediate H₂ production base, and the produced H₂ is transported to fueling stations by trucks or pipelines. Instead, on-site facilities produce H₂ voluntarily at local factories or fueling stations, which is less efficient but has a lower loss rate during transportation. For this motive, off-site production methods predominate and only a little H₂ is produced at local fueling stations (Rödl, Wulf, and Kaltschmitt 2018).

Nowadays, trucking is one method of transporting H₂, in either its compressed gas (GH₂) or liquid (LH₂) form. However, the low density of H₂ requires it to be pressurized at high pressure to achieve an elevated density energy.

In particular, GH₂ is transported in a tube trailer equipped with a high-pressure storage container on a special vehicle to a H₂ fueling station. It requires relatively high pressures (180 bar or higher) increasing the capital investment associated (Buffi, Prussi, and Scarlat 2022). Moreover, the US Department of Transportation (DOT) regulations on H₂ tube trailer can serve as a comprehensive reference: H₂ compression pressure per unit must not exceed 250 bar, and each trailer is limited to transporting a maximum of 800 kg per trailer (Office Of Energy

Efficiency And Renewable Energy 2023). However, the trucking method may still be efficient for distances under 200 km, especially in areas where alternative means of transport do not exist.

The mass limitation could be resolved by LH₂, which increases the density by a factor of 800, but it requires an energy-intensive liquefaction process and special cryogenic insulated tanks to maintain the necessary low temperatures (Chae et al. 2022).

Among the available options, pipelines are considered the most cost-effective and energy-efficient method for transporting large volumes of H_2 over long distances, with cost estimates ranging from &0.044 to &2.64 per ton, depending on the distance (Buffi, Prussi, and Scarlat 2022). In 2016, more than 4,500 km of H_2 pipelines had been installed around the world (Figure 2).

The initial capital investment associated with H₂ pipeline installation are material costs, labour costs, and interconnection costs. However, typical pipeline materials like steel may be weakened by H₂ due to a phenomenon called embrittlement (see section 1.2.5), which can occur when they are exposed to a high concentration and high-pressure H₂ over an extended period. The risk of H₂ embrittlement necessitates the use of expensive materials, and depending on the pipeline diameter and operating pressure, material costs can be up to 68% higher compared to conventional steel pipelines. Embrittlement also increases the risk of leakage, leading to higher maintenance costs due to the need for pipe replacement. In the end, while pure H₂ pipelines are the most cost-effective option in the long term, they require specialized infrastructure, such as dedicated H₂ pipelines and compressors, and are time-consuming to implement (Chae et al. 2022).

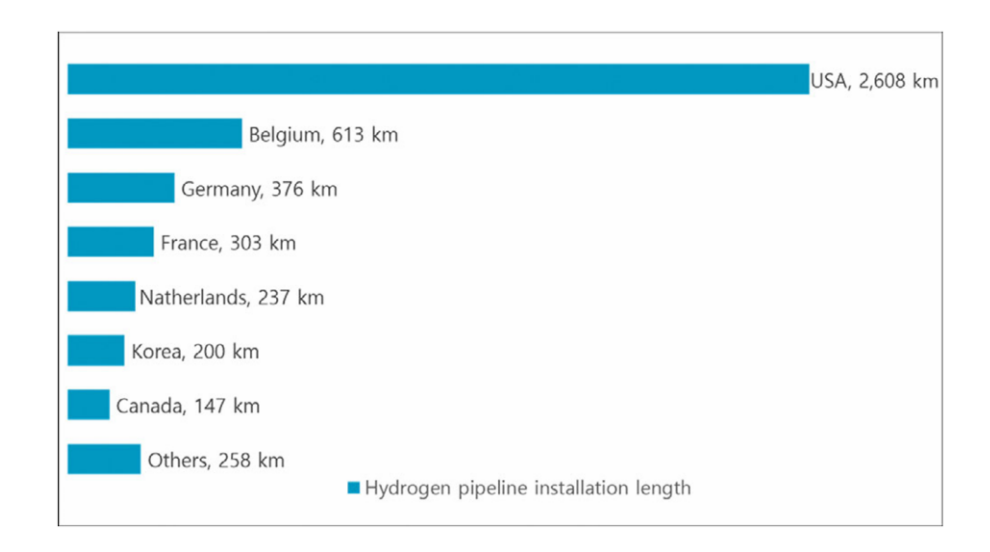


Figure 2. Capture of global H₂ pipelines installed in 2016 (IChemE 2025).

To help contextualizing and providing a practical perspective on the materials and pressures currently being used in H₂ pipelines, Table 1 summarizes the design specifications of H₂ pipelines currently in operation worldwide. These pipelines are usually made of carbon steels with cases where operative pressure reaches 131 bar too.

Table 1. Operating specifications for H₂ pipelines worldwide (Cristello et al. 2023).

Location	Diameter (mm)	Operating pressure (bar)	Material
Texas	150 - 305	24 - 131	Steel Pipe
Westliche	203 - 254	24 - 131	Steel Pipe
Louisiana	150, 203, 305	24 - 131	Steel Pipe
Los Angeles	150, 254, 305	24 - 131	Steel Pipe
Texas	203	24	API 5L Grade B
Texas	36	51	API 5L X60
Netherlands	304.8	65 - 100	Seamless Carbon Steel
Canada	273	38	Gr.290
UK	-	30	Carbon Steel
Germany	-	2 - 5	API 5L L290
France	100	9.7	API 5L X52

1.1.4 Hydrogen Blended Natural Gas (HBNG)

One of the promising solutions to the economical and time-consuming problems of transporting large volumes of pure H₂ over long distances is blending this gas with into the existing NG

pipeline networks. Indeed, blending H₂ produced from low-carbon sources, such as wind and solar energy, into NG could potentially reduce the carbon intensity of difficult-to-decarbonize sectors that are currently served by NG, including peak electricity power production, residential and commercial heating, and industrial processes. As example, in Ontario (Canada) two cases were studied about the economics and emissions of using surplus power to produce electrolytic H₂ to blend and distribute in NG infrastructure. The first one employed buffer storage for H₂ and the second did not. Their results indicated that delivering HBNG to end-users could reduce CO₂ emissions by 9,429 tons with H₂ storage and 3,504 tons without H₂ storage (Mukherjee et al. 2015).

The US Energy Information Administration (EIA) in its 2021 annual Energy Report (U.S. Energy Information Administration 2021) predicted that the supply and demand for NG would steadily increase until 2050, and that pipelines would be used more actively to supply NG. Then, following HBNG alternative strategy and to achieve climate neutrality, several international projects have been launched in recent years. In general, they have examined the possibility of producing, transporting and distributing H₂ in the NG network, as well as H₂ tolerance of currently available gas appliances (see section 3.3). In Europe, for example, to facilitate the transition to the H₂ economy, the European Commission funded the NATURALHY project to study the potential for the existing NG pipeline network to transport H₂ from manufacturing sites to users (NATURALHY 2010).

Table 2. List of major projects regarding H₂ blended natural gas transportation (Galyas et al. 2023).

Project	Country	Objectives	Blended H ₂ (% vol.)
HyDeploy	UK	Blending H ₂ into NG pipelines	20
NATURALHY	Netherlands	Preparing for the H ₂ economy by using the existing NG system as a catalyst	22
Fort Saskatchewan Hydrogen Blending Project	Canada	Blending H ₂ into NG pipelines that serve residential and commercial buildings	5
H21	UK	Investigation of 100 % H ₂ usage with existing natural gas system	100
Hyblend	US	Technical evaluation for blending H ₂ in NG pipelines	-

GRHYD	France	Blending H ₂ into gas distribution lines	20
Snam	Italy	Blending H ₂ into gas transmission lines	10
Enbridge and Cummins Hydrogen- Blending Project	Canada	Blending H_2 into gas distribution lines in Markham, Ontario and performing a routing study	< 2
Hy4Heat	UK	Comprehensive assessment of using hydrogen as a fuel in residential and commercial buildings	100
Hydrogen injection in the gas grid	Denmark	Blending H ₂ into gas distribution and safety evaluation	15
Cleangas Turkey	Turkey	Injecting renewable H ₂ into NG and gas mixture evaluation	20
EN-H ₂	Portugal	Carbon neutralization with the H ₂ economy	15

To achieve this type of transport there are two main methods: on-site method, where NG is used as the feedstock for H_2 production and NG is directly transported to a fuelling station where H_2 is produced; off-site method, where H_2 is produced at its production base, and it can be blended with NG and transported through existing pipelines to H_2 fuelling stations.

 H_2 and NG are separated and purified at intermediate destinations, and then extracted H_2 can be distributed to consumers via the local transportation network for use in fuel cell applications (Figure 3). Also, the end-user may burn the gas mixture directly within existing gas-fired engines, thereby reducing carbon emissions compared to NG (Figure 3).

The implementation of this blending technology requires careful consideration of the H_2 separation and purification processes (Figure 3), as well as any leakage problems that may arise as a result of H_2 embrittlement as mixed gas is pumped through the pipelines (Chae et al. 2022).

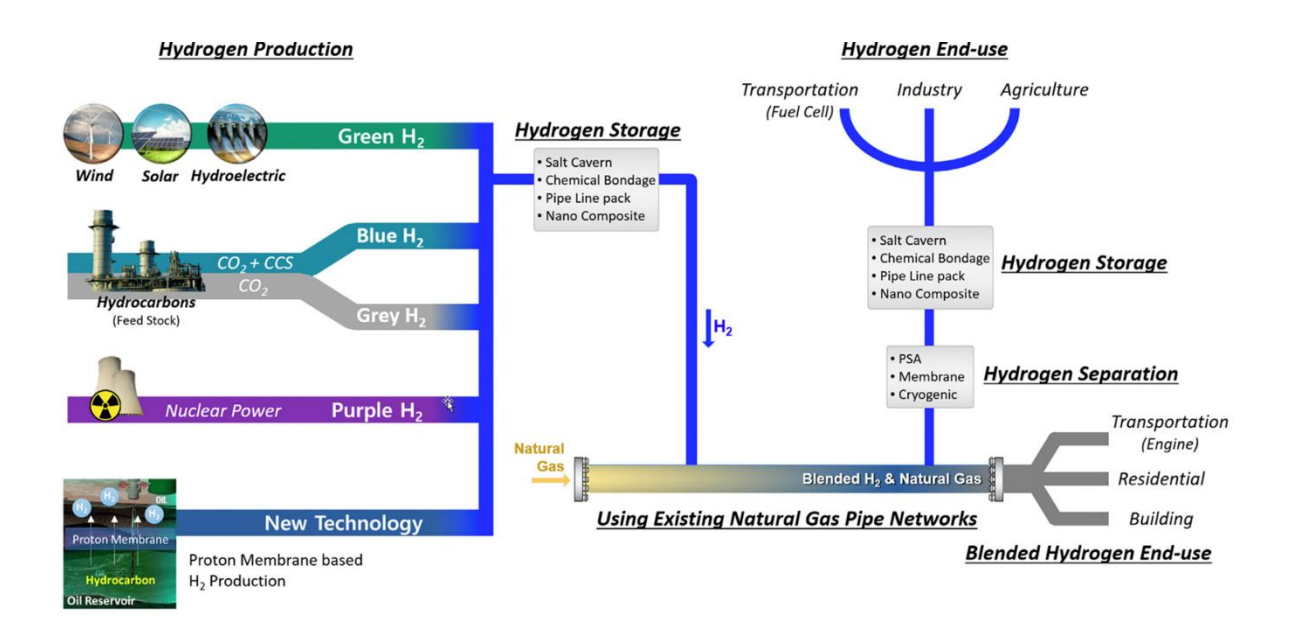


Figure 3. H₂ production alternatives and blended H₂ pathways (Cristello et al. 2023).

A typical system for blending H₂ into NG grids is shown in Figure 4 and it includes an electrolyzer, a H₂ buffer storage tank, and a blending unit. In this process it is important to ensure that HBNG is homogeneous with uniform behaviour along the entire length of the pipeline. If the two gases have significantly different densities, they may stratify, leading to different flow behaviour and leak characteristics. This, in turn, can result in uneven energy distribution and operational challenges with the pipeline (Cristello et al. 2023).

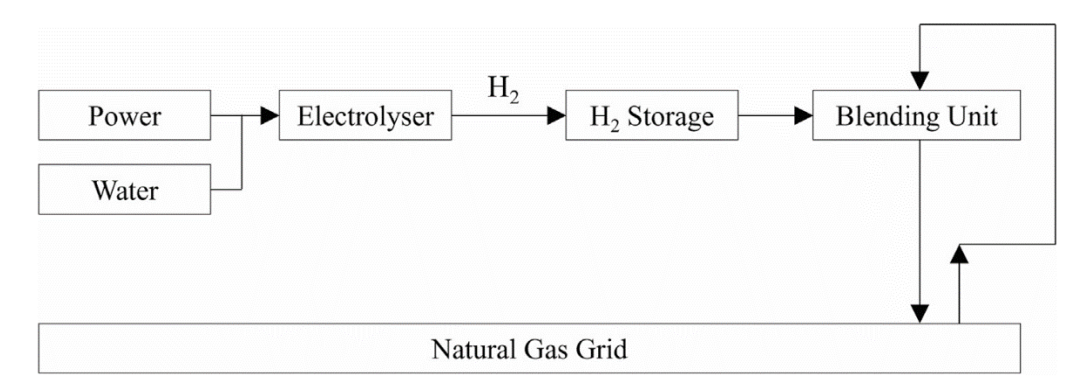


Figure 4. Scheme of a typical system for blending H₂ into natural gas grids (Cristello et al. 2023).

Table 3 lists some of the tried blending systems: in Australia's Hydrogen Park SA project renewable electricity enters the site directly from the local electricity network to power the

electrolyzers. From this one, O₂ is vented and the H₂ purified up to 99% (purity necessary for a fuel cell), by a purification equipment between the electrolyzer and a H₂ buffer tank to remove impurities. Then, H₂ is blended with NG using the gas blending equipment. The blending unit is equipped with a H₂ analyzer located downstream to measure the thermal conductivity of the blended gas, ensuring the H₂ content remains within the allowable limit (Australian Gas Infrastructure Group 2023).

Still in Australia, ATCO's CEIH project blends up to 25% vol. of H₂ using a flow control system with gas chromatography (GC) and a PID controller (ATCO Gas Australia 2019).

In the HyDeploy project, the physical equipment installed was a 0.5 MW electrolyzer, a buffer tank for H₂, a grid entry unit (H2GEU) which mixes the H₂ with incoming NG and sample point around the network to allow monitoring. H2GEU measures the incoming NG Wobbe Index and calculates the amount of H₂ that can be blended while remaining within the Gas Safety Management Regulations. Up to 20 vol% of H₂ is mixed with the NG, and the blended gas passes through a "volume loop" for a composition check before returning to the main feed line. If the blended gas is out of specification, the system automatically reverts to NG and purges the gas out of the specification. Similarly, any process upset triggers a return to NG (Isaac 2019).

All these H₂ blending methods are used to produce developed fully mixed gas mixtures before they are transported through pipelines to prevent gas stratification. When blended gas is transported under turbulent flow conditions, H₂ and NG do not stratify in the pipeline, solving the problem of homogeneity.

Table 3. Examples of H₂ blending systems (Cristello et al. 2023).

Project	Country	Network	Electrolyser Capacity	Blended H ₂ (% vol.)	System
HyP SA	Australia	Distribution	1.2 MW	5	H_2 purification equipment between the electrolyzer and the H_2 buffer tank to remove impurities
ATCO- CEIH	Australia	Distribution	0.15 MW	5 - 25	GC and PID Control in a flow control system
HyDeploy	UK	Distribution	0.5 MW	20	Mixing loop to blend H ₂ with NG before injection into NG grid

In order to examine the potential conversion of an NG pipeline to a HBNG pipeline, two types of pipelines are considered: transmission line and distribution line. As shown in Figure 5, two different lengths are used as reference. In particular, transmission lines generally operate at higher pressures and transport larger volumes over long distances, while distribution lines tend to operate at lower pressures and cover shorter distances. In transmission pipelines, gas is usually transported using centrifugal compressors. The number and location of these compressors are selected to ensure hydraulically stability and safe gas delivery throughout the system.

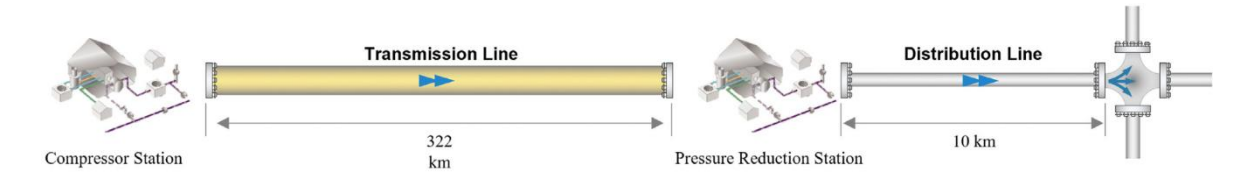


Figure 5. Simulated transmission and distribution pipelines (Cristello et al. 2023).

The operating conditions ranges are provided in Table 4; however, specific values may vary by region and gas provider.

Conditions	Distri	bution	Transmission		
Conditions	Min	Min Max		Max	
Pressure (bar)	0.017	21	41	138	
Temperature (°C)	-6	60	-6	60	

Table 4. Pipeline operating conditions (Melaina, Antonia, and Penev 2013).

Since the density, calorific value, compressibility, and other physical properties of HBNG differ greatly from the originally pure NG (see 1.2.1), this will inevitably affect the economic and environmental performance of the pipeline system. From the economic perspective, the operating costs of the NG pipelines are mainly due to energy consumption of the NG compressor, which is an indispensable active hydraulic component to compensate for the pressure losses during gas flow. Typically, the compressor consumes about 3 - 5% of the transported gas and accounts for about 50% of the overall operating expenses. The energy

consumption of the compressor mainly depends on the compression head, mass flow, and operation efficiency. Due to variations in the properties of the mixed gas, compressor operating parameters (e.g., compression head, efficiency) and energy consumption will change to some extent (B. Zhang et al. 2024).

In the European Union, the twenty-eight Member States are connected by over 200 cross-border pipelines creating a huge and already available long distance transport system. Indeed, Europe's high-pressure gas transmission network, managed by the European Network of Transmission System Operators for Gas (ENTSOG), stretches over approximately 500,000 km across the EU and neighbouring countries (ENTSOG 2015).

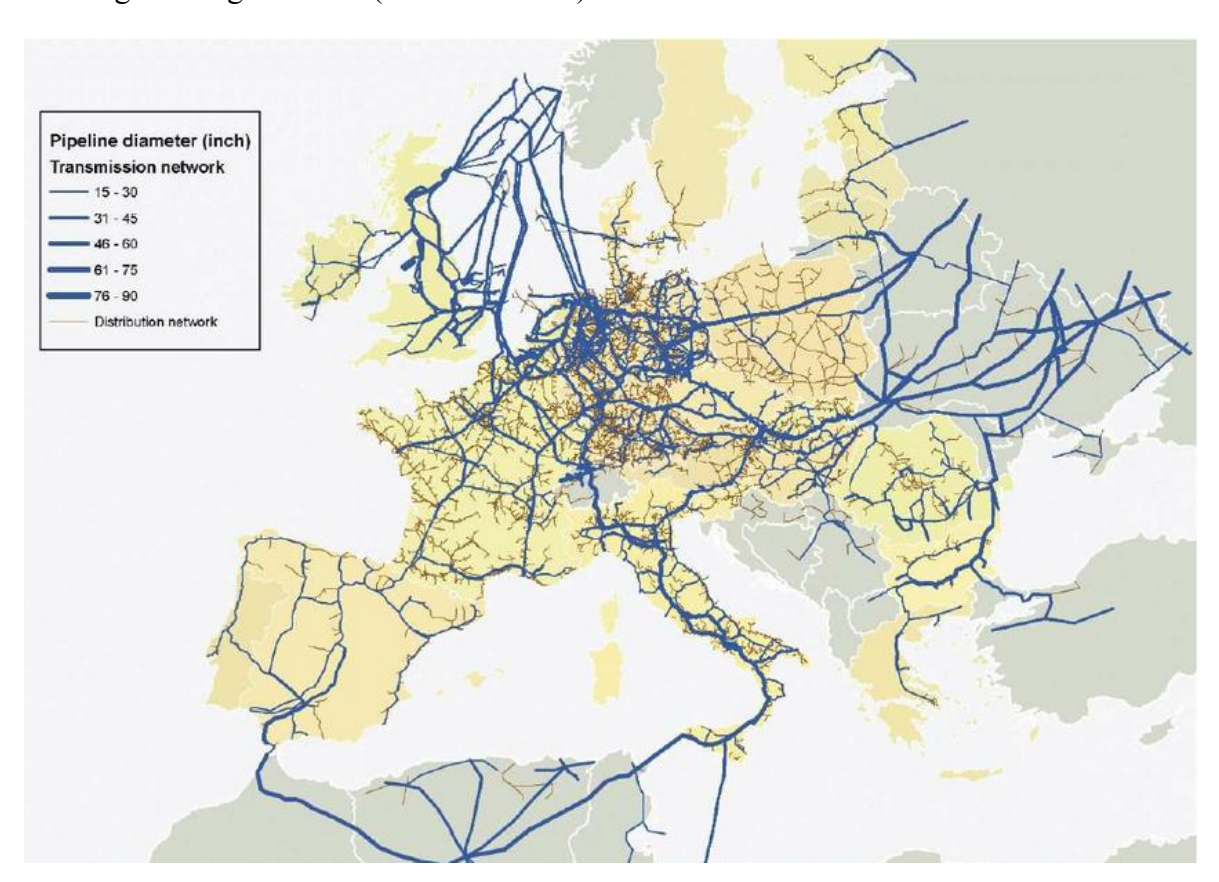


Figure 6. Map of the European NG network (Carvalho et al. 2009).

1.2 Factors to consider with HBNG

When investigating the blending of H₂ in NG networks, most of the researches agree that the operating network is suitable for small-scale H₂ uptake, but there are several critical issues in

the topic due to the properties of H₂ (Galyas et al. 2023). For example, the small size of the H₂ molecule, along with its lower volumetric density and viscosity, can pose safety risks for pipelines originally designed to transport NG. In addition, the presence of H₂ significantly changes the transferable energy capacity of the NG network.

To maintain energy balance and depending on H₂ concentration, the blended gas mixture may need to be transported at higher flow rates than NG. This may result in higher operating pressures and potentially exceed the design limits of compressors and pipelines, which were originally designed for NG transmission and distribution. Therefore, it is important to consider design changes to ensure the safe transportation of HBNG through existing pipeline systems and identify any potential risks and operational issues related to H₂ concentration.

1.2.1 H₂ vs. CH₄

NG typically consists of more than 95% CH₄ by volume, with other gases comprising smaller fractions, as shown in Table 5. Therefore, for the further sections and calculations, it was assumed acceptable to simplify NG with CH₄.

Table 5. Typical NG composition.

Constituent	СН4	C ₂ H ₆	N	CO ₂	СзН8	n-C ₄ H ₁₀	C ₄ H ₁₀	Others
Concentration (% vol.)	95.3	2.16	1.86	0.44	0.19	0.02	0.02	0.01

H₂ and CH₄ have different physical properties (Table 6). H₂ has a molecular weight that is 8 times lower than CH₄, which results in significantly lower values for most physical properties except viscosity. The viscosity of H₂ is approximately 30% lower than that of CH₄ at room temperature (25 °C).

Table 6. Comparison between H_2 and CH_4 in terms of physical properties at T = 0 °C and P = 1.0125 bar (Korb, Kawauchi, and Wachtmeister 2016; Goldmeer and Catillaz 2021; Kurz, Lubomirsky, and Bainier 2020).

Properties	H_2	CH ₄	Units
Molecular Weight	2.016	16.043	kg/kmol
Density (Gas)	0.08	0.65	kg/m³

Density (Liquid)	71	430–470	kg/m³
Specific Gravity	0.0696	0.555	_
Viscosity (at 25 °C)	0.89	1.11	10⁻⁵ Pa·s
Diffusion Coefficient in Air	0.61	0.16	cm²/s
Solubility in Water	0.0016	0.025	kg/m³

In terms of combustion and energy properties (see Table 7), H₂ contains 2.4 times more energy per unit mass than CH₄. However, the lower heating value (LHV) of H₂ per unit volume is three times lower than that of CH₄ due to its low density at standard conditions. This means that the energy content of the blended gas may be reduced with higher concentrations of H₂.

From the safety perspective, higher concentrations of H_2 tend to increase the risk of fire and explosion. Compared to CH_4 , pure H_2 has a much broader flammability range (5.3 times) and detonation-limit range (7.1 times). It also has a significantly lower ignition energy (14.5 times lower), which makes it more prone to ignition and increases the risk of fire. The low density of H_2 also leads to higher diffusivity in mixtures, which can result in more severe flammable and detonable events in confined spaces.

Table 7. Comparison between H₂ and CH₄ in terms of combustion and energy properties (Kurz et al. 2020).

Properties	H_2	CH ₄	Units
Energy Density	120	50	MJ/kg
Lower Heating Value (LHV)	10.2	34	MJ/m³
Higher Heating Value (HHV)	12.5	37.8	MJ/m³
Flammability Limits (in air)	4–75	5–15	% vol.
Detonation Limits (in air)	18.3–59	6.3–14	% vol.
Minimum Spark Ignition Energy	0.02	0.29	MJ
Autoignition Temperature	858	810	K
Laminar Flame Velocity	2.1	0.4	m/s
Specific Heat Capacity	14.86	2.22	J/(g·K)

Specific Heat Ratio	1.383	1.308	-
Wobbe Index	38.71	45.26	MJ/m³
Adiabatic Flame Temperature	2477.60	2235.93	K

The Wobbe index (W), represents the exchange capacity of different fuel gases and it is used to determine how changes in gas quality affect pipeline capacity. A high Wobbe index value suggests overheating or the presence of a significant amount of carbon monoxide, while a low value suggests a risk of flame instability or backfire. When 10% concentration of H₂ is mixed with NG results in a Wobbe index decrease of approximately 2% from baseline of pure NG (Soltyk 2007).

1.2.2 Characteristic gas flow and compressibility factor

In the work Galyas et al. (2023), the characteristic gas flow of a mixture between NG and H₂ was studied to predict the change in transferable energy content. The characteristic gas flow formula describes the pressure conditions of gas flow in pipelines and is based on the frictional Bernoulli energy equation and additional ones for the pressure dependence of the gas density and the flowrate (Tong, Qin, and Dong 2023). The Equations (1) and (2) are written for the pure CH₄ and for the CH₄-H₂ mixture:

$$p_1^2 - p_2^2 = \left(\frac{p_s}{T_s}\right)^2 \cdot \frac{1}{\left(\frac{\pi}{4}\right)^2 \cdot R} \cdot \overline{\lambda_{CH_4}} \cdot M_{CH_4} \cdot \overline{T_{CH_4}} \cdot \overline{Z_{CH_4}} \cdot \frac{L}{d_i^5} q_{CH_4}^2$$
(1)

$$p_1^2 - p_2^2 = \left(\frac{p_s}{T_s}\right)^2 \cdot \frac{1}{\left(\frac{\pi}{4}\right)^2 \cdot R} \cdot \overline{\lambda_{mix}} \cdot M_{mix} \cdot \overline{T_{mix}} \cdot \overline{Z_{mix}} \cdot \frac{L}{d_i^5} q_{mix}^2$$
(2)

where p_1 and p_2 are relatively the pressure at the starting and ending points, p_s and T_s the standard pressure and temperature, R the universal constant, $\overline{\lambda_{CH_4}}$ and $\overline{\lambda_{mix}}$ the average friction factors, M_{CH4} and M_{mix} the molecular weights, $\overline{z_{CH_4}}$ and $\overline{z_{mix}}$ the average compressibility factors, d_i the diameter and q the standards flowrate.

In the investigated scenarios the pressure conditions were kept identical in the studied horizontal pipe segment with constant diameter and without side draw, so the starting point and endpoint pressures are kept constant. Therefore, the left-and sides of Equations (1) and (2) are identical, and consequently the right-hand sides must also be the same.

The value of friction factors ($\overline{\lambda_{CH_4}}$ and $\overline{\lambda_{mux}}$) in the gas transmission system mainly depend on the relative roughness of the inner pipe wall due to the large Reynolds numbers, but the gas composition has negligible impact on the friction factor; therefore, the average friction factors are set to be identical.

The effect of gas composition on the temperature distribution is practically insignificant (remains below 1.5%) and could be neglected (Kuczyński et al. 2019). Considering these simplifications proposed, from Equations (1) and (2), the ratio of flowrates can be expressed:

$$\frac{q_{mix}}{q_{CH_4}} = \sqrt{\frac{M_{CH_4}}{M_{mix}}} \cdot \sqrt{\frac{\overline{z_{CH_4}}}{\overline{z_{mix}}}}$$
 (3)

The relative flow capacity of CH₄ -H₂ system depends on its specific gravity and compressibility factor.

Thus, the compressibility factor plays significant role in the transmission of H₂-NG mixtures, since its behaviour is opposite for H₂ and for NG with increasing pressure. Therefore, the change of the compressibility was determined as a result of numerous runs in Aspen HYSYS® simulation software; it has been established that the best fit can be achieved by using the Soave-Redlich-Kwong (SRK).

Figure 7 shows the relative flowing capacity of the pipeline as a function of H₂ content of the gas mixture. In particular, the compressibility factor seems differing slightly from 1, having a minimum of 0.968 when pure H₂ is transported.

Instead, the increase in flowrate appears to be more significantly dependent on the square root of the ratio of specific gravities, due to the nearly eightfold difference in molecular weights. For gas mixtures with 10 mol% and 20 mol% H₂ content the standard gas flow rate increase is approximately 4% and 9%, respectively. In case of transporting pure H₂ by pipeline the standard gas volumetric flow rate is increased by 165% compared to pure CH₄ when the pressure conditions of the investigated gas transmission pipeline are kept constant.

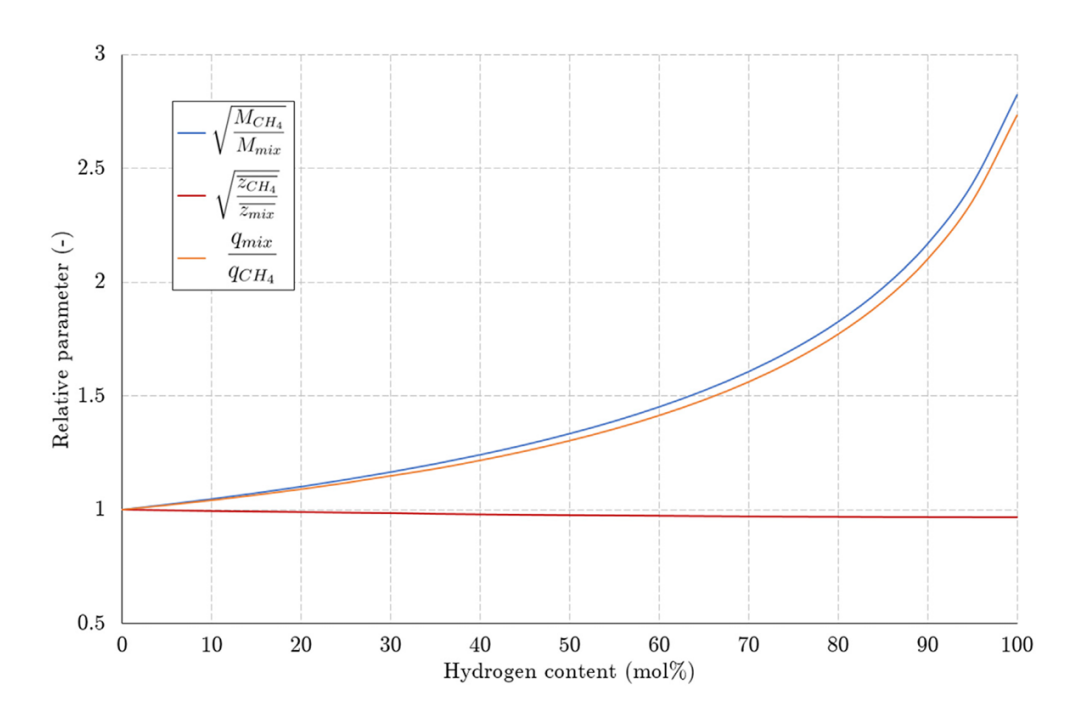


Figure 7. Effect of H₂ admixture on the flow rate (Galyas et al. 2023).

Also, the compressibility factor trends were investigated, highlighting differences between CH₄ and H₂. While the compressibility factor of CH₄ decreases as the pressure increases, the H₂'s compressibility factor increases. Another significant difference is that the compressibility factor of H₂ is practically independent of the temperature between 0 and 50 °C.

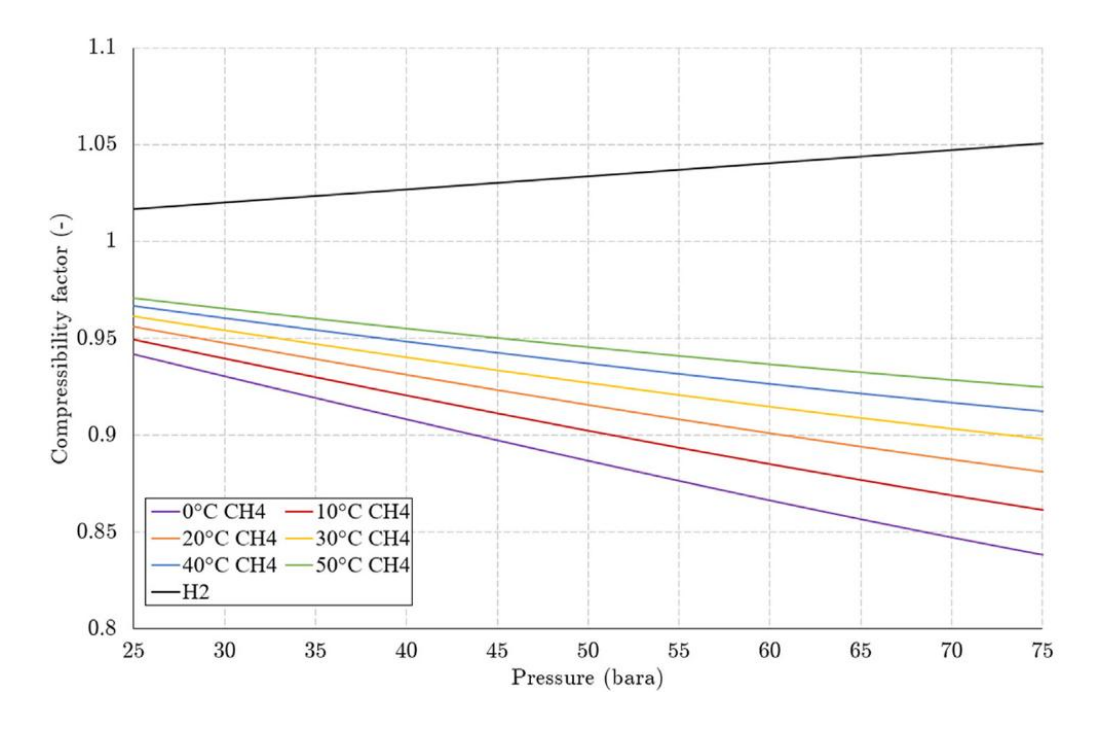


Figure 8. The compressibility factor curves of CH₄ and H₂ (Galyas et al. 2023).

Getting deeper, Figure 9 shows the compressibility factor curves of 20 mol% H₂ in CH₄ -H₂ gas mixture. These curves have and overall decreasing tendency with increasing pressures, which is more significant at lower temperatures.

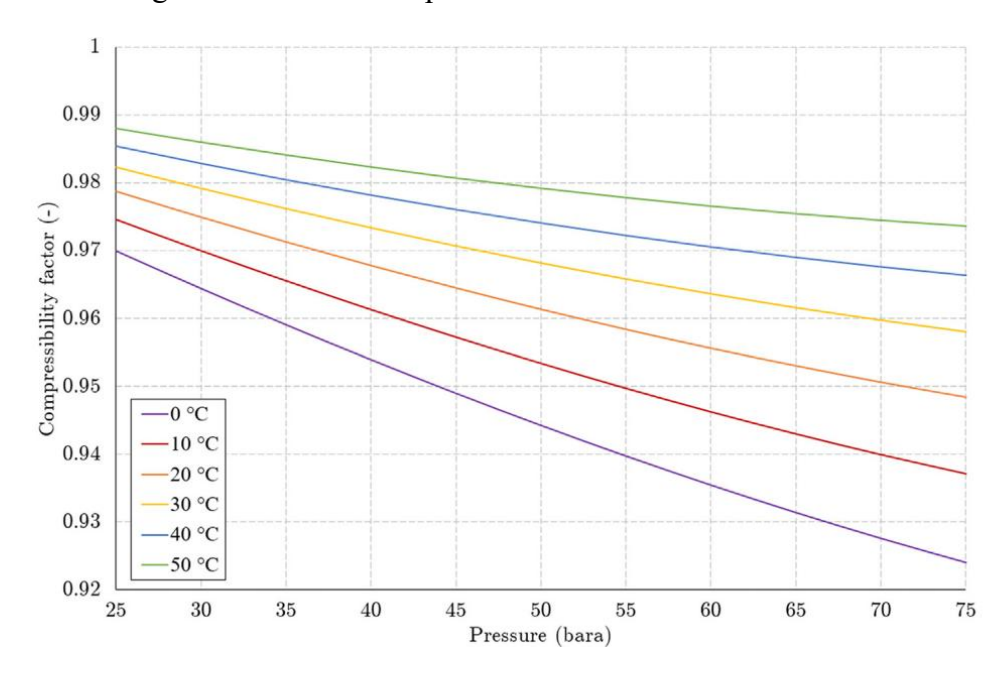


Figure 9. Compressibility factor curves for 20 mol% H₂ concentration case (Galyas et al. 2023).

1.2.3 Energy transmission

Energy transmission is a key factor to consider when converting an NG pipeline to a HBNG one. The amount of transmitted energy can be calculated by multiplying the standardized operating flow rate by the LHV of the gas mixture. As explained in section 1.2.1, H₂ contains 2.4 times more energy per unit mass than CH₄, but the LHV of H₂ per unit volume is 3 times lower than the one from CH₄ due to its low density at standard conditions. Therefore, when using pure H₂ the energy transmission is approximately 3.3 times lower than when using pure CH₄. In other words, the lower the concentration of H₂ in the gas mixture, the higher the energy transmission for the same flow rate and pressure.

The energy throughput capacity is illustrated in Figure 10 for simulated transmission (a) and distribution (b) pipelines (Cristello et al. 2023). For example, the transmission pipeline with NG would typically transmit 4.80×10⁸ MJ/day, but this would drop to 1.44×10⁸ MJ/day with pure H₂ in the pipeline. Thus, if it is desired to maintain the same energy transmission in a

pipeline conversion, the flow rate and/or operating pressure must be increased accordingly. These changes may not be trivial; increasing the operating pressure may be constrained by the pipe material used, or it may be limited by the number of compressors that can be installed (Cristello et al. 2023).

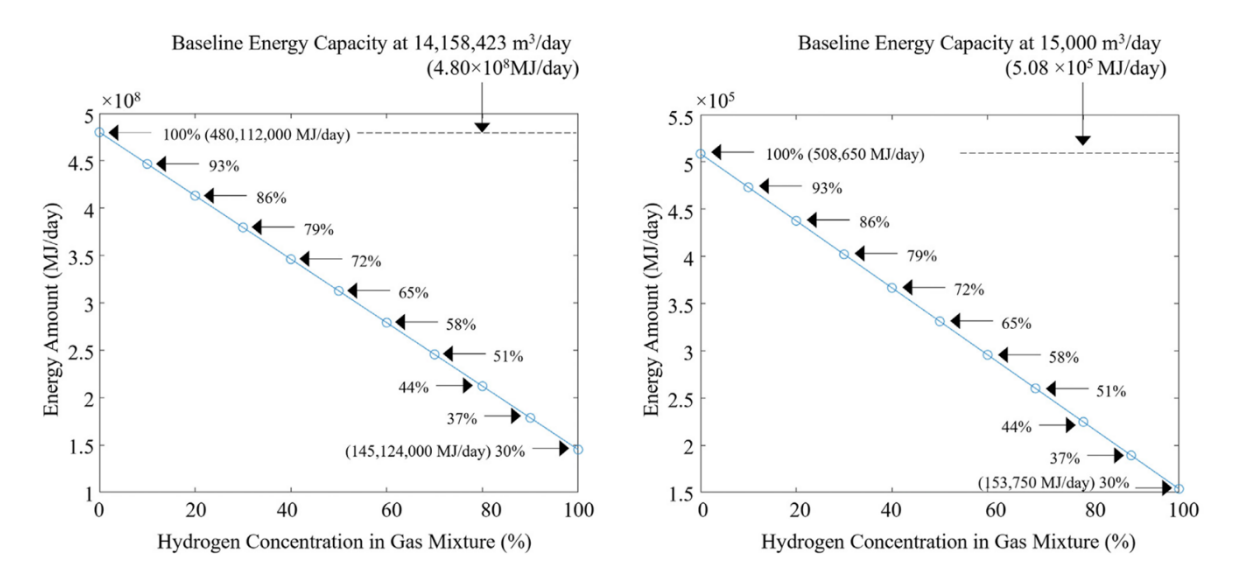


Figure 10. Energy transmission by H₂ concentration in the gas mixture (Cristello et al. 2023).

1.2.4 Temperature during pressure drops

Fluid transport through pipelines can result in temperature variations due to two main sources. The first is the heat transfer between the inside of the pipeline and its surroundings. The second is the Joule-Thompson effect, which is a change in temperature that occurs when gas expands due to pressure differences between the inlet and outlet. This effect is described by Equation (4):

$$J_t = \left(\frac{\partial T}{\partial P}\right)_H \tag{4}$$

Where: J_t is the Joule-Thompson coefficient (°C/bar), T is the temperature (°C), and P is pressure (bar). H denotes that the partial derivative is evaluated at constant enthalpy.

The Joule Thompson coefficient (J_t) is a property of the gas being used as well as the temperature and pressure of the gas prior to expansion. Every gas has an inversion point at which the Joule-Thompson coefficient changes sign and the gas begins to either warm or cool.

Most gases, including CH₄, have a high inversion point temperature, meaning that a pressure drop has a cooling effect. H₂, however, is one of the few gases that has a very low inversion point, with an inversion point of -71 °C at atmospheric pressure. As a result, H₂ generally experiences a warming effect when subjected to a pressure drop. Constant values for CH₄ (0.5 °C/bar) and H₂ (0.035 °C/bar), obtained from the literature (Haeseldonckx and Dhaeseleer 2007), are normally assumed. The highest temperature change occurs at higher concentrations of H₂ and transmitted energy.

1.2.5 Hydrogen embrittlement

One major concern when using H₂ in pipelines is its ability to permeate through materials. H₂ can easily diffuse into the lattice structure of materials, causing them to become weaker and more prone to cracking under stress. This process, known as H₂ Embrittlement (HE), can be a significant issue for pipelines and lead to unexpected failures. HE can reduce mechanical properties, such as tensile strength, ductility, fracture resistance, and fatigue resistance, making pipelines more prone to loss of ductility and cracking.

Gaseous H₂ has a significant impact on fatigue and fracture resistance of line pipe steels, and questions remain regarding how to account for this when assessing steel pipeline compatibility with H₂.

A report from the US Department of Energy indicates that the majority of NG networks are made of carbon-steel materials (i.e., 99.7% of transmission and 50.4% of distribution lines) (Department of Transportation 2010). As such, when considering the use of existing NG networks for H₂ transportation, it is crucial to determine whether the existing metallic materials are compatible with H₂ gas service. Carbon steels, including ASTM A 106 Grade B, ASTM A 53 Grade B, and API 5L Grades X42 and X52, have been shown to be suitable for use in H₂ pipelines with pressures up to 140 bar, according to ASME B31.12 (Schmura, Klingenberg, and Corporation 2005).

The Hydrogen-Environment Embrittlement (HEE) Index is a metric used to evaluate the potential for hydrogen embrittlement in a material. It compares the Notched Tensile Strength (NTS) of a specimen when tested in a H₂ environment to the NTS when tested in air or helium.

The NTS of a material is the value given by performing a standard tensile strength test on a notched specimen of the material.

The HEE Index can be calculated using the equation:

$$HEE Index = NTS Ratio = NTS in hydrogen/NTS in air or helium$$
 (5)

The HEE Index is a ratio ranging from 0 to 1, with higher values indicating a lower susceptibility to hydrogen embrittlement (Table 8). Materials with an HEE Index close to 1 are therefore preferred.

Table 8. Hydrogen embrillement	(HE) severily and HEE I	ndex ranges (Cristello et al. 2023).

HE Severity	HEE Index (NTS Ratio)
Negligible	1.00 - 0.97
Small	0.96 - 0.90
High	0.89 - 0.70
Severe	0.69 - 0.50
Extreme	0.49 - 0.0

Table 9 summarizes HE severity, HEE Index and the compatibility of common industrial materials with H₂. It also specifies the H₂ pressure at which the HEE Index was measured, either 69 bar or 689 bar. Notably, ferritic steels commonly used in current gas pipelines exhibit HEE severity ranging from high to low when exposed to pressures up to 69 bar at room temperature. More ductile materials, such as stainless steels (304 and 316) and copper-based alloys, show relatively low HEE severity even at high pressures (689 bar) and demonstrate good resistance to hydrogen embrittlement in both gaseous and liquid states.

Table 9. Hydrogen embrittlement (HE) severity and HEE Index for commercialized materials (Cristello et al. 2023).

Material		Lab	-scale HE Ev	valuation	Material compatibility H ₂			
17146	1 1411	H ₂ pressure (bar)	HE Severity	HEE Index (NTS Ratio**)	Gas	Liquid		
Ferritic Steels	A106- Gr. B	69	High	-	Acceptable	Not acceptable		
(carbon	A516	69	High	0.83	Acceptable	Not acceptable		

steels and low alloy	alloy X42 69		High	-	Acceptable	Not acceptable
steels)	API 5L X52	69	High	0.86	Acceptable	Not acceptable
	API 5L X60	69	Small	0.92	Acceptable	Not acceptable
	API 5L X65 69		Small	0.94	Acceptable	Not acceptable
	API 5L X70	69	Small	0.90	Acceptable	Not acceptable
Austenitic	304L	689	Small	0.87	Acceptable	Acceptable
Steels	316	689	Negligible	1	Acceptable	Acceptable
Copper	Copper (OFHC*)	689	Negligible	1	Acceptable	Acceptable
Based	70-30 Brass	689	Negligible	-	Acceptable	Acceptable

OFHC*: Oxygen free-high thermal conductivity.

NTS Ratio**: calculated in H₂ and helium environments.

The HEE index can also be correlated with the operating pressure through a proportionality constant and a material-dependent exponent, as described in Equation (6). This relationship reinforces that higher pressures increase the risk of H₂ embrittlement.

$$HEE Index = \alpha(P)^{-n} \tag{6}$$

Where: α is a proportionality constant, P is the H₂ pressure (bar), n is the material-dependent decay exponent.

Temperature is another factor that strongly influences H₂ embrittlement behaviour. In general, hydrogen embrittlement occurs at temperatures below 95 °C. At high temperatures (> 200 °C), H₂ embrittlement is usually not a problem for most materials. However, High Temperature Hydrogen Attack (HTHA), also known as hydrogen attack, can be a concern. This occurs when H₂ dissociates into its atomic form and diffuses into steel, reacting with carbon to form CH₄. This can cause various problems, including fissures and cracks in the pipeline. While each material's resistance to HTHA varies and depends on both temperature and pressure, API 941 provides a comprehensive list of recommended practices and operational limits for different steels (Inspectioneering 2022).

1.3 Jet fires

Jet fires are turbulent diffusion flames following the ignition and combustion of a flammable fluid coming out continuously from a pipe or orifice, which burns close to its release point. Between the release point and the flame there can be a zone, called lift off zone, where there is no combustion because there is a high quantity of fuel, and the velocity is very high (Casal 2018a).

Due to the high degree of turbulence, the combustion efficiency is usually higher in jet fires than in other flame events, such as pool fires, and therefore they are more dangerous due to the heat they can transfer and the potential direct impact of the jet on other equipment. Thus, in the evaluation of the hazard posed by jet flames, the accurate determination of the likelihood of flame impingement and/or the amount of radiant energy received by objects at a distance from the flame is of primary importance.

If a jet fire accident occurs in a plant in which the density of equipment is high, as happens in a process plant or in an oil platform, its flames impingement and thermal flux on an equipment and thermal flux can originate another release, fire or explosion, with the consequent escalation of the effects and consequences of the whole accident. This is called "domino effect". The domino effect has been defined by Delvosalle (1996) as "a cascade of events in which the consequences of a previous accident are increased both spatially and temporally by the following ones, thus leading to a major accident".

A good example is the serious accident that occurred in a petrochemical plant in Priolo, Italy, in 1985 (Casal 2018b). The failure of an instrument caused the increase of pressure in the reboiler of a distillation column and a safety relief valve was activated; the flammable gas released was ignited, forming a jet fire. This jet fire impinged on a pipe with a diameter of 600 mm containing ethylene at 18 bar that, after a relatively short time failed, originating a very large jet fire. This impinged on a set of cylindrical storage tanks located at a distance of 60 m; one of them underwent an explosion (BLEVE) followed by a fireball; the ejected fragments damaged other equipment, originating other fires. The plant had been evacuated, so there were no fatalities (one operator wounded), the plant was seriously damaged: a serious accident, started by a relatively small jet fire.

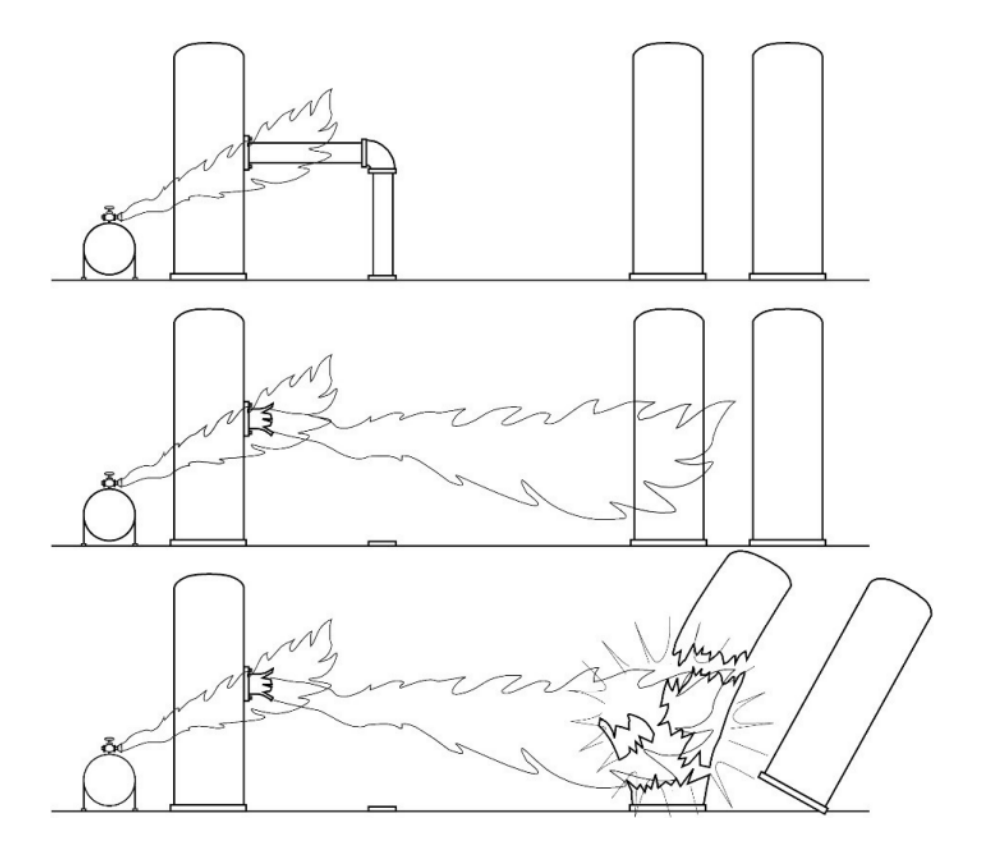


Figure 11. An example of a domino effect originated from a jet fire (Casal 2018b).

Table 10 provides information on several domino accidents in NG transmission pipeline systems involving jet fire impingement, that occurred between 1971 to 2020. These incidents serve as stark reminders that regardless of the initial trigger for an accident, be it corrosion, excavation activities, or an explosion, the moment a jet of flammable fluid is released and subsequently ignites while impinging on a pipeline, there is a substantial possibility of a chain reaction occurring. This domino effect can lead to a series of interconnected accidents, intensifying the overall impact and magnitude of the incident.

Table 10. Several cases of jet fire domino effect in parallel pipelines (Foroughi, Casal, and Pastor 2023).

Location, year	Cause	Accident	Brief description	Reference
Gulf of Mexico, USA 1989	External	Explosion → Fire → Rupture	18 in sales gas pipeline on the platform failed during installing a pig trap on it. Released hydrocarbons ignited. The explosion and fire burned the main structure and caused subsequent explosions when six other pipelines ruptured due to the intense heat	(USDI 1989)
Rapid City Canada, 1995	Stress corrosion cracking	Fire → Fire → Failure	Corrosion ruptured a gas pipeline. The jet fire affected another gas pipeline: rupture; fire on a third 48 in gas pipe which did not fail.	(TSBC 1995)
Al Khobar Saudi Arabia, 1996	Terrorist attack	Fire ≯ Explosion ≯ Fire	A terrorist attack targeted the U.S. military housing complex known as Khobar Towers. The attack involved a truck bomb that caused a massive explosion. The ensuing jet fire impinged on nearby pipelines, triggering a domino effect of fires and explosions. The incident resulted in significant casualties and	(MHIDAS 2007)
Uch Sharif Pakistan, 2004	External event	Explosion → Fire → Explosion	A pipeline explosion occurred due to a leak, resulting in a jet fire that impinged adjacent pipelines. The subsequent domino effect caused a chain reaction of explosions. The incident resulted in casualties, widespread damage,	(MHIDAS 2007)
San Bruno USA, 2010	External	Fire → Explosion → Fire	A natural gas pipeline ruptured due to high-pressure gas flow. The rupture led to a jet fire impingement on nearby pipelines, causing a chain reaction of explosions. The incident resulted in multiple fatalities, and extensive property damage.	(NTSB 2011)
Alabama USA, 2011	External	Explosion → Fire → Failure	A gas pipeline exploded, and the jet fire burned for hours and damaged a closed pipeline.	(USDT 2011)
Manitoba Canada, 2014	Welding failure	Explosion → Failure → Fire	Natural gas released from the pipeline ignited, and the resulting fire burned for approx. 12 h. Two adjacent pipelines were shut down before rupture.	(TSBC 2014)

1.3.1 HBNG jet fires

Pipeline transportation of HBNG is susceptible to leakage or rupture accidents caused by pipeline construction, corrosion and, as discussed previously, H₂ embrittlement, posing significant threats to the environment, human safety and property.

From a safety perspective, increasing H₂ content in NG grid markedly raises the likelihood and severity of fire and explosion. As discussed in section 1.2.1, pure hydrogen's flammability range is over five times wider than CH₄'s, and its ignition energy is nearly an order of magnitude lower, making H₂ far easier to ignite. Its low molecular weight also accelerates mixing with air, increasing the risk of deflagration or detonation in confined spaces. HBNG leaks release energy more abruptly, producing sharp pressure drops and shorter leak durations (El-Ghafour, El-dein, and Aref 2010). In practical terms, whereas pure CH₄ ignites between 5 % and 15 % vol., H₂ will ignite anywhere from 4.0 % to 74.2 % vol., so even modest blends substantially expand the danger zones around a leak and make jet fires more probable (B.J. Lowesmith and Hankinson 2013).

The increase in H₂ content leads to shorter flame lengths. This can be attributed to the momentum diameter, the initial jet diameter scaled by the square root of the fuel-to-air density ratio, which is smaller at higher H₂ content. This variation is due to the lightness of the hydrogen-enriched mixture. At the same time, the high molecular diffusivity of H₂ increases the air entrainment coefficient, for which the flame length is inversely proportional (A. Choudhuri 2000).

The relatively slower reaction rate of a typical hydrocarbon fuel can be accelerated by admixing H₂ enhancing the production of radicals/atoms such as H, O and OH. It also results in an improved ignitability and flame holding and shrinks the global convective time scale (A. Choudhuri 2000). For this phenomena spends less time in the visible flame zone and, therefore, travels a shorter distance before completing combustion (Choudhuri and Gollahalli 2003). Kong et al. confirmed this trend experimentally, reporting that under constant pressure a 10 % vol. H₂ blend produced a 1.28 m flame, while a 50 % vol. H₂ blend measured just 1.13 m (13.7 % shorter). Differences in radical concentrations were obtained, which influenced flame chemistry (Kong et al. 2024).

Hydrogen enrichment also reduces the lift off distance of the flame, in opposition to an increase of the internal pressure. This is related to the competition between the local flow velocity and the combustion velocity at the bottom of the diffusion flame. When the operating pressure rises, the local flow velocity at the nozzle also increases. The flame moves away from the nozzle and the lift off distance gradually increases. Blending H₂ into CH₄ also contributes to an increase in the local flow velocity of the jet gas. It is noticeable that H₂ burns at a significantly faster rate compared to CH₄. Additionally, the higher molecular diffusivity of H₂ increases air entrainment and further promotes fuel combustion. As the concentration of H₂ in the mixture increases, the increase of the combustion speed of the flame is higher than that of the local flow velocity of the jet gas. Then the flame reaches a new balance nearer the nozzle, and the lift off distance is correspondingly reduced (Kong et al. 2024).

The convective time scale, which is a representation of the global flame residence time, decreases as H₂ concentration increases in the mixture too. Faster chemistry and stronger entrainment combine to shorten flame lifetime, reinforcing the decrease in both length and lift off distance.

Regarding the emissions (Figure 12), the higher flame temperatures and radical pools enhance NO production through *Zeldovich mechanism*, while lower CH concentrations at higher blending rates reduce NO destruction through *Fenimore mechanism* (A. Choudhuri 2000). As combined effect the NO and NO_x emissions increases. Meanwhile, CO emissions fall: for a given Reynolds number, less carbon enters the flame, and the boost in OH radicals accelerates CO oxidation, driving the CO emission index downward (EI) (El-Ghafour, El-dein, and Aref 2010).

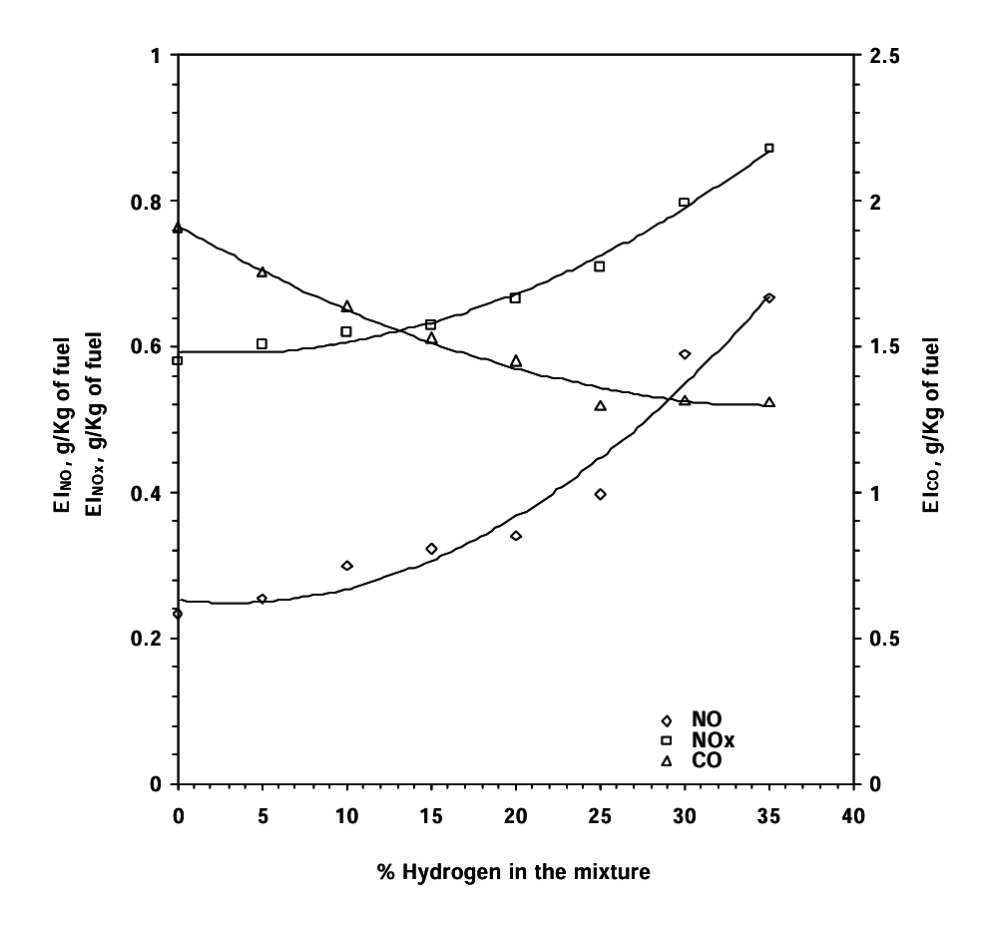


Figure 12. Variation of NO, NOx, and CO EI with % H₂ in the mixture (Choudhuri and Gollahalli 2002).

An example of a horizontal HBNG jet fire is shown in Figure 13. In horizontal jets, the interplay of momentum and buoyancy produces a characteristic curvature. Near the nozzle, the transparent, soot-free base burns with a blue hue, rich in CH and C₂ radicals; higher up, soot-laden yellow regions appear. As H₂ is added, the blue, soot-free zone expands upward, pushing the yellow, luminous tip further along the trajectory.

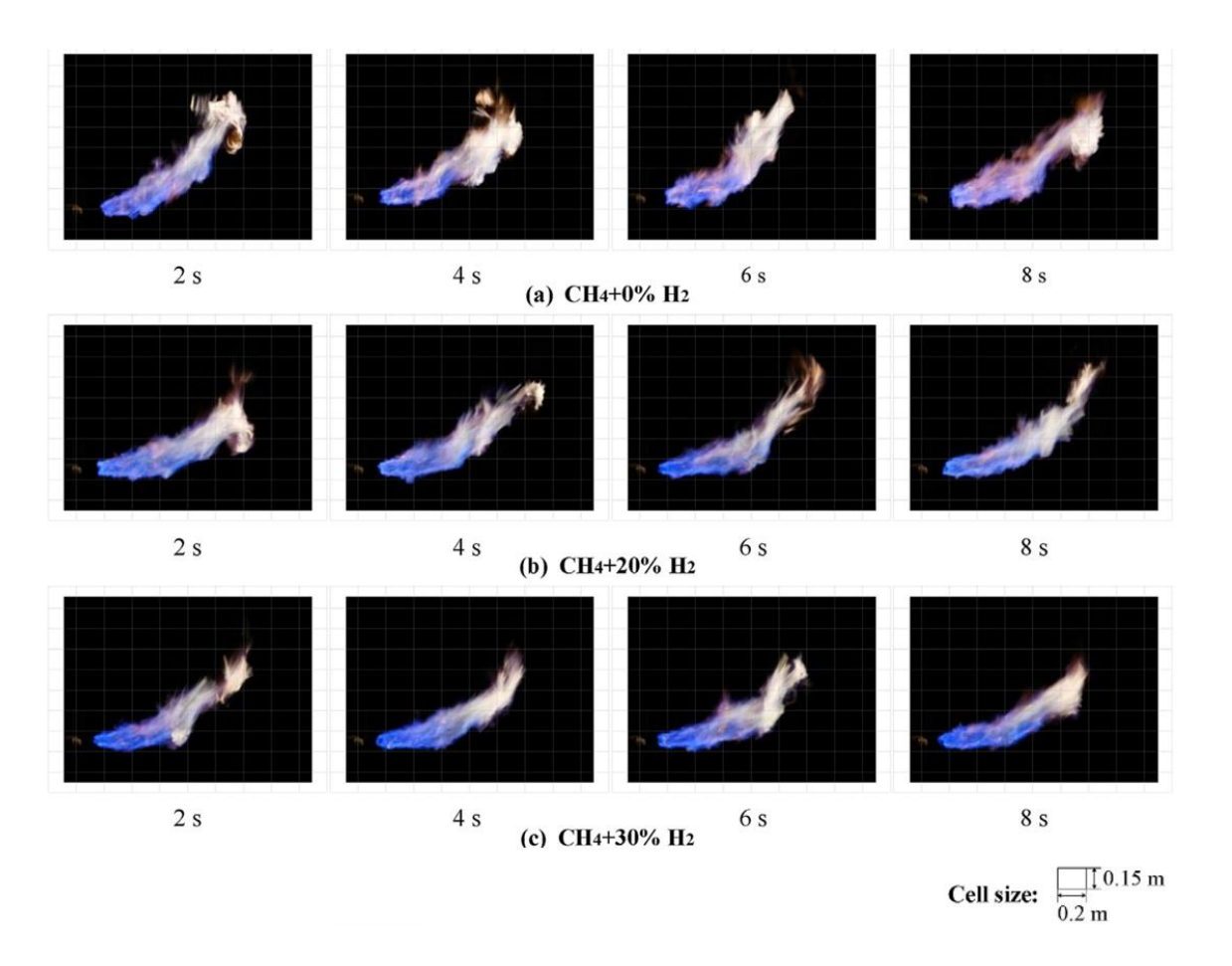


Figure 13. Flame images of mixture of CH₄ and H₂ with H₂ volume fraction from 0% to 30% at P = 400 Pa and. Background grid with a cell size of 0.2 m x 0.15 m (Kong et al. 2024).

1.3.2 Jet fires simulation

Models developed for estimating the received radiated heat flux by objects at a distance from jet flames can be broadly divided into three categories: semi-empirical, field, and integral models. Of these three types, semi-empirical models are, in comparison with integral or field models, mathematically simpler, easier to understand and formulate, quicker to implement in computer programs, require significantly shorter computational run times, and predict flame properties that are of interest for hazard assessment studies with reasonable accuracy. However, semi-empirical models are heavily dependent on experimental data and are limited to the specific type of fire studied during experimentation and the range of conditions under which model correlations were derived.

Semi-empirical models are usually designed to predict quantities such as flame shape and heat fluxes to external objects without providing a detailed description of the fire itself. They can be further divided into:

- a) **Point source:** point source models do not attempt any shape prediction and represent the source of heat radiation by a point.
- b) **Multiple point source:** multiple point source models attempt to model the effect of flame shape on radiated heat flux by representing the flame with a flame centreline trajectory along which several radiating point sources are distributed.
- c) Surface emitter: Surface emitter models represent the flame by a solid object (usually a cone or a cylinder) from which heat is being radiated

Of all semi-empirical models for jet fire simulation that have been correlated over a wide range of conditions encompassing typical jet fires, the JFSH model implemented in Process Hazard Analysis Software Tool (PHAST), the proprietary consequence analysis tool developed by the Norwegian company DNV and used in the research. This model can estimate the basic features of a jet fire (DNV 2025) using two different model: the surface emitter model by Chamberlain, which was later extended by Johnson (Johnson, Brightwell, and Carsley 1994) and the Miller multipoint source emitter flame model (M-MPS) (Miller 2017).

The Chamberlain model was originally developed for modelling jet fires resulting from vertical/inclined vapour phase releases, and the extension, Johnson et al. (1994), specifically simulates jet flames resulting from horizontal/near horizontal vapour phase releases. The Chamberlain model, when compared with multiple point source models, gives a better physical description of flame behaviour by its representation of a flame with a solid body (conical frustrum), emitting radiation through its surface.

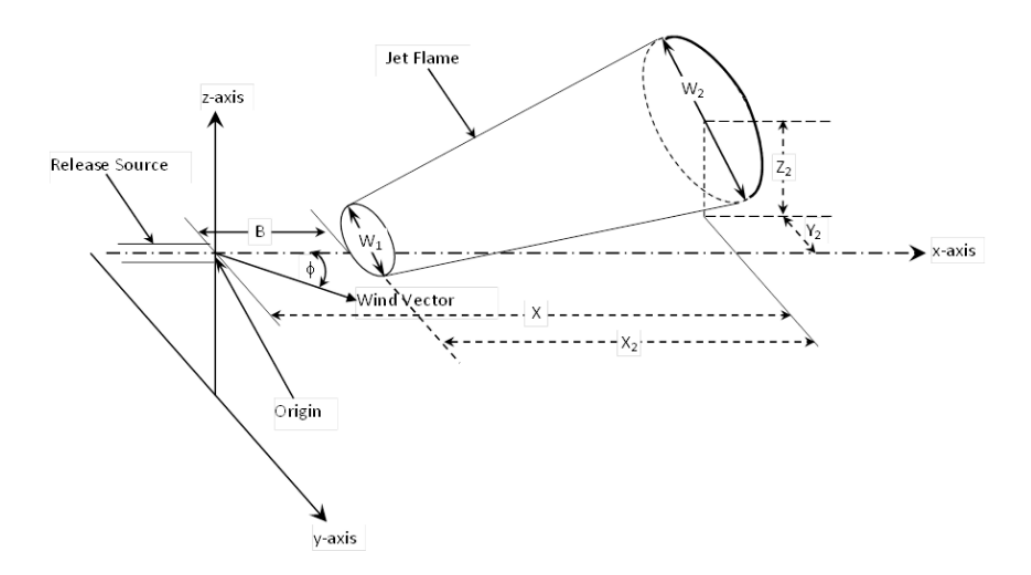


Figure 14 Jet fire for horizontal jet fire model ((Johnson, Brightwell, and Carsley 1994).

The Miller model was primarily developed for low to high pressure releases of non-hydrocarbon/low-luminosity gases, pointed downwind in the horizontal, vertical or 45° inclined release directions. The jet flame in this case is represented as shown in Figure 15 and it is modelled as a distribution of individual point sources along the flame centreline. The model predicts maximum surface emissive power and flame characteristics as in the Chamberlain model, except frustum base and tip width. Radiation emitted along the flame centreline is modelled in terms of a weighting factor representing the proportion of combustion energy multiplied by a fixed fraction of heat radiated at different positions along the flame length (DNV 2023).

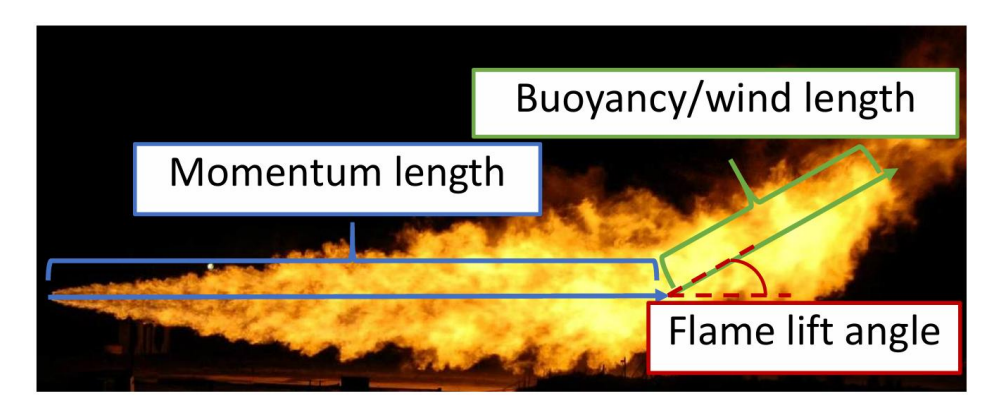


Figure 15. Miller model flame representation for horizontal jet fires (DNV 2023).

With respect to radiation this is emitted along the flame centreline with an intensity distribution that rises and falls in a linear fashion with a maximum at a distance corresponding to 2/3 of the overall flame length following Figure 16 scheme.

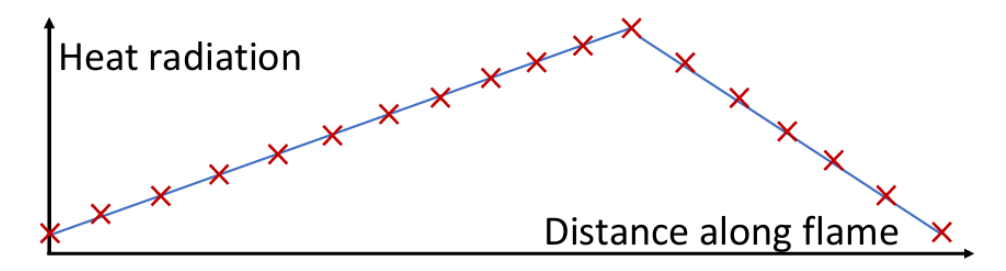


Figure 16. Miller model radiation intensity distribution (DNV 2023).

1.3.3 Safety distances according to vulnerability

The area potentially affected by an accident can be divided into different zones according to the type of hazard (chemical, mechanical or thermal), the intensity of the effects, and the vulnerability of people and property (Casal 2018a):

- a) Intervention Zone (IZ): accidents involve a degree of damage, which warrants the immediate application of protective measures.
- b) Alert Zone (AZ): accidents involve effects that, although perceptible by the population, do not justify intervention, except to protect critical groups of people.
- c) Domino Effect Zone (DZ): zones in which potential accident propagation must be considered.

Since the harm of thermal radiation in pipeline leakage accidents is considered to be dominant according to other authors (Froeling et al. 2021), the official threshold values applied in Spain for thermal type accidents are shown in Table 11.

Table 11. Threshold values (thermal radiation dose or intensity) for IZ, AZ, DZ (Casal 2008).

Dangorous	Accident	Description of	7	Threshold value	
Dangerous phenomenon	type	Description of planning zones	Intervention zone (IZ)	Alert zone (AZ)	Domino zone (DZ)

Thermal type	Zones surrounding the jet	250 (kW·m ⁻²) ^{4/3} 5 kW·m ⁻² for 30 s	115 (kW·m ⁻²) ^{4/3} 3 kW·m ⁻² for 30 s	8 kW·m ⁻²
--------------	---------------------------	---	---	----------------------

1.4 Neural Networks (NN)

Various methods can be used to study jet fires behaviour, such as performing experiments or CFD simulations. Experimental methods, carried out even on a small scale, generate high costs because they require the use of expensive control and measurement equipment. In order to maintain a sufficiently high level of safety, large scale jet fire investigations should be carried out on training grounds, which requires both a great deal of money and work (scientific, technical and organizational). Moreover, the measurement of large jet fires is burdened by problems with the accuracy of determining the length and width of the flame.

Methods based on CFD techniques do not present all these disadvantages. However, numerical methods also require a considerable amount of money, associated with the purchase of suitably powerful computing servers and CFD simulation software. Additionally, CFD methods use mathematical models that are based on simplifications related to the description of the combustion process in turbulent flow, for example, which affects the accuracy of their results. Also, the CFD simulation of large jet fires (where the flame length exceeds several meters) requires a suitably dense numerical grid. Calculations carried out on such grids can take from a few days to even a few weeks depending on the performance of the computing server used. Experimental methods are most often used to verify the results of CFD calculations or to create correlations, using dimensionless numbers, to determine the flame length of a jet fire. It is virtually impossible to use CFD methods in tools for determining flame sizes included in risk analysis programs.

In the last years, machine learning has been shown to be one promising tool to develop models. Among the different possibilities, neural networks (NN) are used to uncover connections between data, if any exist. NNs have the following characteristics: high speed connections, nonlinear calculations, communication of output and input datasets, flexibility, response to noisy data, high availability, and retraining.

The NN approach is inspired by the way the human brain and the nervous system are organized. An NN model is a computing model that is able to reproduce structural or functional characteristics of a given system. In the 1940s, research on the network approach started when data from different subjects were analysed and classified. However, NNs were not extensively used until the second half of the 1980s since it was impossible to overcome past theoretical barriers. For example, one of them was the representational content: it was not possible to construct machines with genuine representative action without understanding what representation is (Bickhard 1993). Today these theoretical barriers no longer exist and NNs are currently popular. The NN has the advantage of requiring less processing to solve challenging tasks (Michał Lewak and Jarosław Tępiński 2023). Over the last two decades, network classifiers have become one of the most popular strategies in the machine learning field.

In the NN approach, all the variables of the network's model are created, collected in matrixes and tuned starting from a dataset. The simplest processing unit that could process data is a neuron; its inputs and outputs are both numerical values. The network is made up of synapses, where the base units, indeed neurons, link each other from the input to the outputs one. A weight (w), which reflects its relative value, is given at each link. Multiple input variables (x_i) and output interconnections are possible for a single neuron. The output is then created by computing this weighted sum via an activation transfer function (f). The bias value (b) can then be added to the total of all these values once they have been put together. Then the results coming from Equation (7) are fed into a transfer function (f) to get the output signals (y) in Equation (8).

$$net_j = \left(\sum_{i=1}^N w_{ij} x_i\right) + b \tag{7}$$

$$y_j = f(net_j) \tag{8}$$

The transfer functions are usually ramp, linear, step or sigmoid. In order to create a layer of neurons, the neuron cells link with one another. The structure of the network is made up of one or more layers of neurons. One type of NN is the feedforward NN (Figure 17), with $X_1, X_2, ...$ and X_n serving as model inputs, n serving as the number of input nodes, w_{ij} serving as the neuron's weight factor of a neuron j, b serving as the bias value of a neuron j, and y_j serving as the output of a neuron.

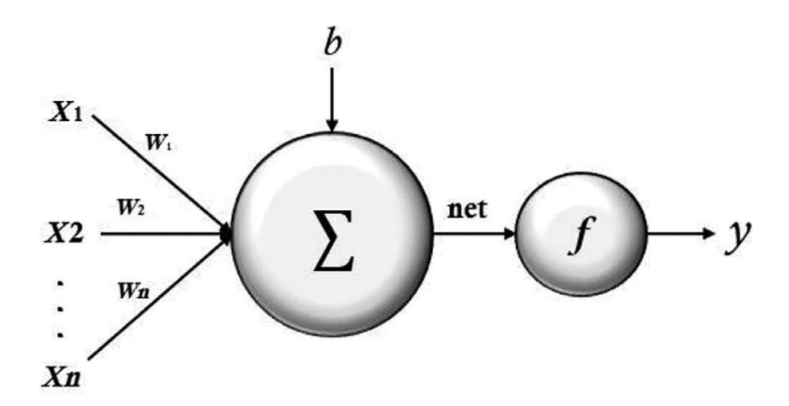


Figure 17. Feedforward NN (Mashhadimoslem et al. 2023).

1.4.1 Multilayer feedforward neural network (MLFFNN)

Algorithms to ascertain the connectivity in the weights of neurons are found via learning in NNs, starting from Equation (7) and (8).

An MLFFNN method typically comprises an input layer, one or more hidden layers, and an output layer that gathers, analyses, and transmits the data. In order to reduce the overall mean squared error, the network is trained and tuned. Equation (7) shows how the MLFFNN method for an NN output is developed:

$$y_j^k = f_k \left(\sum_{i=1}^{N^{k-1}} w_{ij}^k x_i^{(k-1)} + b_j^k \right)$$
 (9)

Where w is the weighted vector for a value i and neuron j at layer k (the values are not elevated for it), multiplied by the value at the precedent layer k-1, summed with the relative bias b_j^k , creating the neuron for k. Then, the nonlinear activation transfer function is applied, called f_k . The result will correspond to the output parameters y_j^k . Based on the previous explanations, the basic organization of a MLFFNN can be represented as shown in Figure 18.

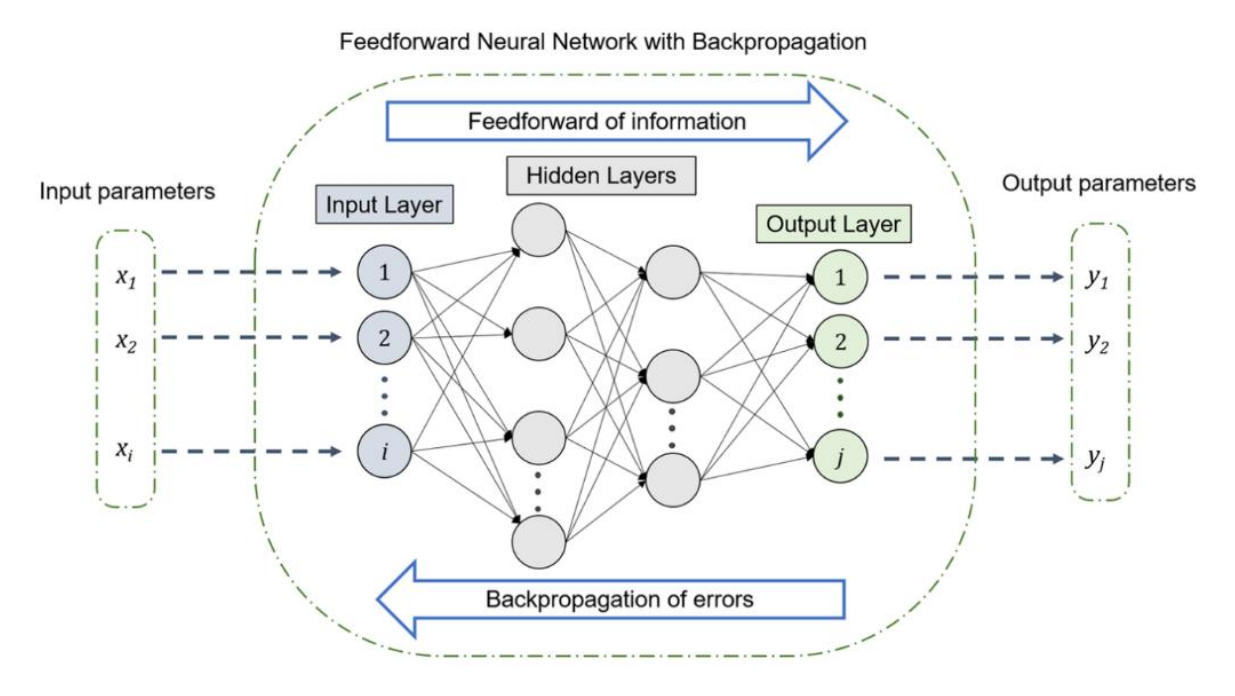


Figure 18. A multilayer feedforward neural network (MLFFNN) approach with backpropagation for NN structure (Sun et al. 2020).

1.4.2 Activation transfer functions

There are numerous alternative ways to think about the activation transfer function, which include identical function, binary sigmoid, hyperbolic tangent etc.

The Sigmoid function is a specific case of logistic function and is bound between 0 and 1. There are two disadvantages of the Sigmoid function. First, the gradient of the Sigmoid function is almost 0 when the Sigmoid function goes to 0 or 1. Second, the Sigmoid function is not symmetric by origin, which will cause issues when updating the weight during backpropagation (BP).

Meanwhile, the *tanh* function solves the second issue because it is origin-symmetric and is bound between -1 and 1. However, the issue of the gradient approaching 0 at the extremes has not been solved. A linear function can solve this gradient issue; however, the combination of the linear function has bad performance for a highly nonlinear problem (Zhong et al. 2024).

During the training process of the BP NN model, a common problem encountered is the vanishing and exploding gradients. The vanishing gradient issue can lead to a slowdown or

almost negligible weight updates, while the exploding gradient occurs when the gradient values between network layers exceed 1.0, resulting in an exponential growth of the gradients. This makes the gradients extremely large, causing significant updates to the network weights and thereby making the network unstable. To address these issues s in the training process mentioned above, the *ReLU* (Rectified Linear Unit) function is usually set as the activation transfer function (He et al. 2020).

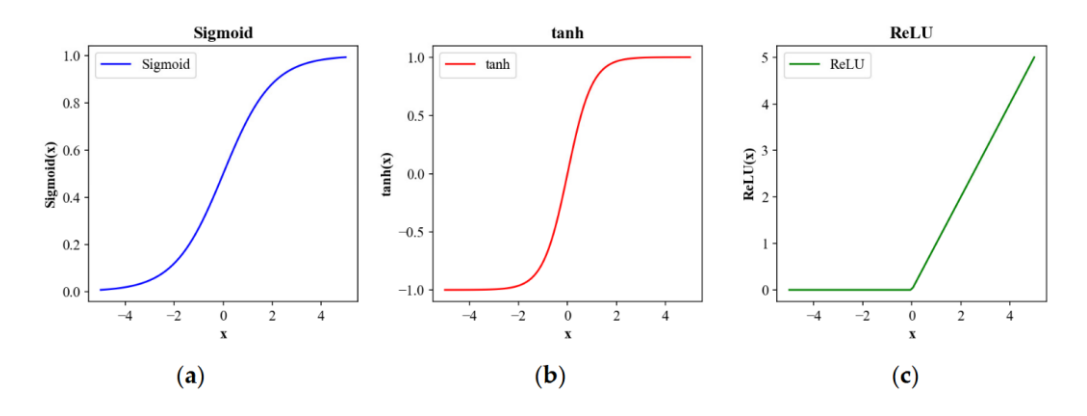


Figure 19. Illustration of activation transfer functions. (a) Sigmoid activation function; (b) *tanh* activation function; (c) *ReLU* activation function (Zhong et al. 2024).

Whereas the transfer functions between both the hidden layer and the input layer are nonlinear, the one between the output and hidden layers in the MLFFNN's NN technique is linear. Therefore, the output layer data is created by linearly integrating the performance results with a linear transfer function (*purelin*).

2 Objectives

The main objective of this work was to obtain an optimal and optimized model for the estimation of safety distances in case of HBNG horizontal jet fires from NG transmission pipelines. This address the need for risk assessments in hydrogen-blending applications, where a detailed CFD or semi-empirical consequence analysis (e.g., in PHAST) may be too time-consuming for real-time or iterative decision-making.

In order to accomplish this objective three secondary objectives have been defined:

- Analyse and review HBNG trends, applications, hazards and relevant changes in NG and jet-fires behaviour.
- 2. Create a synthetic and extensive database (50,112 cases) of jet fires scenarios from transmission pipelines using PHAST's Grid Consequences tool, after defining a suitable configuration. These results are going to be used for the dataset of point 4.
- 3. Develop a MLFFNN architecture and its training and validation loop based on these simulations and assess its predictive performance to estimate safety distances via an evaluation of his performance (MAE, MSE, R²).
- 4. Optimize the first version of the NN model through a sensitivity analysis on the hyperparameter, analysing the results from the scatter plots and the evaluative metrics.
- 5. Propose point of improvement and possible future works, useful to extend the efficiency and the operative range of the ML tool created.

3 Methodology

3.1 HBNG jet fires simulation

3.1.1 PHAST – Process Hazard Analysis Software Tool

Jet fires are simulated in this work using PHAST (Process Hazard Analysis Software Tool), which is a tool that offers capabilities for modelling various loss of containment scenarios, including discharge, dispersion, fires, explosions, and toxic effects. PHAST delivers key results through intuitive 2D graphs, immersive 3D views and comprehensive reports available in both Word and Excel formats (DNV 2025.).

The software relies on a comprehensive database of substances and enables users to create custom mixtures. Utilizing the multi-component modelling method, the software conducts rigorous thermodynamic calculations to determine mixture properties accurately. Users can specify various types of equipment, including pressure vessels, atmospheric storage tanks, long pipelines, and warehouses. For each equipment type users can define initiating events such as catastrophic ruptures, leaks, and line ruptures. Upon creating loss of containment scenarios, PHAST automatically assesses the type and magnitude of consequence effects. It performs calculations for discharge, pool vaporization, and dispersion, considering potential outcomes like jet fires, pool fires, flash fires, fireballs, and explosions. The software also supports a range of standalone models, which are used when the user has knowledge of the source term. In such cases, discharge and dispersion calculations are not performed. One of the main limitations is that, when simulating a catastrophic tank rupture, all the energy from the rupture is converted into overpressure, without accounting for the kinetic energy of the fragments, leading to an overestimation of the overpressure (DNV 2025).

The software workspace provides predefined parameters and weather conditions, but users have the flexibility to customize model parameters according to their requirements. Additionally, users can define new weather conditions by specifying atmospheric stability class and wind velocity. However, PHAST has constraints on simulating wind velocity. The software issues a warning for wind velocities below 1 m/s and does not allow simulations for wind speeds below 0.1 m/s.

3.1.2 Pseudo-validation of PHAST models

The first issue emerging in the simulation of horizontal HBNG jet fires from a leak in a transmission pipeline was how to simulate them using the PHAST software. Indeed, looking in the documentations available from DNV and their online tutorials, there is no "step by step" guide to follow for the simulation of jet fires of gas mixtures. Thus, it was decided to look in the validation documentation of the JFSH and radiation (RADS) models implemented in PHAST, and to try simulating experiments included there and from other sources with different configurations and checking the results obtained if they were in accordance with those presented in the documents (i.e., pseudo-validation).

In the validation document tests used hydrocarbons and other substances, such as H₂ and mixtures (e.g., H₂/CH₄ blends and syngas). Hole sizes covered a wide range and release conditions also varied, cover relatively slow jets and supersonic turbulent jets. Release orientation included vertical, horizontal and inclined releases (DNV 2023).

From this set of data and other experiments, DNV compared the predictions of two versions of Miller model: the original Miller one, which assumes jet flames to burn very close to the source, eliminating the lift off, and an updated version labelled Miller/DNV, which includes the lift off as calculated in Lowesmith and Hankinson (2012) equation (42). The conclusion was that overall the last version improves a bit the predictions for horizontal jet fires (DNV 2023).

Another comparison was conducted between Miller/DNV and Cone models (i.e. the Johnson model for horizontal jet fire) for non-hydrocarbon gases and mixtures of H₂/NG. According to Figure 20, significant underpredictions (by a factor of 2) were observed for horizontal releases with the Cone model. These are mainly caused by two factors: the under-predictive behaviour by the Johnson model of the fraction of radiated heat and the flame shape for H₂ releases simulated as frustrum cone. Additionally, predictions by the Miller/DNV model for vertical releases were also better than those from the Chamberlain model (results not shown here) (DNV 2023).

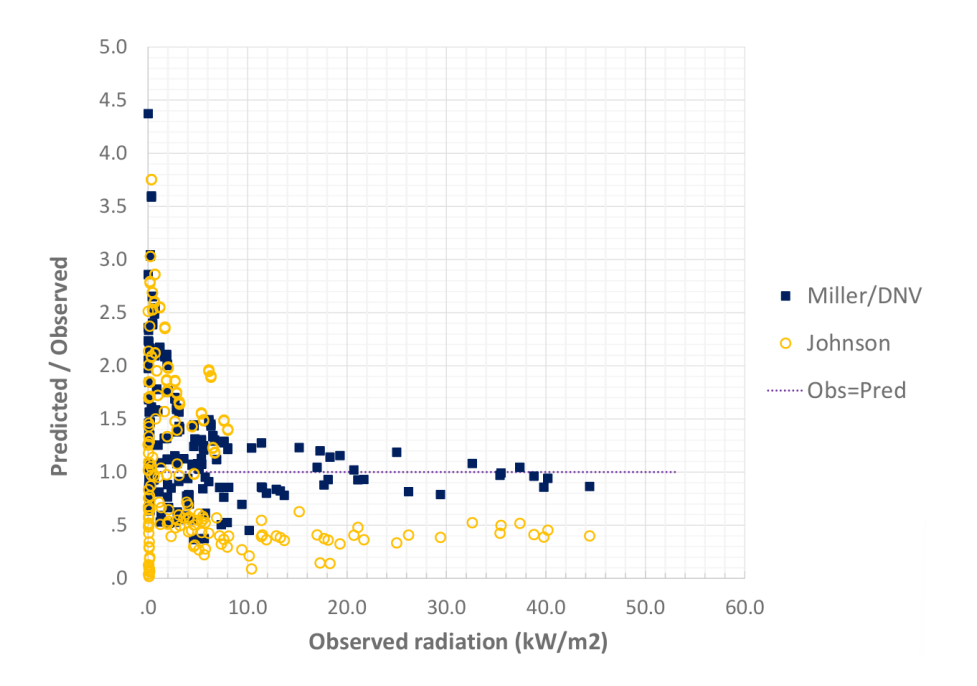


Figure 20. Comparison of the predictions by the Miller and the Cone model in PHAST for horizontal releases of H_2 and H_2 mixtures (DNV 2023).

According to Figure 21, the Miller/DNV model gives also good predictions for hydrocarbon releases, although the distribution of the datapoints is a bit wider than that of the Cone model. On the other hand, there are groups of outliers both for the Miller/DNV and the Cone models. These are indicated by the labels 'A' and 'B' in Figure 21. Points 'A' correspond to measurements taken behind the flame source closely aligned with the flame axis. Probably the overprediction is a result of all the radiation from the flame reaching the radiometer used in the experiments whereas, in reality, there is significant shielding of the radiation from the furthest points of the flame by the flame shape itself. The view factor approach of the frustrum cone overcomes this limitation. Group 'B' shows significant underprediction by the Cone model whilst the Miller/DNV model performs well. DNV concluded that there might be a range for hydrocarbon tests where the Miller model is preferable to the Cone model, but there is not enough data to define such ranges with confidence (DNV 2023).

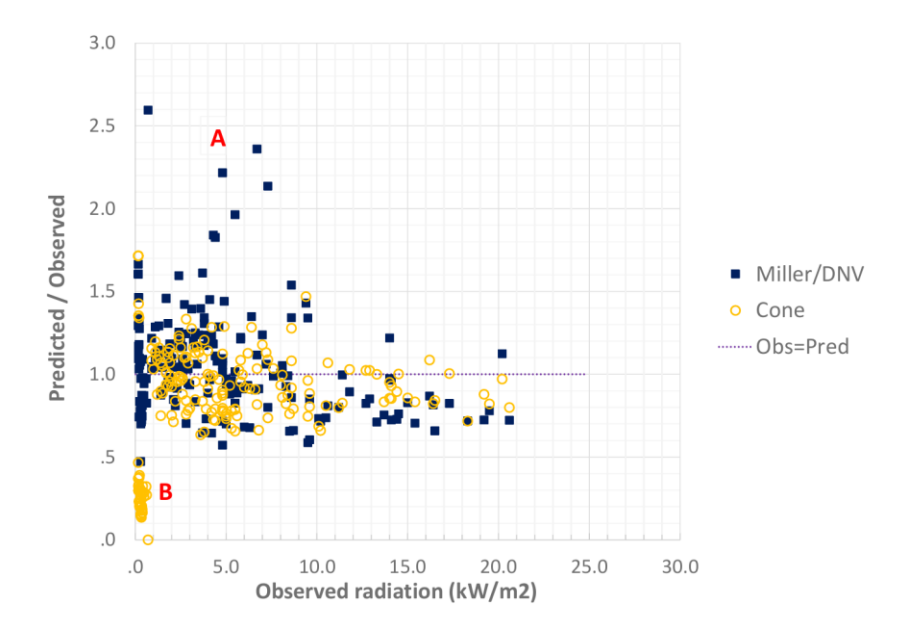


Figure 21. Comparison of the predictions between the Miller and the Cone models in PHAST for hydrocarbon releases (DNV 2023).

Indeed, the experiment from Lowesmith and Hankinson (2012), which was performed using a mixture of NG and 24 % vol. of H₂, provided comprehensive information about the experimental setup, the release pressure and the distance to the pipe target. Details about the experimental conditions are shown in Figure 12.

The results included the flame length, the lift off and the incident radiation (kW/m²), which was positive for the comparison of the best configuration in PHAST to simulate jet fires. The fraction of emissivity (F), which according to the PHAST documentation corresponds to the fraction of the maximum amount of heat that can be radiated from the surface of the flame, was also available.

Table 12. Test conditions and key results from (Lowesmith and Hankinson 2012).

Gas	dor	P _{release} (barg)	Distance to pipe (m)	dir _{wind}	u _{wind} (m/s)	m _{or} (kg/s)	MNP (MW)	L _f (m)	B (m)	F
NG	20	59.4	9.45	1±11S	6.3±1.5	2.9	140	19.8±1.6	6.0±0.8	0.137
NG	35	61.5	15.45	27±5S	6.2±0.5	9.4	462	37.8±2.9	7.5±1.1	0.179
NG	50	58.8	21.61	3±13N	3.6±0.5	18.4	939	49.9±2.9	8.7±0.9	0.202
Mix.	20	60.2	9.45	7±10N	2.7	2.7	137	17.6±1.1	5.8±0.4	0.130

Mix	35	60.8	15.45	14±6S	7.2	8.4	366	30.7±1.7	6.8±0.6	0.168
Mix	50	59.4	21.61	3±8N	16.9±0.1	16.8	860	45.2±2.5	7.2±0.6	0.168

 $P_{release}$ is the gauge pressure of the release, MNP is the Mean Net Power; L_f is the flame length; B is the flame lift off; F is emissivity fraction

The atmospheric temperature (3.4 °C), relative humidity (88%) and storage temperature (4.2 °C), which were not provided in the experiment used, were taken from a later study done also by Lowesmith and Hankinson (2013), assuming the two tests were performed at the same location and during the same period.

Table 13. Atmospheric parameters of the validation case Lowesmith and Hankinson (2013).

	Low	esmith and Ha	nkinson (2013) ambient cond	litions	
Air T (°C)	Stability class	Wind (m/s)	m/s) Solar radiation (kW/m²) Humidity (%)		
3.4	D	2.1	0.5	88	0.005

Four different configurations based on the type of discharge were tested to try to reproduce the results from Lowesmith and Hankinson (2012). These are shown in Table 14, i.e., Pressure vessel + Short pipe + Control valve; Pressure vessel + Short pipe + Relief valve; Pressure vessel + Leak; Long pipeline + Location Specific Break. The empty cells in this table correspond to possible inputs that were not required in that configuration.

Table 14. Possible configurations for jet fires in PHAST depending on the discharge type.

Feature		Pressure vessel								Long pipeline		
V inventory (m ³)	10	10	10	10	10	10	10	10	10	-	-	-
Temperature (K)	4.2	4.2	4.2	4.2	4.2	4.2	4.2	4.2	4.2	4.2	4.2	4.2
Pressure (barg)	60	60	60	60	60	60	60	60	60	60	60	60
Pipe length (m)	-	-	-	-	-	-	-	-	-	10	10	10

Pipe d _{int} (mm)	-	-	-	-	-	-	-	-	-	150	150	150
Discharge type	Short Pipe						Leak			Location specific break		
Valve type	Control valve			Relief valve			-	-	1	1	-	1
Pipe d _{int} (mm)	20	35	50	150	150	150	-	-	-	-	-	-
Pipe length (m)	1	1	1	1	1	1	-	-	-	-	-	-
Fixed m (kg/s)	2.7	8.4	16.8	-	-	-	-	-	-	2.7	8.4	16.8
Orifice diameter	-	-	-	20	35	50	20	35	50	20	35	50

Pure CH₄ was used in the calculations instead of a specific NG composition because this is the main constituent of the gas, as assumed in section 1.2.1. To calculate the physical and chemical properties of the CH₄-H₂ mixture the add-on PhastMC from PHAST was used (DNV 2025).

In PHAST, the default choice for the pressure vessel is a horizontal cylinder. It was decided to use 10 m³ as the volume of the gas mixture contained in the vessel in order to choose a single value valid for all configurations and to be close to the minimum limit allowed by PHAST, as this parameter only affects the release duration of the jet and not the final flame.

For the short pipe in the case of pressure vessels, the minimum length accepted by PHAST's default parameters was 1 m. Different lengths were tested but there were no differences in the flow rate and in the jet flame.

In Pressure Vessel + Leak and Long Pipeline + Location Specific Break configurations there is the possibility of fixing the discharge coefficient (C_D). In this case a value of 0.9 was chosen as indicated in the experimental data. However, in a similar study of jet fires from HBNG, such as the one by Pio Gianmaria et al. (2022) (results not shown here), it was observed that a higher accuracy was achieved when the calculation was performed automatically by the software. However, the values ranged between 0.87 and 0.96 in the simulations executed in this research.

The position of the Location Specific Break was set at the end of the Long Pipeline, for which the minimum length available of 10 m. As for the Short Pipe configuration, the length did not affect the discharged gas or the jet fire.

The elevation of the release at 3.25 m was the same for all configurations and this value was taken directly from Lowesmith and Hankinson (2012)

Figure 22 shows the results obtained after trying to reproduce the results from Lowesmith and Hankinson (2012). The closer the points are to the horizontal black dashed line, the better the agreement between the calculated and experimental values. According to this plot, the Miller model should be chosen to get better performances for estimating the fraction of emissivity and the frustrum lift off. However, the Cone model appears to be slightly better for predicting correct flame lengths but this is due to a large lift off when the orifice diameter and pressure are bigger. Regarding the four configurations, all of them get comparable results except for the configuration Pressure Vessel + Short Pipe + Relief Valve for the flame length and the fraction of emissivity. In this case higher values are obtained than those obtained with the other three configurations.

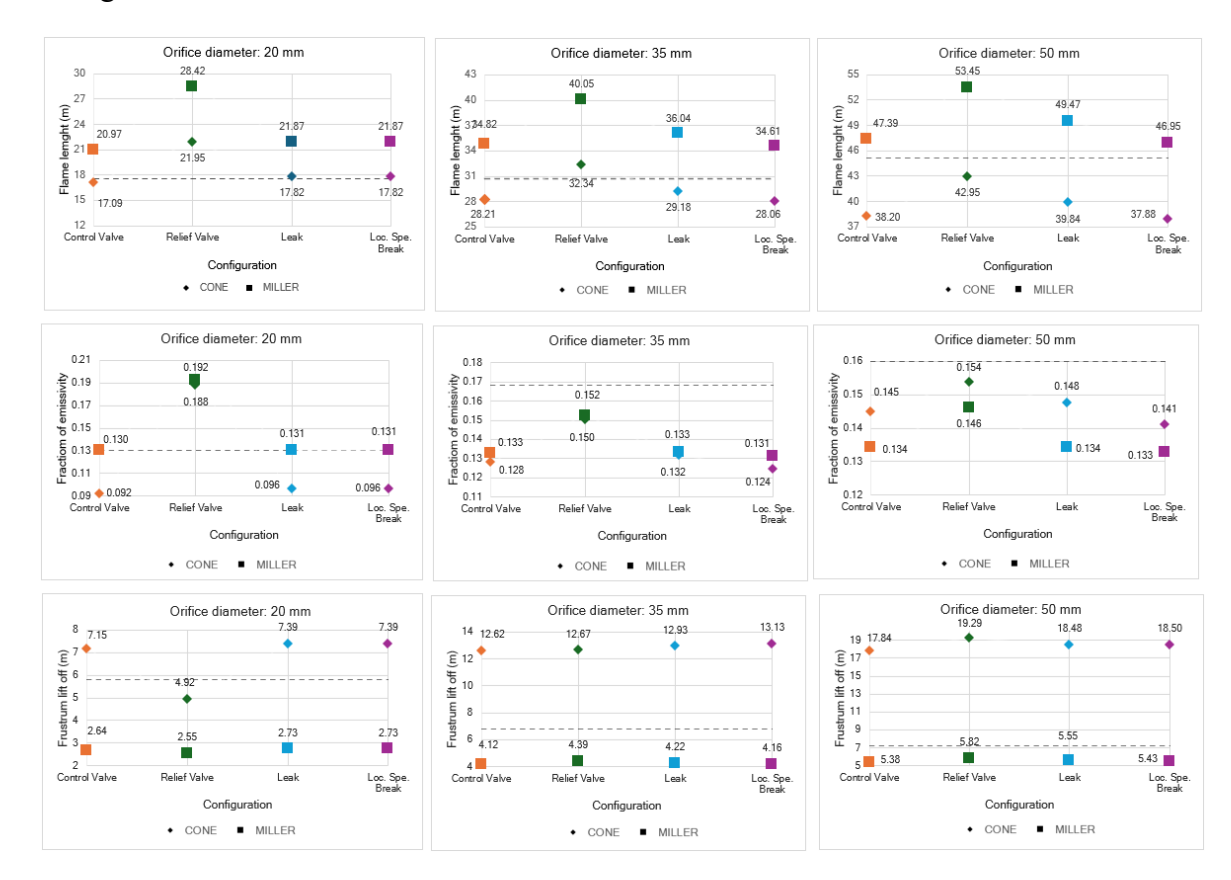


Figure 22. Flame length, fraction of emissivity and frustum lift off distance simulated for 20 mm, 35 mm, 50 mm orifice diameters with four different configurations: a horizontal pressure vessel with a control valve (orange; 1), relief valve (green; 2) or leak (light blue; 3); or a long pipeline with a specific location of the break (purple; 4). The

rhomboid points are from Cone model and the squared ones from Miller one. The black dotted line corresponds to the experimental values.

About the incident radiation, the experimental values were extracted from the measurements at different distances from the flame axis still collected in Lowesmith and Hankinson (2012) work (not shown here). The simulated results were collected in two subplots, where the distance to the flame axis is shown together with the radiation calculated using the four different configurations defined in PHAST. It appears that the pressure vessel with a relief valve is not the most suitable configuration for simulating incident radiation for the studied jet fires. Indeed, both in Cone and Miller models, it overestimates the values of flame length and fraction of emissivity for small diameters. Therefore, this configuration was discarded and focus shifted to the others (Figure 23).

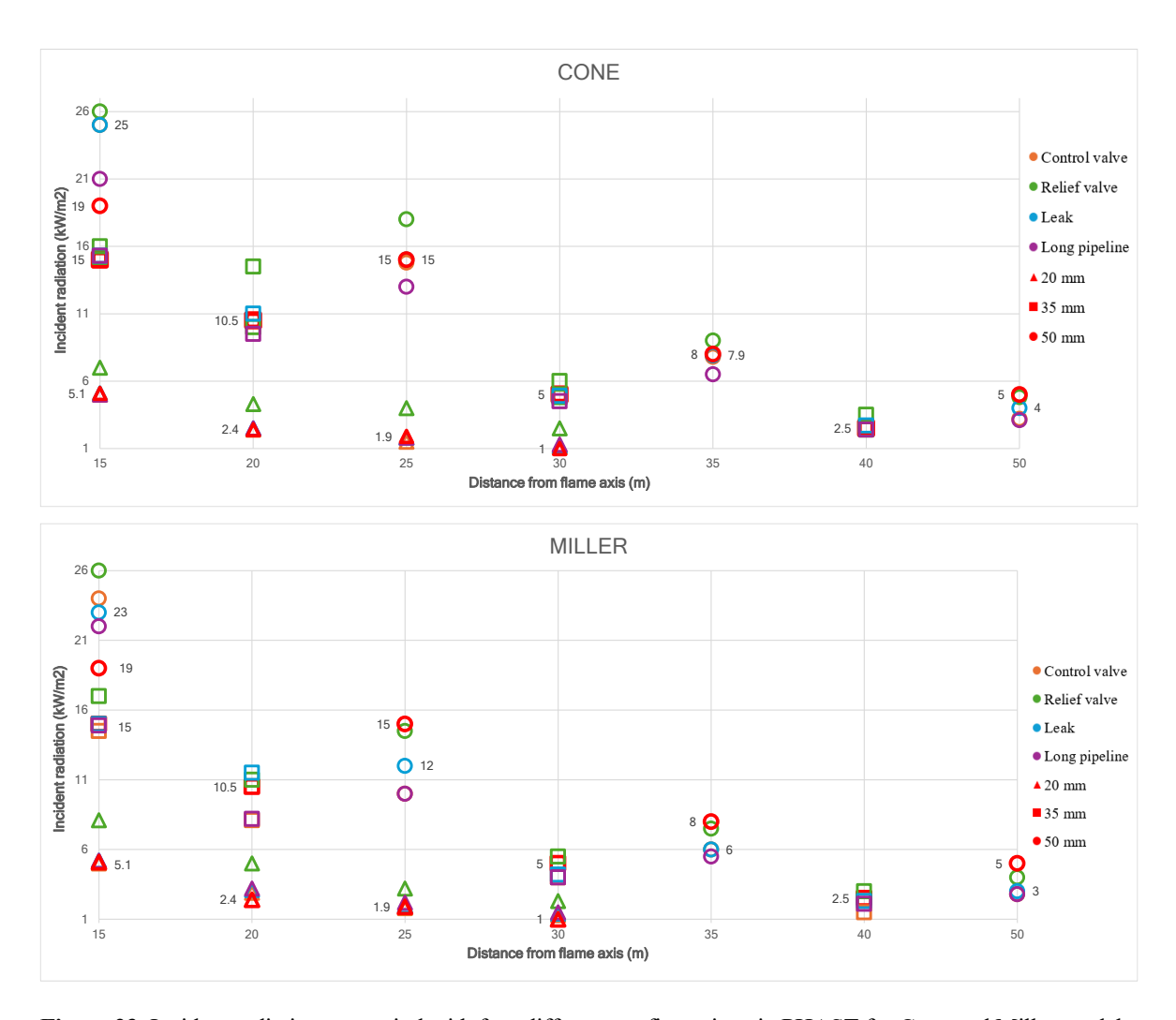


Figure 23. Incident radiation crosswind with four different configurations in PHAST for Cone and Miller models: control valve (pressure vessel), relief valve (pressure vessel), leak (pressure vessel), location specific break (long pipeline). The red markers are the experimental values for each orifice diameter: triangles for 20 mm, squares for 35 mm and circles for 50 mm.

To choose the final configuration from among the last three the predicted values over the observed ones were plotted as a function of the incident radiation (Figure 24). Based on this last comparison, it was decided to use Pressure Vessel + Leak with Miller/DNV model (ANNEX B) as the most reliable configuration.

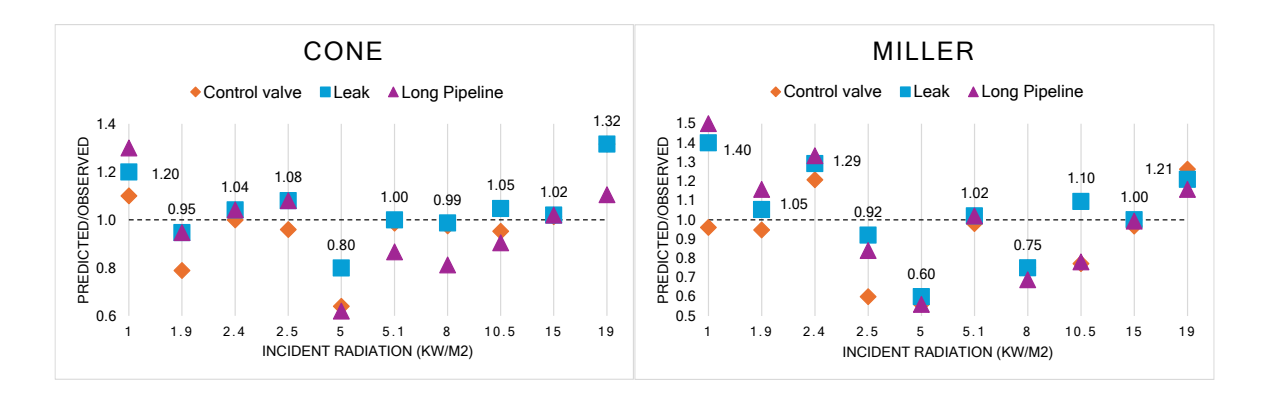


Figure 24. Predicted/observed value for incident radiations for the following configurations in PHAST: leak, control valve and location specific break in a long pipeline simulated with Cone and Miller model.

3.2 Workflow for designing a NN model

The work cycle for an integrated NN model design process includes five main steps, as shown in Figure 25.

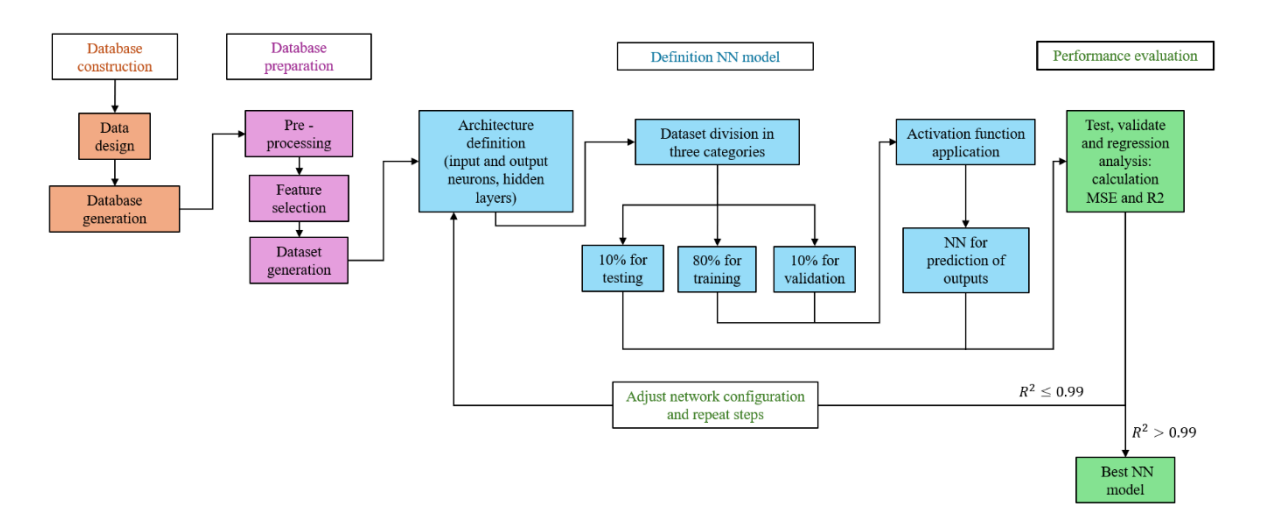


Figure 25. A schematic view of a NN work cycle model design.

The first step involves the Database construction gathering data from the many cases simulated by PHAST with the configuration of Pressure Vessel + Leak defined in section 3.1 and the parameters setup defined in the following section 3.3. In this way the jet flame data are defined and generated: composition of H_2 (% vol.), storage temperature (°C), storage pressure (barg),

elevation of release (m), jet fire mass rate (kg/s), flame length (m), distance to intervention zone (m), distance to alert zone (m), distance to domino effect (m), orifice diameter (m), wind (m/s), air temperature (°C), humidity (%), atmospheric stability).

Obtained the database it must be prepared before used it for training and validate the NN. The features (data values) are separated in input data (composition of H₂, storage temperature, storage pressure, elevation of release, orifice diameter, wind, air temperature, humidity, atmospheric stability) and output data (jet mass flow rate, flame length, distance to intervention zone, distance to alert zone, distance to domino effect). Before they could be used to generate a Dataset (a structured collection of data organized and stored together for analysis or processing) in PyTorch language (PyTorch 2025), the data are pre-processed (standardization) to prevent problem of overfitting in the NN training.

In the next stage, the network architecture is defined with the selection of the learning algorithms, number of layers and number of neurons for each one of them. The NN model training process is applied along with a network training validation on two different group of data from the dataset (training and validation batches). It includes network input and output adjustments through activation function and optimization algorithm (see section 3.6). At the end of the definition of the training model, the results are prediction of the original simulated values.

The performance of the trained model is evaluated using statistical criteria, including the coefficient of correlation (R^2) and the Mean Square Error (MSE) to compare the model outputs with the dataset. If the results are suitable (MSE \approx 0 and $R^2 \ge 0.99$), the best NN model for the topic case is obtained. Otherwise, the NN architecture could be optimized and the third step (definition NN model) repeated.

In the protracted research, several files and tools were used, starting from the Grid Consequence function present in the PHAST software (see section 3.3). From this last one, the obtained excel file serves as a basis for the creation of the database in JSON, containing all the simulated cases in a single format (see section 3.4). This file is used by a Python script, "Jet_fire_NN_original.py" for the definition, training and evaluation of the sketched NN model (see section 3.5 and section 3.6). After the Performance evaluation step (see section 3.7), the original model is optimized thanks to the script "Jet fire NN all optimization for test.py"

(see section 3.8) obtaining in the end the best NN model for horizontal HBNG jet fires from leaks in transmission NG pipelines.

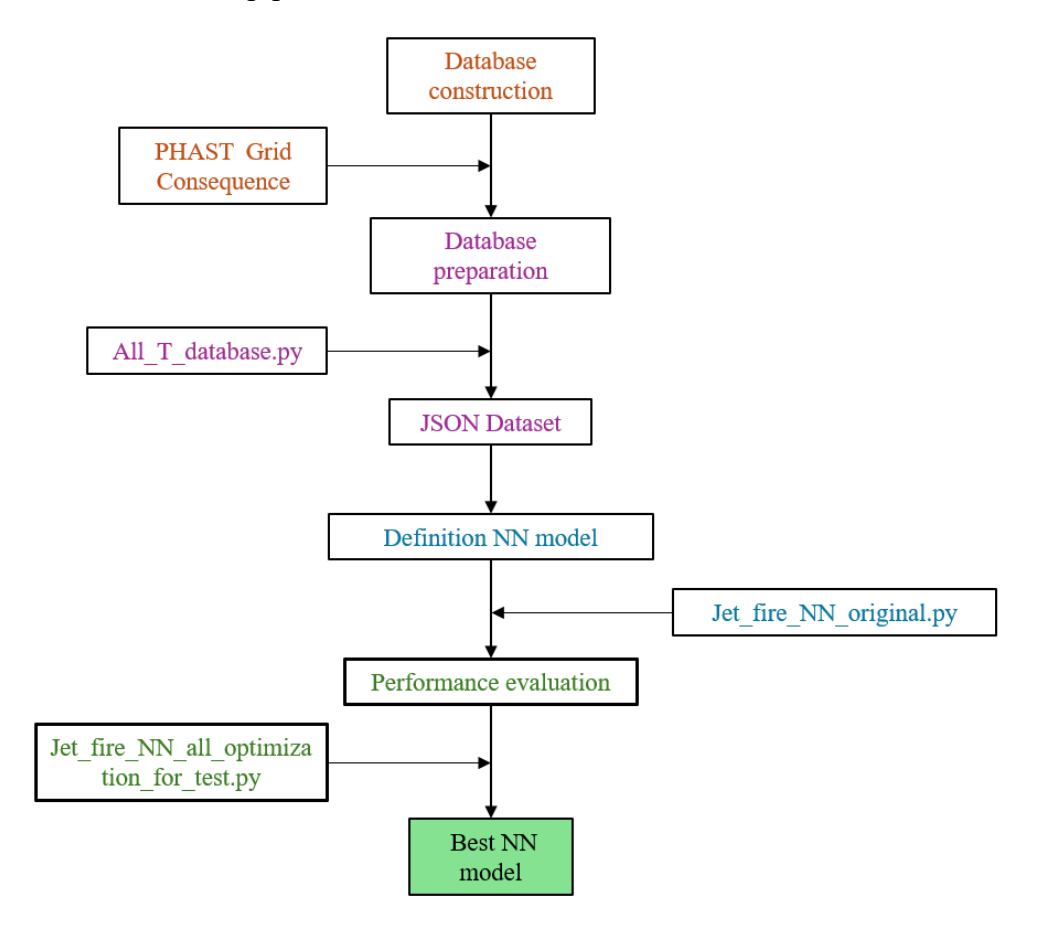


Figure 26. Main steps of the workflow for designing a NN model with the Python scripts applied in this research.

3.3 Database construction

From the simulations used for the further validation done for selecting the appropriate discharge configuration and jet fire model available in PHAST, the storage pressure, concentration of hydrogen and orifice diameter seemed to be the most impacting input parameter for the outputs. To get a predictive model of flame length and safety distances for HBNG horizontal jet fire from a transmission pipeline flame length, it was necessary to define the operative ranges of these parameter, those were going to be used in the NN.

To try to get the most suitable and wide range, the inlet pressures were set from 30 barg up to 150 barg, a bit higher the operating range of typical high-pressure gas transmission systems to

amplify the range (see section 1.1.4). Indeed, the pressure level of NG long-distance pipelines is usually high to meet the needs of long-distance transportation (Topolski et al. 2022). Cristello et al. (2023) summarize that transmission pipelines operate around 34.5 bar, with maximum allowable operating pressures (MAOP) often designed up to 100 - 140 bar for X-grade steels. Typical transmission line MAOPs for steel pipelines fall in the 30–150 bar range (e.g. API 5L X70 lines). Therefore, the set range lets to assess jet fires behaviour across a spectrum that covers lower-pressure city-gate releases up to worst-case transmission ruptures.

For the concentration of hydrogen in the simulated HBNG network, in "U.S.-applicable hydrogen blending guidance for a natural gas pipeline network based on network end-users", in general, only minor issues arise when blending less than 5% - 15% hydrogen by volume and that these low blend levels should not increase risks associated with end-use devices, public safety, or durability and integrity of the gas pipeline network (Melaina, Antonia, and Penev 2013). Pilot projects and feasibility studies typically target up to $\sim 20\%$ H₂ to avoid material, safety, or operational incompatibilities (Chae et al. 2022; Cristello et al. 2023). However, others have extended their numeric studies up to 30% of hydrogen to understand the nonlinear increase in flame speed, heat flux, and radiation intensity. By covering a composition range of 0% - 30% we capture both current industrial practice ($\leq 20\%$) and scenarios where hydrogen infrastructure and safety measures may allow higher blending.

Finally, regarding the orifice diameter, a range from 1 to 50 mm was chosen. This range allows to capture both the under-rim cracks and pinhole type leaks (~1 mm) up to more severe slot or gouge scenarios (~50 mm), ensuring the simulations cover the full envelope of expected release rates and resulting flame lengths. These values were already tested in precedent studies, such as in a CFD-based jet fire numerical study of HBNG pipelines where nozzle diameters of 5, 8, 11, 14, 17 and 20 mm were used (Zhang et al. 2025), and they were extended up to 50 mm to include also the conditions of experiments Lowesmith and Hankinson (2012) used for validating the simulation results.

The ambient related conditions are stability class, wind speed, ambient air temperature and humidity. By definition, stability class according to Pasquill classes (Luna and Church 1972) is a function of wind speed and solar radiation. Nineteen possible combinations between stability classes and wind speeds were examined to cover different atmospheric turbulence conditions. Three values for ambient air temperature were defined and they stem from 2022 Catalan

climatology data for minimum, average and maximum registered temperatures (Idescat 2023), which are representative for the Mediterranean type of climate.

A summary of the values used to generate the database are shown in Tables 15 and 16. Variables not included in these tables were kept constant.

Table 15. Database design (release parameters): Cat – categorical; N – Numerical; T – Temperature; P – Pressure; MW – Molecular Weight.

Leak from a pressure vessel with immediate ignition of a premixed HBNG							
Feature	Type	Value					
Concentration H ₂ (% vol.)	N	0	5	10	20	24	30
Ideal MW (g/mol)	N	16.04	15.36	14.68	13.31	12.78	11.95
Storage T (K)	N	268, 288, 308					
Storage P (barg)	N	30, 45, 50, 60, 70, 80, 100, 150					
Elevation of release (m)	N	3.25					
Orifice diameter (mm)	N	1, 5, 10, 20, 35, 50					

Table 16. Database design (atmospheric parameters): Cat – categorical; N – Numerical; T – Temperature; P – Pressure; MW – Molecular Weight.

Ambient related parameters														
Feature	Type		Value											
Air T (°C)	N		-5, 15, 35											
Stability class	Cat	A	I	В С				D (day)	1	D (night)	Е	F		
Wind (m/s)	N	1	1	2	3	5	7	8	5	6	8	2, 4, 6, 8	2, 3, 5	2, 3
Solar radiation (kW/m²)	N	0.9	0.9 0.3 0.9 0.3 0.5 0.9 0.9 0.3 0.5 0.5 0 0				0	0						
Humidity (%)	N		50, 70, 90											
Ground roughness (m)	N		0.005											

In total 50,112 combinations were simulated using PHAST software with the chosen configuration (leak from a pressure vessel with Miller model) and the input parameters already shown.

The software collects all the data useful for the consequence analysis through the command "Grid Consequence". This one creates an Excel file in which the main input parameters used (path, scenario, weather, hole size, material as the mixture of gas, storage temperature, storage pressure and the height of interest) and the outputs are displayed (ANNEX C).

For the studied cases, PHAST was operated three times for each of the atmospheric temperatures (-5 °C, 15 °C, 35 °C), because at in the high-pressure transmission pipeline, the storage temperature could be maintained at ambient temperature. Therefore, the simulated Pressure Vessel had three different storage temperature available. Each batch run in the program containing 16,704 cases (a third of the total ones) required 3 hours and 42 minutes with parallel calculations.

3.4 Database preparation

A Python script was created to extract only the columns of interest, perform unit conversions and categorical mappings, check data consistency, and finally write out a single JSON file containing all simulation cases in a uniform format.

Indeed, a single JSON file makes information easier to maintain, test and reuse in the following scripts, without running or inspecting again the original Excel files. It is a single source for all cleaned, unit-converted, and validated cases, and also any language or tool can read it (R, MATLAB or JavaScript).

In the "grid consequence" excel (ANNEX C) excels were extract the information corresponding to this field: "Path", "Scenario", "Weather", "Hole size (mm)", "Material", "Temperature (input) (degC)", "Pressure (input) (bar)", "Height of interest (coming from parameters) (m)", "Jet fire mass rate (kg/s)", "Flame length (m)", "Distance downwind to intensity level 1 (5 kW/m2) (m)", "Distance downwind to intensity level 2 (3 kW/m2) (m)", "Distance downwind to intensity level 3 (8 kW/m2) (m)" (see ANNEX C). In particular:

- The original "Material" column values were mapped to a numeric percentage of H₂ by volume.
- The ideal molecular weights were added and assigned to the corresponding mixture gas (0, 5, 10, 20, 24, 30 %vol of H₂).
- A number (1 to 7) for each atmospheric stability class (A, B, C, D, D night, E, F) because NN can process only numerical data and not categorical values.
- The denominations were changed to a more concise and consistent naming scheme.

```
661376
             "Scenario": "Leak 20 mm",
661377
             "Weather": "Lowesmith case",
661378
661379
             "Composition H2 (%vol)": 30,
661380
             "Storage T (degC)": 15,
             "Storage P (bar)": 50,
661381
             "Elevation of release (m)": 3.25,
661382
661383
             "Jet fire mass rate (kg/s)": 2.1378,
             "Flame length (m)": 19.1359,
661384
661385
             "Distance to intervention zone (5 kW/m2) (m)": 26.893,
661386
             "Distance to alert zone (3 kW/m2) (m)": 30.7623,
661387
             "Distance to domino effect (8 kW/m2) (m)": 24.1301,
661388
             "Pressure vessel": "30% vol 50 bar 15 degC",
             "Orifice diameter (m)": 0.02,
661389
             "Ideal MW (g/mol)": 11.95,
661390
             "Stability class": "D",
661391
             "Wind (m/s)": 2.1,
661392
             "Air T (degC)": 3.4,
661393
             "Humidity (%)": 0.88,
661394
             "Atm stability": 4.0
661395
661396
           },
```

Figure 27. Particular of the JSON script "all_T.json" created by the merged three excel files obtained by Grid consequence command in PHAST.

Then this file, was loaded by the script "Jet_fire_NN.py", which deal with the next steps: Definition NN model and Performance evolution.

3.4.1 Pre-processing

Before implementing the algorithms, a pre-processing operation was performed to examine the various ranges to prevent that any data could not be greater than others. One of the most

common pre-processing steps is standardization, called also "z-score scaling". If x is a single scalar measurement of one feature, then the standardized value z is computed as:

$$z = \frac{x - \mu}{\sigma} \tag{10}$$

Where μ is the sample mean of that feature in the training data:

$$\mu = \frac{1}{N_{train}} \sum_{i=1}^{N_{train}} x_i \tag{11}$$

and σ is the (unbiased) sample standard deviation in the training data:

$$\sigma = \sqrt{\frac{1}{N_{train}} \sum_{i=1}^{N_{train}} (x_i - \mu)^2}$$
 (12)

Once μ and σ for each feature are computed from the training set, the same formula is applied to every feature value in training, validation, and test. StandardScaler computes for each column of the training values the mean and the standard deviation. Then every original value x is replaced by z. By standardizing, every feature contributes roughly equally at the start of training. Also, the NN tuners, would converges more quickly when inputs are centred around zero with unit variance.

The outputs are standardized too, to makes the MSE loss more numerically stable and prevents one target from dominating the training if its scale is much larger than others. μ_y and σ_y are computed on the raw training targets. The network is trained to predict:

$$z_{y} = \frac{y - \mu_{y}}{\sigma_{y}} \tag{13}$$

After NN has produced these outputs (normalized), they are converted back to the original scale:

$$y = z_{\nu} \cdot \sigma_{\nu} + \mu_{\nu} \tag{14}$$

3.4.2 Feature selection and Dataset generation

After importing train_test_split (from sklearn.model_selection) and StandardScaler (from sklearn.preprocessing) the relative numerical values (Figure 27) for "Storage T (degC)", Storage P (bar)", "Elevation of release (m)", "Orifice diameter (m)", "Composition H2 (%vol)", "Ideal MW (g/mol)", "Wind (m/s)", "Air T (degC)", "Humidity (%)" and "Atm stability" were set as input; instead, "Jet fire mass rate (kg/s)", "Distance to alert zone (3 kW/m2) (m)", "Distance to intervention zone (5 kW/m2) (m)" and "Distance to domino effect (8 kW/m2) (m)" were defined as output.

"all_T.json" is read in a Pandas DataFrame. This DataFrame has one row for each simulated jet-fire case, with all numeric inputs and outputs. It gets polished eliminating redundant and purely textual rows and passed through a check: verify that every column can be cast to a numeric dtype (float or int) and if there are missing values; this guarantees that the DataFrame is ready for machine learning.

3.5 NN model definition

Python in Visual Studio Code

Python is a high-level programming language known for being designed to be easy to read and write, oriented features, and dynamic semantics. It offers built in data structures and supports dynamic typing and dynamic binding. Python's syntax promotes modularity and code reuse through support for modules and packages. Python comes with an extensive standard library that are available for free for major platforms. Python served as the backbone for data ingestion, preprocessing, model definition, training loops, and result visualization (Python 2010). Running Python code in an environment like Visual Studio Code notebooks allows interactive exploration of dataframes, rapid debugging, and inline plotting of intermediate results. The ease of writing concise scripts enabled quick iteration on preprocessing pipelines and neural network architectures.

PyTorch

PyTorch is an open-source machine learning framework that accelerates the path from research prototyping to production deployment. Built to offer maximum flexibility and speed, PyTorch supports dynamic computation graph. Its Pythonic design and deep integration with native Python tools make it an accessible platform for building and training deep learning models at scale. Widely adopted across academia and industry, PyTorch has become the framework of choice for commercial ML applications. It supports a broad range of use cases, from natural language processing and computer vision to reinforcement learning, through a robust ecosystem of libraries, tools, and integrations. PyTorch is also optimized for performance across CPUs, GPUs, and custom hardware accelerators, including support for distributed training and deployment on cloud platforms and mobile devices (PyTorch 2025). In this jet fire regression task, PyTorch was employed to define the multi-layer feedforward neural network, implement custom training loops, and leverage automatic differentiation for backpropagation.

3.5.1 Division of the data between training, validation and test

All these data were extracted as NumPy arrays and divided randomly into three distinguished sets, including training, validation, and test. The 80% of the total data points were used to determine the weights (the network training); 10% of the total data points were used to validate these weights (network validation); and 10% of the total data points were tested with the developed network, to provide an independent measure of the network performance during and after training.

3.5.2 NN Architecture

As explained before, MFLNN with consists of input layer, hidden layers and output layer, and adopts error-based back propagation algorithm. The learning rule is to use the fastest descent method. The weights and biases of the network are constantly adjusted through Backward Propagation to minimize the sum of squared errors of the network.

```
149
      class JetFireModelReg(nn.Module):
141
          def __init__(self, D_in=10, H1=32, H2=16, D_out=5, p_dropout=0.3):
142
              # D in = number of feature in input (10)
143
144
              # H
                    = number of neurons in each hidden layer
145
              # D_out = number of targets to predict (5)
                     = number of hidden layer
146
147
148
              super().__init__()
149
              self.net = nn.Sequential(
150
                  nn.Linear(D_in, H1),
                  nn.ReLU(),
151
                                                # regularisation
152
                  nn.Dropout(p_dropout),
                  nn.Linear(H1, H2),
153
154
                  nn.ReLU(),
                  nn.Dropout(p dropout),
155
                                                # linear output
156
                  nn.Linear(H2, D_out)
157
158
159
          def forward(self, x):
160
              return self.net(x)
161
```

Figure 28. Particular of "Jet_fire_NN.py" script to show the first architecture of the MLFFNN.

With PyTorch library is possible to use JetFireModelReg command, a subclass of nn.Module implementing a simple feedforward (multi-layer perceptron) for multi-output regression. The number of the precedent selected features will be constat for the input layer and the output one; 10 and 5 respectively. As first attempt the number of hidden layers was chosen as two and the number of the neurons for each of them was selected trying to simulate a pyramidal structure which helps for the regression. Therefore, the first one has 32 neurons and 16 are in the second layer. As explained in the section 1.4.2 the *ReLu* function is used between the input and the first hidden layer, and between the hidden ones. Instead, the *purelin* between the second hidden layer and the target (output) layer.

In the first attempts, the and R^2 results were too good (MSE \approx 0 and $R^2 \approx$ 1), pointing out a problem of overfitting. This phenomenon occurs when a model learns to reproduce not only the underlying signal but also the noise in the training data, so it performs poorly on unseen data. Thus, after each activation function, there's a "dropout" of 30% of the neurons, which prevent the overfitting during training by introducing randomness and forcing the network to be more robust.

Dropout is a regularization technique which randomly zero excludes from the training some hidden neuron's output with probability p (30% in this case) on every training step.

Later in the interference (evaluation) time the dropout is turned off and each weight is effectively scaled by (1 - p). In PyTorch that scaling is handled automatically so that at test time inputs are simply passed through the full network without zeroing anything out.

3.5.3 Setting up the DataLoader

Generally coding for processing data samples could get messy and hard to maintain, therefore PyTorch provides two data tools: torch.utils.data.DataLoader and torch.utils.data.Dataset.

A Dataset stores the samples and their corresponding labels, and DataLoader wraps an iterative set of data from the Dataset to enable easy access to the samples from the NN.

The Dataset recall dataset's features and labels one sample at a time. While training a model, the samples are put in "minibatches" and the data reshuffled at every passage in the training section to reduce model overfitting and use Python's multiprocessing to speed up data retrieval. DataLoader performs an iteration where the dataset is loaded and automates batching and shuffling. With shuffle=True, after all batches are iterated, the data is shuffled; necessary for the training DataLoader, not for the validation and testing ones (PyTorch 2025).

3.6 Training

The purpose of the build training loop in the NN is minimizing the Mean Squared Error (MSE) between the network's prediction and the true targets. A fundamental concept in NN training is the epoch: it refers to one complete pass of entire training dataset through the learning algorithm, and in a MLFFNN each training epoch has two parts: forward pass, and backward pass.

In forward pass, a batch of input vectors from the "test dataset" (80% if the total dataset) is fed through the network, layer by layer, to produce an output \hat{y} . The criterion function, also known

as the loss function \mathcal{L} , is calculated for reducing the error between the expected (from the experiments or the simulations with PHAST in this case) and the predicted values during forward propagation and can be expressed as:

$$\mathcal{L}(y, \hat{y}) = \frac{1}{N} \sum_{i=1}^{N} ||y_i - \hat{y}_i||^2$$
 (15)

Where \hat{y}_i is the true target for the sample i and y_i the one predicted from the NN over that batch set by the DataLoader.

In backpropagation the gradient of the MSE loss is calculated with respect to every weight in the network by propagating the error $\hat{y}^{(i)} - y^{(i)}$ backward through each layer. These gradients tell how each weight contributes to the loss. However, the backpropagation algorithm is slow to converge, and an overfitting problem may occur along with it.

Some regularization techniques (optimizer) have been developed to overcome these issues, such as Adam in this study, which constantly updates the weighted values between nodes in each layer:

$$w_{i+1} = w_i - \eta \frac{\partial \mathcal{L}}{\partial w} + \alpha (w_i - w_{i-1})$$
 (16)

Where w_{i+1} and w_i are the weights of the relative iteration, η is the learning rate, $\frac{\partial \mathcal{L}}{\partial w}$ is the gradient of the Loss function, α is a momentum coefficient.

In practice, Adam optimizer integrated through Equation (16) with adaptive learning rates and momentum terms tend to speed convergence and mitigate oscillations. Its adaptive steps tend to help prevent the network from fitting noise in the training set. In this study the baseline model is set using an optimizer with a learning rate of 10^{-3} and a weight decay option of 10^{-4} for further regularization.

After updating the weights, forward and backward passes is repeat on the next batch, continually reducing the network's mean squared error. Because backpropagation could overfit the training data an "early stopping action" is employed: monitoring the validation loss at the end of each epoch (Figure 29). In particular, with a patience of 10, if the loss does not improve

for ten consecutive epochs, the training is halt training, even if the maximum of 100 epochs is not reached yet.

```
model = JetFireModelReg(D_in=10, H1=32, H2=16, D_out=5, p_dropout=0.3).to(device)
195
196
197
     criterion = nn.MSELoss()
     optimizer = optim.Adam(
198
199
         model.parameters(),
         lr=1e-3,
201
         weight_decay=1e-4 # L2 regularization
202
203
204
     # Early stopping setup
205 import copy
206 patience = 10
      best_val_loss = float('inf')
208 best_model_wts = copy.deepcopy(model.state_dict())
209
     epochs_no_improve = 0
210
     num_epochs = 100
211
     for epoch in range(1, num_epochs+1):
212
213
         # — train -
        model.train()
        running_train = 0.0
215
216
         for Xb, yb in train_loader:
217
            Xb, yb = Xb.to(device), yb.to(device)
218
             optimizer.zero_grad()
            y_pred = model(Xb)
loss = criterion(y_pred, yb)
loss.backward()
optimizer.step()
219
220
221
222
             running_train += loss.item() * Xb.size(0)
223
        train_loss = running_train / len(train_loader.dataset)
224
         # - validation -
226
227
          model.eval()
228
         running_val = 0.0
          with torch.no_grad():
229
230
              for Xb, yb in val_loader:
                 Xb, yb = Xb.to(device), yb.to(device)
                  loss = criterion(model(Xb), yb)
232
                  running_val += loss.item() * Xb.size(0)
233
234
          val_loss = running_val / len(val_loader.dataset)
235
          print(f"Epoch {epoch:03d} Train Loss: {train_loss:.6f} Val Loss: {val_loss:.6f}")
236
237
          # - early stopping control-
          if val_loss < best_val_loss - 1e-6:</pre>
239
249
             best_val_loss = val_loss
241
              best_model_wts = copy.deepcopy(model.state_dict())
242
              epochs no improve = 0
          else:
243
244
              epochs_no_improve += 1
              if epochs_no_improve >= patience:
246
                  print(f"Early stopping at epoch {epoch}")
247
                  break
```

Figure 29. Training section of "Jet_fire_NN.py" script.

In the script extract shown in Figure 29 it is shown that the variable best_model_wts stores the optimum model weights for the lowest validation MSE seen so far and best_val_loss stores the

relative MSE results. In each epoch there is a validation section: model.eval disables dropout and other training-only behaviour, torch.no_grad context avoids computing gradients for validation (saving memory and computation), loops through val_loader, computes MSE on the model's predictions, and sum over the entire validation set.

3.7 NN performance evaluation

To recap the architecture proposed for the Multi-Layer Feedforward Neural Network with Backpropagation is one input layer with 10 neurons (inputs), two hidden layers with respectively 32 and 16 neurons, and an output layer of 5 features (outputs); 30% as percentage of dropout, function loss on MSE; Adam optimizer with learning rate 10⁻³ and weight decay 10⁻⁴; 100 epoch with early stepping control on MSE of 10⁻⁶ and patience 10.

The Mean Absolute Error, the Mean Square Error and the square of the correlation coefficient (R^2) were used as evaluation criteria to compare the model outputs with the evaluation dataset. MAE, MSE and R^2 were calculated as follows:

$$MAE = \frac{1}{N} \sum_{i=1}^{N} |y_i - \hat{y}_i|$$
 (17)

$$MSE = \frac{1}{N} \sum_{i=1}^{N} (y_i - \hat{y}_i)^2$$
 (18)

$$R^{2} = \frac{\sum_{i=1}^{N} (y_{i} - \hat{y}_{i})^{2}}{\sum_{i=1}^{N} (y_{i} - \hat{y}_{i})^{2}}$$
(19)

With the best_model_wts loaded, the model was valuated before on the saved 10% of the total data points; later is used the remaining 10% of the Dataset (test_loader) never used yet.

```
321 # Load the best weights
322 model.load_state_dict(best_model_wts)
323 model.eval()
324
325 # MSE on test_loader
326 test_mse = 0.0
     with torch.no_grad():
327
          for Xb, yb in test_loader:
329
             Xb, yb = Xb.to(device), yb.to(device)
             test_mse += criterion(model(Xb), yb).item() * Xb.size(0)
330
331 test mse /= len(test loader.dataset)
332 print(f"\nTest Loss (MSE): {test mse:.6f}")
333
     # Prediction on all X_test and metrics by target (all in real scale)
334
335
     with torch.no grad():
     y_test_pred_norm = model(X_test.to(device)).cpu().numpy()
337
     y_test_pred = scaler_y.inverse_transform(y_test_pred_norm)
338
339
     y_test_true = scaler_y.inverse_transform(y_test.cpu().numpy())
341
342 print("\nMetrics on TEST set (by target):")
     for i, name in enumerate(target_cols):
343
          mae_i = mean_absolute_error(y_test_true[:,i], y_test_pred[:,i])
345
          mse_i = mean_squared_error(y_test_true[:,i], y_test_pred[:,i])
         r2_i = r2_score(y_test_true[:,i], y_test_pred[:,i])
346
347
         print(f"\{name\}: \ MAE=\{mae\_i:.3f\}, \ MSE=\{mse\_i:.3f\}, \ R2=\{r2\_i:.3f\}")
```

Figure 30. Performance evaluation extract of "Jet fire NN.py" script.

3.8 Optimization of the MLFFNN with BP

A first MLFFNN with BP model was developed and used as a baseline model. The architecture and model parameters used were the following ones:

- One input layer with 10 neurons.
- Two hidden layers with 32 and 16 neurons, respectively.
- An output layer with 5 neurons.
- Activation function: *ReLU*.
- Dropout rate: 30%.
- Batch size in the validation section: 32.
- Adam optimizer with a learning rate of 10^{-3} and a weight decay of 10^{-4} .
- 100 epochs with early stepping control on MSE of 10⁻⁶ and a patience value of 10.

Afterwards, an optimization on several architecture and model parameters was performed to optimize the baseline MLFFNN with BP model using as loss function MSE. The analysis was performed considering 3 sections of the NN architecture:

- (1) Model definition: to see how the networking capacity impacts on the validation loss. Several parameters were tested:
 - Network geometries: 4 architectures with two hidden layers but with different number of neurons for each one, i.e. (16, 8) (32, 16), (64, 32), (128, 64); 1 architecture with 1 hidden layer with 48 neurons; 1 architecture with three hidden layers with 32, 16 and 8 neurons, respectively.
 - Activation functions: *ReLU*, *LeakyReLU*, *ELU*, *tanh*.
 - Dropout rates: 0, 10, 30, 50%.
- (2) DataLoader creation: to analyse how changing the size of the batches in the validation section influence the results, because smaller batches provide noisier gradients, while larger batches yield smoother updates but require more memory.
 - Batch sizes tested: 16, 32, 64, 128.
- (3) Training loop: to analyse if a higher learning rate could lead every gradient step to overshoot the loss minimum and if is necessary to keep weights smaller to reduce model complexity and improve generalization on unseen data; to study the fact that a shorter patience may avoid overfitting but could also stop training prematurely.
 - Learning rate $(10^{-2}, 10^{-3}, 10^{-4})$ and weight decay $(0, 10^{-5}, 10^{-4}, 10^{-3})$ of the optimizer.
 - Early stopping patience: 5, 10, 20.

The best option among all the ones tested was defined and implemented.

4 Results

4.1 Simulation in PHAST

To get a comprehensive report of the results obtained for HBNG jet fires Pressure Vessel + Leak with Miller/DNV model, here are shown only the grid-consequence results with the weather conditions of Table 16.

The first three column charts (Figure 35, 36, 37), represent the release mass flow rate (kg/s), the flame length (m) and the safety distances according to three vulnerability levels based on radiation thresholds (m), at a fixed storage pressure of 60 barg, storage temperature of -5 °C, and changing the orifice diameter (1, 5, 10, 20, 35, 50 mm) with the volumetric composition of blended hydrogen in the natural gas (0, 5, 10, 20, 24, 30 % vol.). A single, fixed colour is used to represent each composition.

According to these results, increasing the presence of H_2 in natural gas decreases the release mass flow rate, the flame length and the incident radiation in every diameter orifice case. This is in agreement with the introductive part (see section 1.3.1). On the contrary, enlarging the leak increases the quantities for a given composition.

For the release mass flow rate (Figure 31), the values go from a minimum value of 0.0067 kg/s for a mixture of H₂ 30% vol. with an orifice diameter of 1 mm to a maximum of 20.65 kg/s with only methane gas with an orifice diameter of 50 mm, which decreases to 19.96 kg/s by adding 5% vol. of H₂. The flame length (Figure 32) for the reasons already explained goes from 1.39 m with 30% vol. of H₂ and 1 mm orifice to 53.46 m with only methane and an orifice of 50 mm, or to 52.57 m for a 5% vol. of H₂. Following the same pattern, the minimum and maximum for the safety distances (Figure 37) are 2.012 m and 87.26 m (85.94 m for 5% vol. of H₂) in the alert zone, 1.79 m and 75.52 m (74.6 m for 5% vol. of H₂) in the intervention zone, 1.64 m and 67.35 m (66.38 m for 5% vol. of H₂) in the domino effect one.

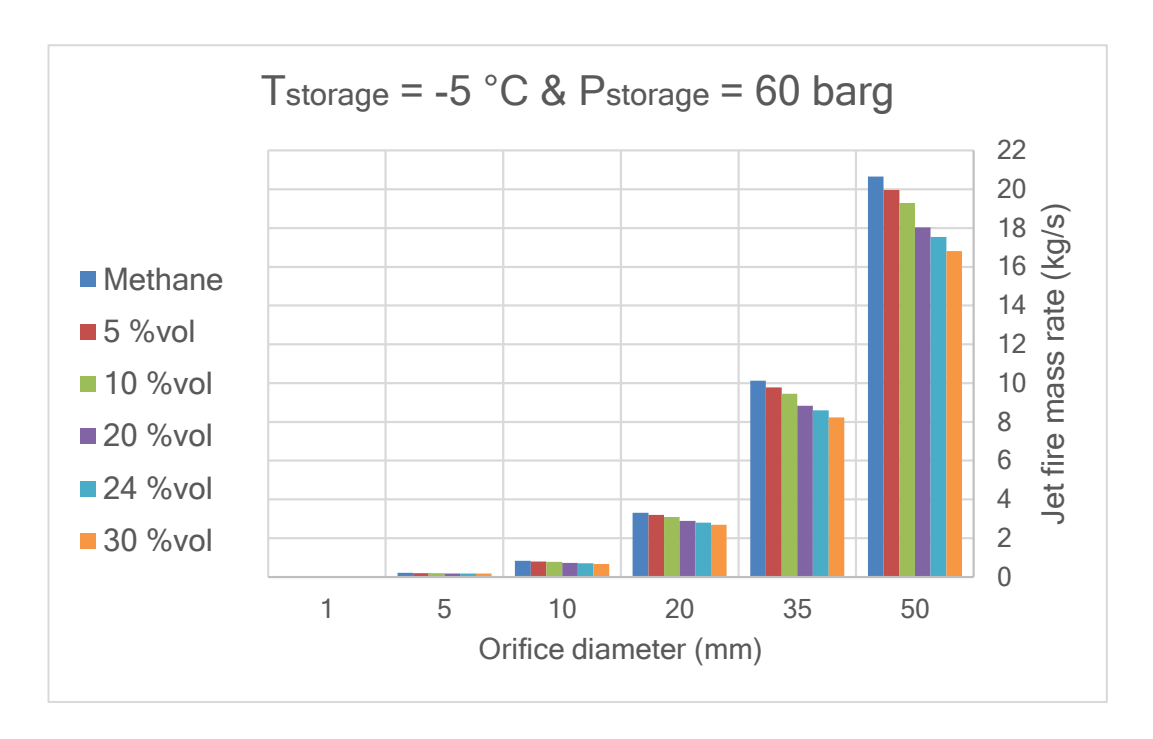


Figure 31. Release mass flow rate (kg/s) results obtained using PHAST for a setup jet fire with storage pressure of 60 barg and storage temperature of -5 °C considering different orifice diameters (1, 5, 10, 20, 35, 50 mm) and different hydrogen compositions (0, 5, 10, 20, 24, 30% vol.) in methane.

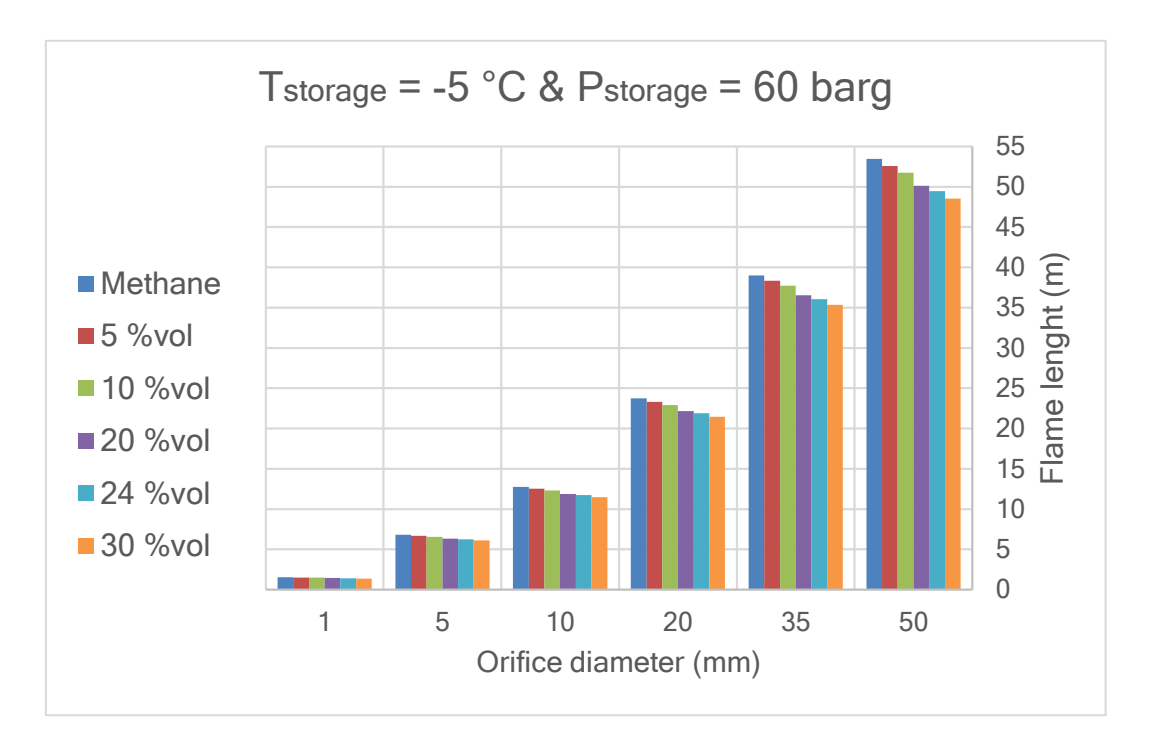


Figure 32. Flame length (m) results obtained using PHAST for a setup jet fire with storage pressure of 60 barg and storage temperature of -5 °C considering different orifice diameters (1, 5, 10, 20, 35, 50 mm) and different hydrogen compositions (0, 5, 10, 20, 35, 50% vol.) in methane.

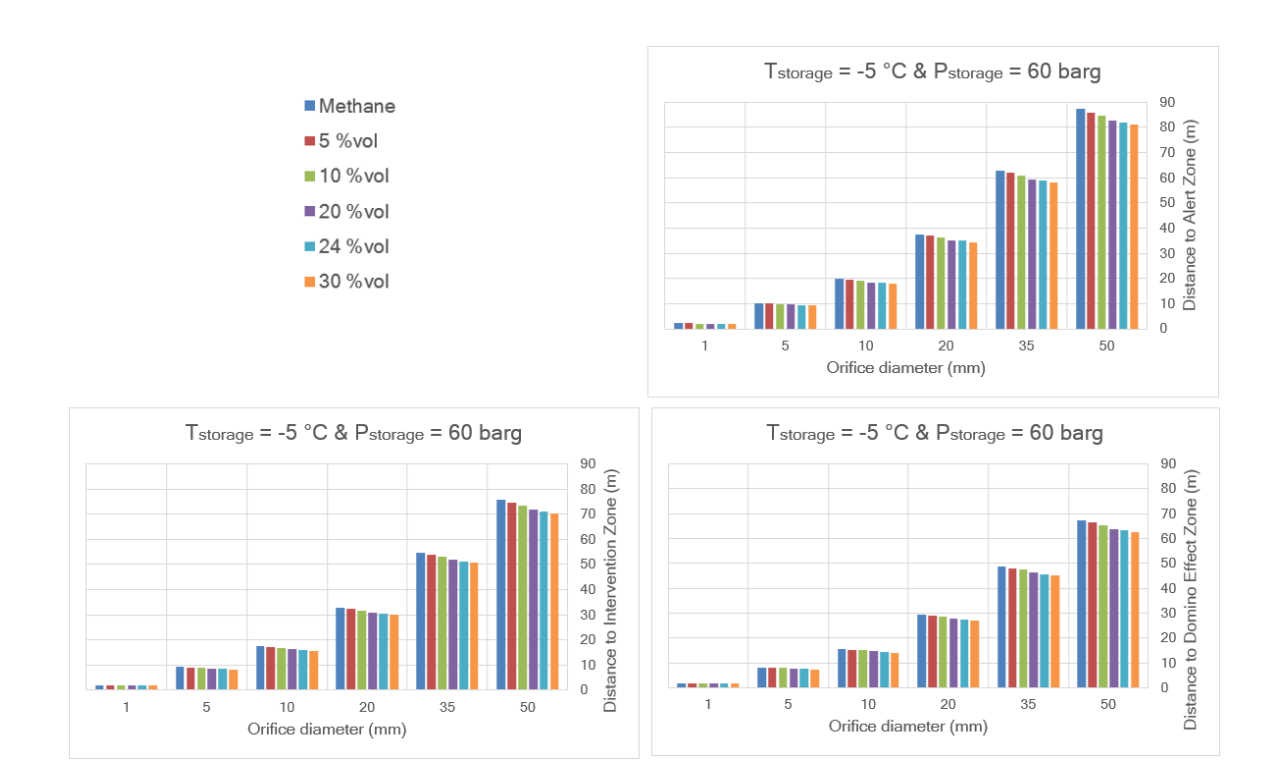


Figure 33. Distance crosswind to intensity level of 3 kW/m² (alert zone), 5 kW/m² (intervention zone), 8 kW/m² (domino effect zone) obtained using PHAST for a setup jet fire with storage pressure of 60 barg and storage temperature of -5 °C considering different orifice diameters (1 ,5, 10, 20, 35, 50 mm) and different hydrogen compositions (0, 5, 10, 20, 35, 50% vol.) in methane.

In Figures 34, 35 and 36 the jet fire outputs considered before are shown considering different orifice diameters, fixing the volumetric composition of hydrogen (24 % vol.) and the storage temperature (-5 °C) and changing, instead, the storage pressure (30, 45, 50, 60, 70, 80, 100, 150 barg). As before, the composition of 24% vol. of H₂.

The storage pressure, as the orifice diameter, has a large influence on the results obtained on each output variable. In Figure 38, it can be observed that the release mass flow rate goes from 0.0035 kg/s (30 barg, 1 mm) to 45.76 kg/s (150 barg, 50 mm). These differences in the release flow rate have consequences on the flame length, with a minimum value of 1.02 m (30 barg, 1 mm) to a maximum value of 75.08 m (150 barg, 50 mm) (Figure 39). The same trend is noted in Figure 40, where the minimum and maximum for the safety distances are 1.48 m and 126.48 m in the alert zone, 1.31 m and 109.50 m in the intervention zone, 1.27 m and 97.14 m in the domino effect one.

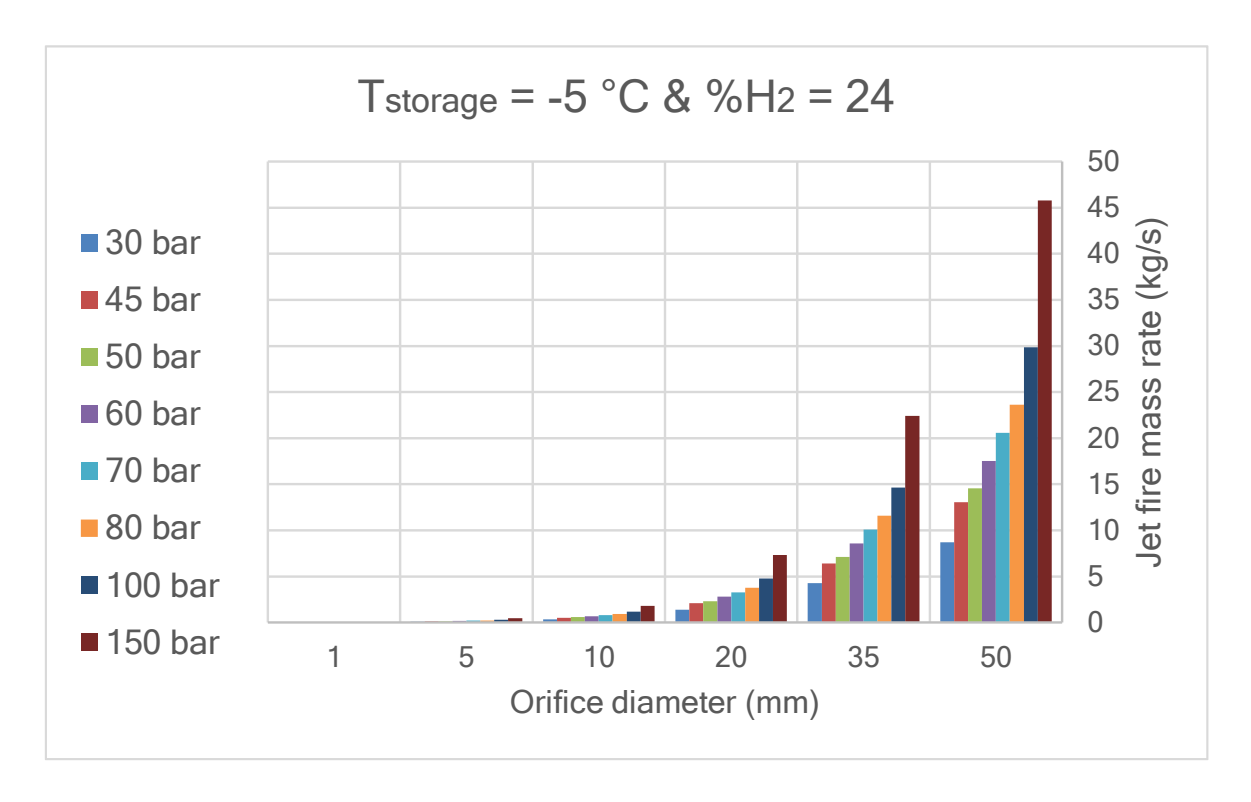


Figure 34. Release mass flow rate (kg/s) results obtained using PHAST for a setup jet fire with a hydrogen composition of 24% vol. and a storage temperature of -5 °C considering different orifice diameters (1, 5, 10, 20, 35, 50 mm) and different storage pressures (30, 45, 50, 60, 70, 80, 100, 150 barg).

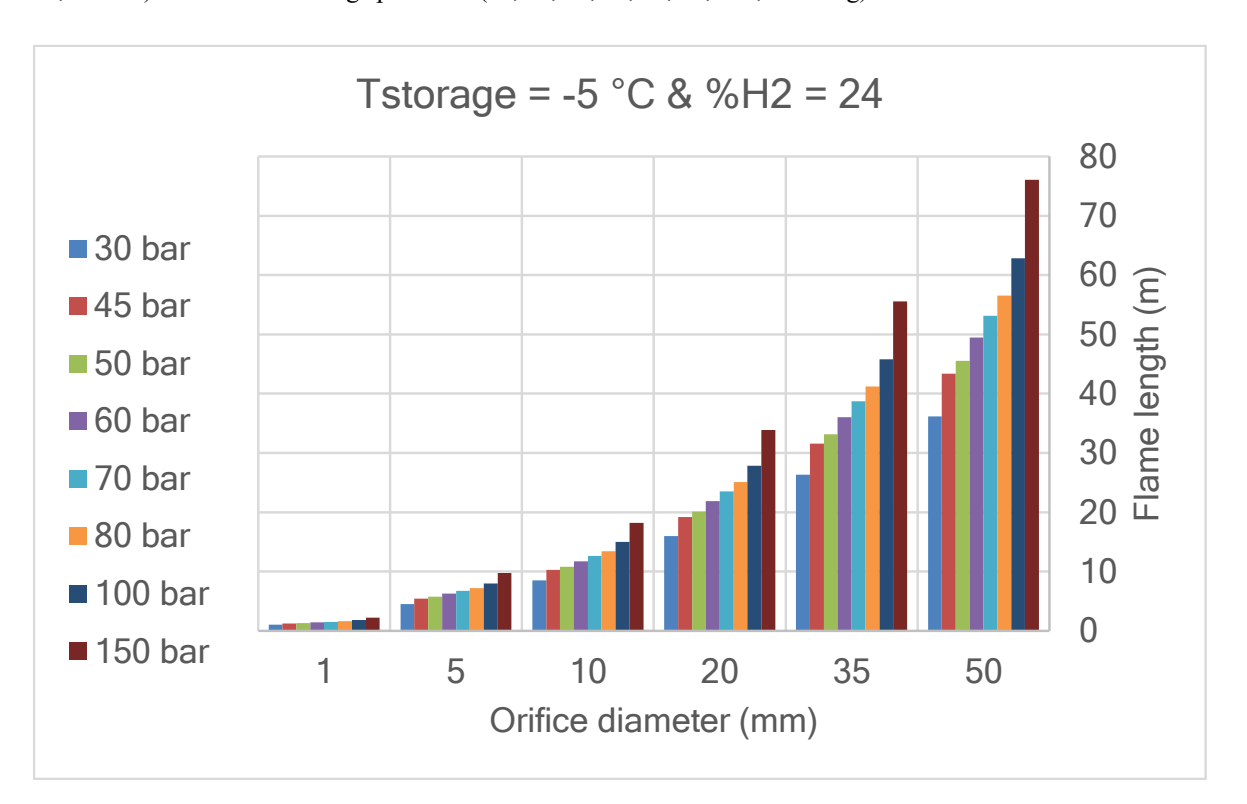


Figure 35. Flame length (m) results obtained using PHAST for a setup jet fire with a hydrogen composition of 24% vol. and a storage temperature of -5 °C considering different orifice diameters (1, 5, 10, 20, 35, 50 mm) and different storage pressures (30, 45, 50, 60, 70, 80, 100, 150 barg).

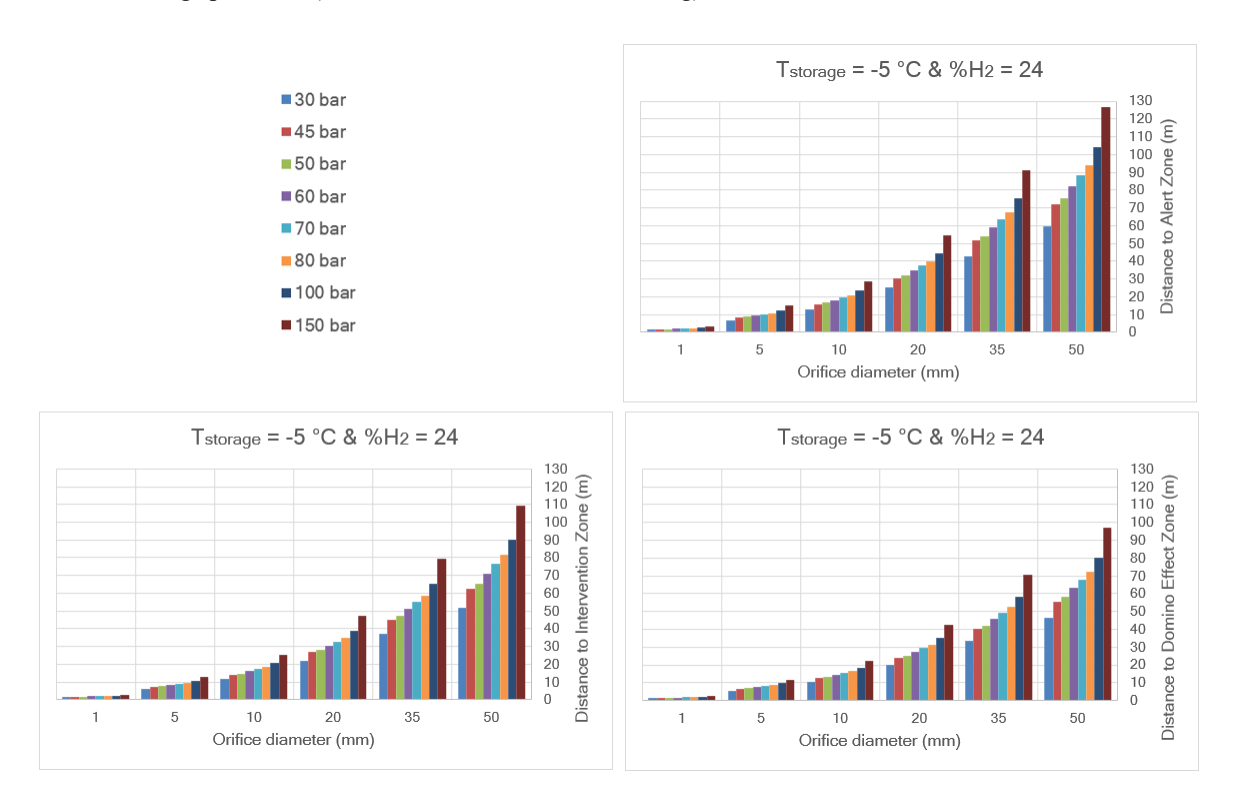


Figure 36. Distance crosswind to intensity levels of 3 kW/m² (alert zone), 5 kW/m² (intervention zone), 8 kW/m² (domino effect zone) obtained using PHAST for a setup jet fire with a hydrogen composition of 24% vol. and a storage temperature of -5 °C considering different orifice diameters (1, 5, 10, 20, 35, 50 mm) and different storage pressures (30, 45, 50, 60, 70, 80, 100, 150 barg).

Regarding the influence of the storage temperature in the Pressure Vessel + Leak configuration to simulate HBNG horizontal jet fire, in ANNEX D are collected the results for 15 and 35 °C.

Increasing this temperature corresponds to a decreasing of the release mass flow rate, the flame length and the intensity irradiation both in the cases with fixed storage pressure (60 barg) and the ones with fixed concentrations (24 %vol.), following the same behaviour already plotted in this section.

Considering the results from all 50,112 cases simulated, the minimum values correspond to $T_{storage} = 35$ °C, $P_{storage} = 30$ barg and 30 % vol. of H_2 conditions; and the maximum ones to

 $T_{storage} = -5$ °C, $P_{storage} = 150$ barg and 0% vol. of H_2 conditions. The respective min and max values for each condition are:

- Release mass flow rate: 0.003 kg/s and 55.541 kg/s.
- Flame length: 0.940 m and 83.960 m.
- Distance crosswind to intensity level 3 kW/m² for 30 seconds "Alert zone" (m): 1.374 m and 138.750 m.
- Distance crosswind to intensity level 5 kW/m² for 30 seconds "Intervention zone" (m):
 1.222 m and 119.917 m.
- Distance crosswind to intensity level 8 kW/m² for 30 seconds "Domino effect zone"
 (m): 1.198 m and 106.090 m.

4.2 Performance evaluation of the MLFFNN with Backpropagation

A preview of the 2-dimensional data structure (i.e., DataFrame) before exporting it into a JSON file format is shown in Figure 37.

Anteprima Dat	aFrame:										
Scenario	Weather	Composition H2 (%vol)	Storage T (degC)	Storage P (bar)	Elevation of release (m)	 Ideal MW (g/mol)	Stability class	Wind (m/s)	Air T (degC)	Humidity (%) At	m stability
0 Leak 1 mm	Lowesmith case	0	-5	30	3.25	 16.04	D	2.1	3.4	0.88	4.0
1 Leak 1 mm	A-15_50	0	-5	30	3.25	 16.04	A	1.0	-5.0	50.00	1.0
2 Leak 1 mm	A-15_70	0	-5	30	3.25	 16.04	A	1.0	-5.0	70.00	1.0
3 Leak 1 mm	A-15_90	0	-5	30	3.25	 16.04	A	1.0	-5.0	90.00	1.0
4 Leak 1 mm	B-15_50	0	-5	30	3.25	 16.04	В	1.0	-5.0	50.00	2.0
[5 rows x 19	columns]										

Figure 37. Extract in Visual Code (Python) of the DataFrame.

Showing the training epoch of the NN (Figure 38), there was an early stop at epoch 22, meaning that the function loss (based on the MSE) did not get better results for 10 consecutive epochs (i.e., patience was set at 10), so the maximum of 100 epochs was not reached. At the end of each training section and validation the target values were transformed back to their original physical units to invert the standardisation applied (see section 3.4.1)

```
Epoch 001 Train Loss: 0.209893 Val Loss: 0.014374
Epoch 002 Train Loss: 0.089765 Val Loss: 0.013987
Epoch 003 Train Loss: 0.081226 Val Loss: 0.010566
Epoch 004 Train Loss: 0.079325 Val Loss: 0.022211
Epoch 005 Train Loss: 0.076681 Val Loss: 0.013915
Epoch 006 Train Loss: 0.074862 Val Loss: 0.020215
Epoch 007 Train Loss: 0.073798 Val Loss: 0.010094
Epoch 008 Train Loss: 0.073931 Val Loss: 0.009401
Epoch 009 Train Loss: 0.072672 Val Loss: 0.007622
Epoch 010 Train Loss: 0.072788 Val Loss: 0.009421
Epoch 011 Train Loss: 0.072767 Val Loss: 0.006994
Epoch 012 Train Loss: 0.072552 Val Loss: 0.005826
Epoch 013 Train Loss: 0.071924 Val Loss: 0.007758
Epoch 014 Train Loss: 0.072430 Val Loss: 0.007570
Epoch 015 Train Loss: 0.069980 Val Loss: 0.008833
Epoch 016
          Train Loss: 0.071602 Val Loss: 0.008462
Epoch 017 Train Loss: 0.071287 Val Loss: 0.009633
Epoch 018 Train Loss: 0.069992 Val Loss: 0.006118
Epoch 019 Train Loss: 0.070721 Val Loss: 0.006647
Epoch 020 Train Loss: 0.071711 Val Loss: 0.013313
Epoch 021 Train Loss: 0.070597 Val Loss: 0.007098
Epoch 022 Train Loss: 0.070591 Val Loss: 0.012098
Early stopping at epoch 22
```

Figure 38. Extract in Visual Code (Python) of the training calculations for the proposed Neural Network.

Once the training was completed, the NN model was evaluated on the testing dataset, with the weights corresponding to the lowest loss function results (related with MSE values) and obtained during the valuations. Therefore, the results shown in Table 17 and the scatter-plots on testing dataset (Figures 39 and 40) refer to the best configuration of the original NN using the architecture summarized in section 3.7

Before proceeding with the test evaluation, the predicted outputs are converted back to the original scale (see section 3.4.1). Therefore MAE, MSE and R² have the relative units.

Table 17. Statistical metrics (MAE, MSE, R^2) obtained using the weights corresponding to the lowest loss function results in the proposed NN.

Feature	MAE	MSE	\mathbb{R}^2
Release mass flow rate (kg/s)	0.574 kg/s	$1.412 \text{ kg}^2/\text{s}^2$	0.985
Flame length (m)	1.144 m	1.894 m ²	0.995
Distance (m) at intensity level of 8 kW/m ² (domino effect zone)	1.636 m	3.900 m ²	0.995
Distance (m) at intensity level of 5 kW/m² (intervention zone)	1.898 m	5.436 m ²	0.995
Distance (m) at intensity level of 3 kW/m² (alert zone)	1.454 m	3.011 m ²	0.995

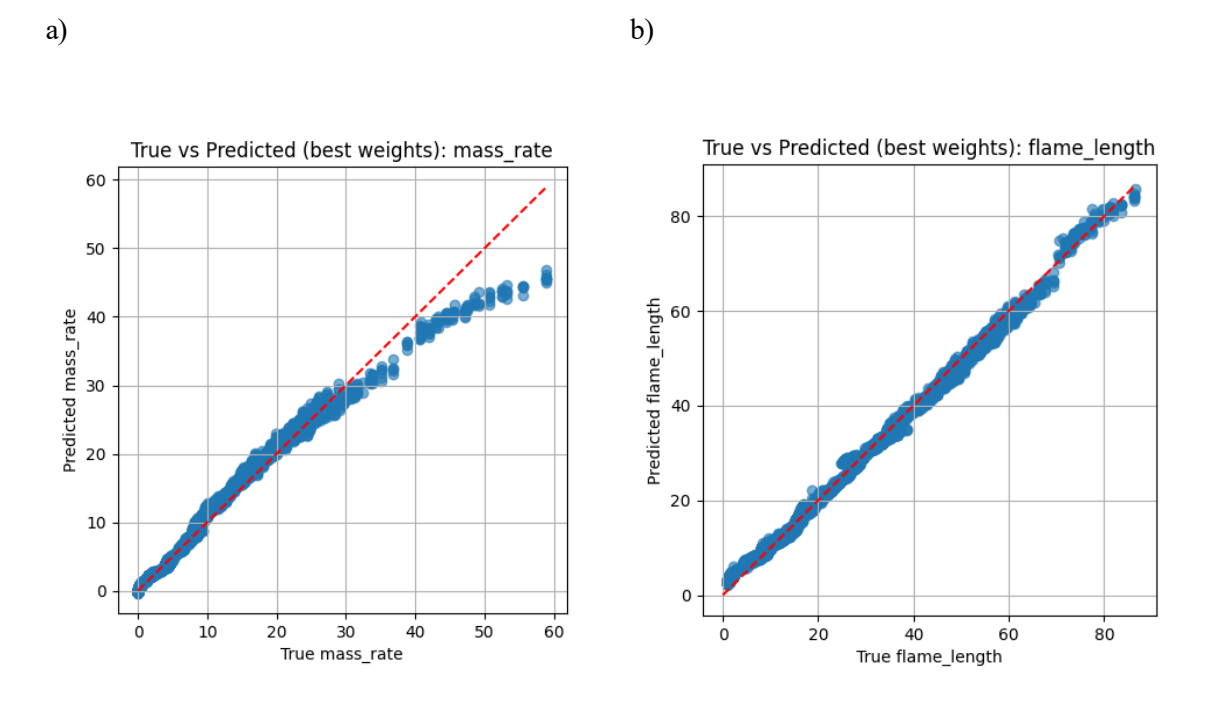
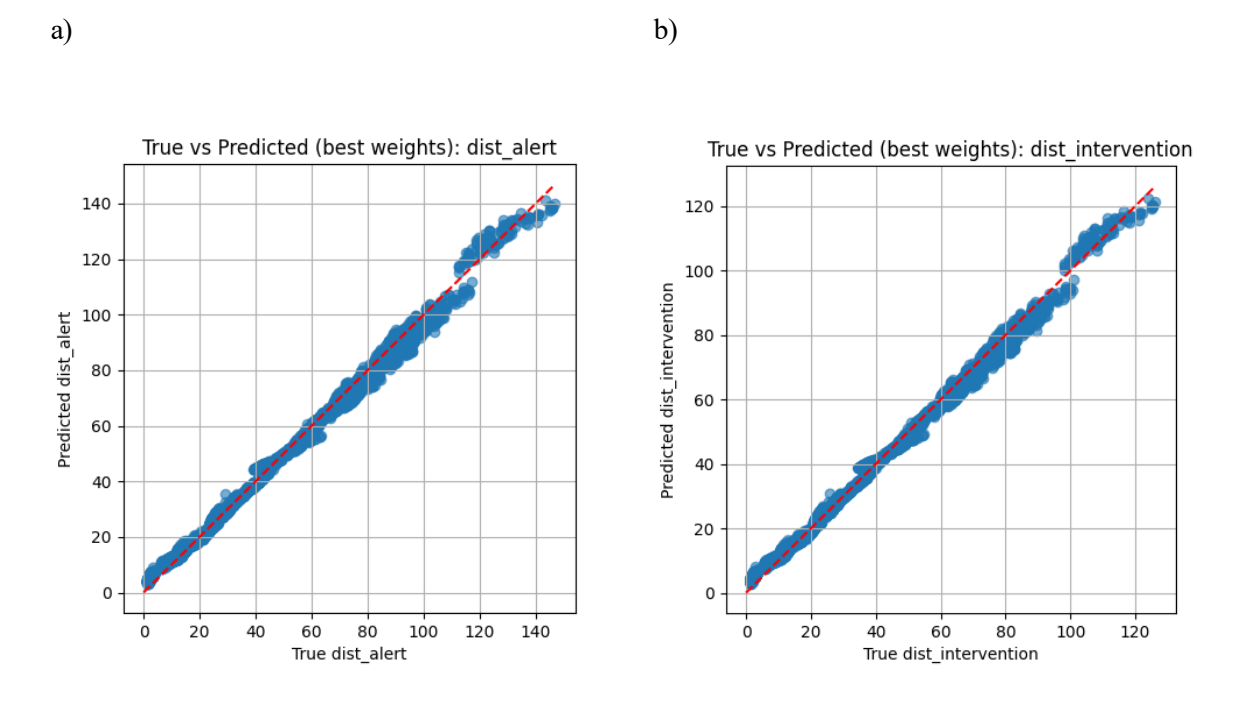


Figure 39. Scatter plots comparing the true values with the from the first version of NN model with: a) Release mass flow rate (kg/s); b) Flame length (m).



c)

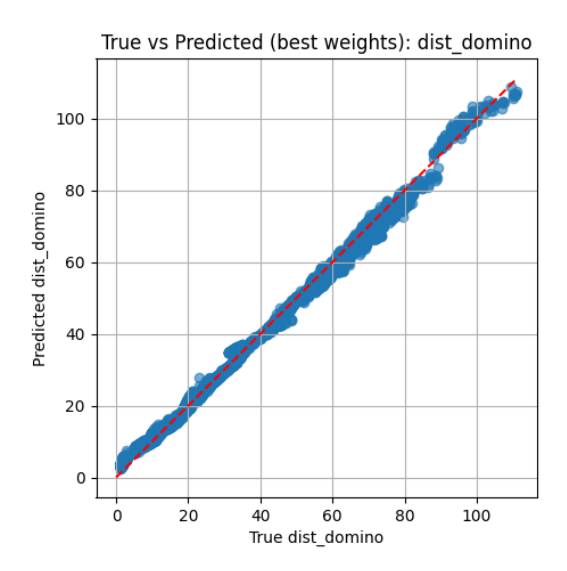


Figure 40. Scatter plots comparing the true values with the from the first version of NN model with: a) Distance (m) crosswind to an intensity level of 3 kW/m²; b) Distance (m) crosswind to an intensity level of 5 kW/m²; c) Distance (m) crosswind to an intensity level of 8 kW/m²

For the release mass flow rate, in Figure 39 (a), points near the middle (mass rates between 10 and 40 kg/s) lined up well, but at the upper extreme (mass rates 45–50 kg/s) the points laid below the ideal line, meaning underprediction. Looking at the right side for the flame lengths, Figure 39 (b), up to circa 60 m the points clustered closely around the diagonal Over this value, the tendency is a bit different but the point cloud is still around the diagonal. For the distances (Figure 40) points are slightly below the diagonal, indicating a tendency to underpredict the safety distances of 4 - 5 meters.

4.3 Optimization results of the MLFFNN with BP model

As explained in section 3.7, the baseline model used in section 4.2 was optimized considering the following variables: network geometry, activation functions, dropout rates, batch sizes in the validation section, learning rate with weight decay of the optimizer and patience in the early stopping.

In the sensitivity analysis the results of the valuative loss function were computed for each output parameter and used to choose the best available option. In these tables, MSE does not have the units, because it is obtained by the standardized features (input and output) used for training and validation.

According to the results shown in Tables 18, 19 and 20, the best configuration was:

- One input layer with 10 neurons.
- Two hidden layers with 128 and 64 neurons, respectively.
- An output layer of 5 neurons.
- Activation function: *LeakyReLU*.
- Dropout rate: 0%.
- Batch size in the validation section: 128.
- Adam optimizer with a learning rate 10⁻³ and a weight decay 0.
- 100 epochs with early stepping control on MSE of 10⁻⁶ and a patience value of 20.

Table 18. Sensitivity analysis performed on the model definition variables for the MLFNN with BP network used.

Number of neurons in (1st hidden layer, number 2nd hidden layer, etc.)	MSE
(16, 8)	0.0218
(32, 16)	0.0062
(64, 32)	0.0026
(128, 64)	0.0014
(48)	0.0034
(32, 16, 8)	0.0424
Activation function	MSE
ReLU	0.0021
LeakyReLU	0.0017
ELU	0.0033
tanh	0.0059
Dropout rate (%)	MSE
0	0.0001

10	0.0017
30	0.0033
50	0.0059

Table 19. Sensitivity analysis performed on the DataLoader for the MLFNN with BP network used.

Batch size	MSE
16	0.0001
32	0.0001
64	0.0001
128	0.0001

Table 20. Sensitivity analysis performed on the training loop for the MLFNN with BP network used.

Learning rate	Weight	decay	MSE
10-2	()	0
10-2	10) -5	0.0001
10-2	10) -4	0.0002
10-2	10) -3	0.001
10-3	()	0
10-3	10-5		0
10-3	10) -4	0.0001
10-3	10)-3	0.0007
10 ⁻⁴	()	0
10-4	10) -5	0
10 ⁻⁴	10		0
10 ⁻⁴	10)-3	0.0007
Early stopping patien		MSE	

5	0
10	0
20	0

The graphs in Figures 50 and 51 confirms that the most optimal configuration of MLFFNN with BP was obtained, because the majority of the points are on, or quite near, the ideal line.

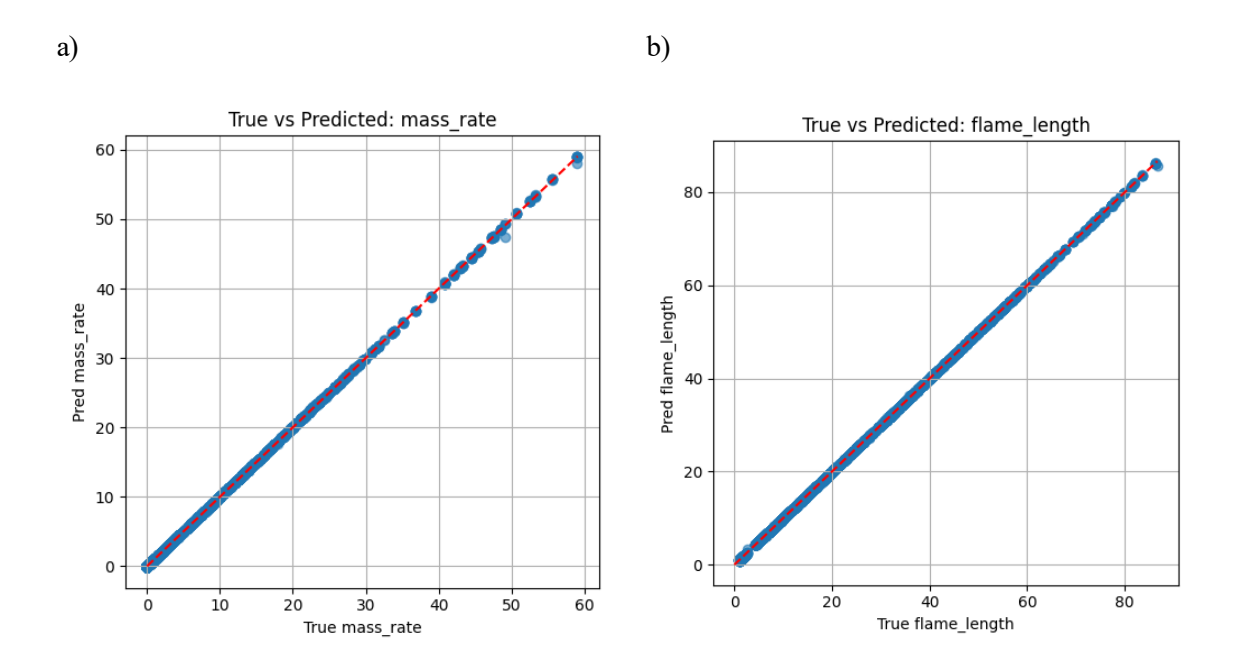


Figure 41. Scatter plots comparing the true values with the predicted ones from the optimized MLFFNN: a) Release mass flow rate (kg/s); b) Flame length (m).

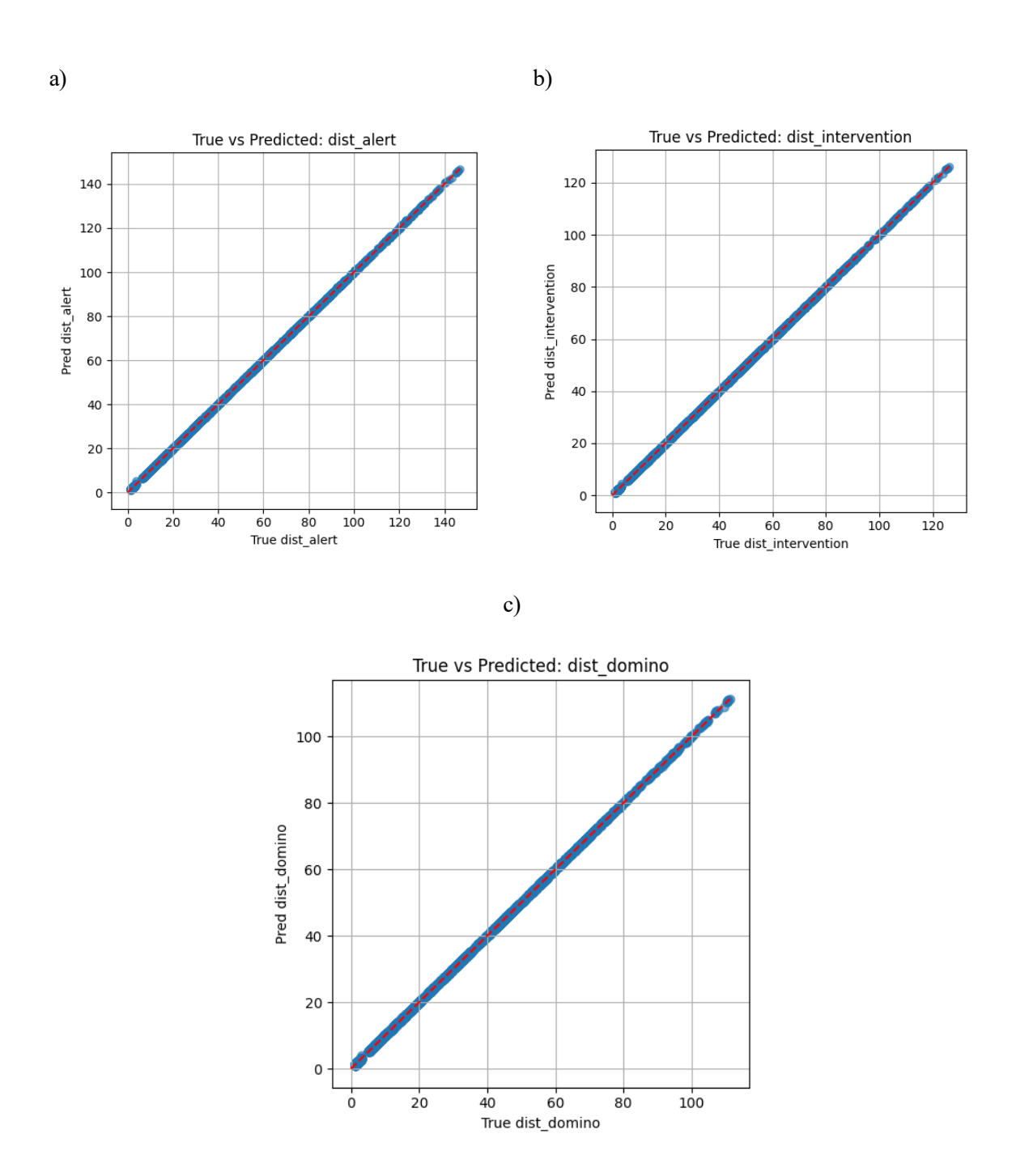


Figure 42. Scatter plots comparing the true values with the predicted ones from the optimized MLFFNN: a) Distance (m) crosswind to an intensity level of 3 kW/m²; b) Distance (m) crosswind to an intensity level of 5 kW/m².

4.4 Further works

Further work could focus on enhancing both the simulation and validation of HBNG jet fires, as well as improving the operability of the developed NN model.

First, it would be beneficial to explore more validated experiments and simulations of jet fires in PHAST not only focusing on horizontal leaks, where the Multi-Point Miller/DNV model was found to outperform Johnson's Cone model but also considering vertical flames with varying hydrogen concentrations. Additionally, expanding the storage pressure range to include values representative of the natural gas distribution grid would also be of interest.

A sensitivity analysis would be useful to understand how each input and configuration affects the model's results. For instance, it could reveal how individual weather parameters (e.g., wind speed, atmospheric stability, humidity, and solar radiation) influence flame behaviour.

Regarding the NN, other ML tools and architectures could be tested. For example Mashhadimoslem et al. (2023) used in their research not only MLFFNN for the evaluation of jet fires from the natural gas processing, storage and transport, but also a Radial Basis Function (RBF) network with only one hidden layer and several neurons.

It would also be useful to perform a sensitivity analysis on the neural network's hyperparameters not only to achieve a more targeted optimization, but also to better understand how each parameter influences the training process.

5 Conclusions

The promising opportunities that hydrogen could offer in terms of high energy density and net-zero emissions, lead to an exponential growth of studies in the production, transportation, and commercialization. Between the already analysed ways of transports, such as liquified and compressed gas forms, Hydrogen Blended Natural Gas has prospected as an economical and viable strategy. In particular, the H₂ produced is blended in the already exiting NG pipeline. However, this new mixture is affected by a different behaviour and problems than the normal natural gas, such as changing in the compressibility factor, energy transmission and temperature. In particular, due to the small dimension of H₂ and its high affinity with air, the common pipeline could be affected by hydrogen embrittlement phenomena, which is the cause of leaks and breaks in the structure. In addition, the small molecular size and low ignition energy of the added gas lead rapidly to turbulent jet flames. These high-momentum diffusion flames radiate heat impinge on nearby structures, and can trigger catastrophic domino events, and therefore HBNG jet fires represent a newest danger and safety issue in industrial risk-assessment workflows.

In parallel, new technological tools implementing machine learning offer faster and more accurate results than the common CFD software. Between the several algorithm, Neural Networks are optimal instruments, easily to modify and to implement. In particular, a MLFNN with Backpropagation, could be a simple, but at the same time efficient, structure to be created and use for simulating the jet mass flowrate, flame length and safety distances of the flames chosen to discuss.

In this thesis, before developing the indicated NN, were tested different configuration to simulate scenarios of horizontal HBNG jet fire from NG transmission pipeline, choosing as the most suitable the Pressure Vessel + Leak setup.

With this configuration a comprehensive database of 50,112 cases was generated in PHAST and collected in a Grid Consequence, by varying the volumetric concentration of H₂ blended (0 - 30 vol %), orifice diameter (1 - 50 mm), storage pressure (30 - 150 barg) and temperature (– 5, 15, 35 °C), as well as the meteorological condition (atmospheric stability, wind speed, ambient temperature and humidity).

These simulations revealed that increasing H₂ content, storage temperature, orifice diameter and reducing storage pressure each led, respectively, to lower mass release rates, shorter flame lengths and smaller required safety distances (3, 5 and 8 kW/m² contours).

Building on this database, a MLFFNN was trained using PyTorch, initially with two hidden layers (32 and 16 neurons) and ReLU activation function, achieving validation MSE $\approx 10^{-3}$ and $R^2 > 0.98$ across all outputs.

A subsequent optimization, increasing hidden layer sizes to 128 and 64 neurons respectively, switching to LeakyReLU, eliminating dropout, enlarging validation batches and tuning Adam's learning rate and weight decay, reduced the validation MSE to near zero and pushed R^2 to \geq 0.99 for jet mass flow, flame length and all three safety distance predictions.

Merging the full dataset from PHAST and the accuracy of the optimized NN, this one predicts mass release rates varying from 0.003 to 55.541 kg/s with an average absolute error below 0.58 kg/s, flame lengths spanning 0.94 to 83.96 m with mean deviations under 1.15 m, and crosswind safety distances for 3 kW/m² (Alert zone), 5 kW/m² (Intervention zone), and 8 kW/m² (Domino effect zone) ranging respectively from 1.374 to 138.75 m, 1.222 to 119.917 m, and 1.198 to 106.09 m with average errors of 1.45 m, 1.90 m, and 1.64 m

In the end, the developed model provides high accuracy estimates of jet fire consequences across the full parameter space, offering a practical, computationally efficient tool for rapid risk assessment in HBNG risk issues.

ANNEX A: Sustainability report

A.1 Environmental sustainability

The environmental impact of this work can be assessed by quantifying the main source of emissions, which is the electricity consumed during the research activities. Specifically, these emissions can be calculated based on the energy mix of Spain. Figure 43 illustrates the daily distribution of electricity production sources, with wind, photovoltaic, and nuclear energy being the three primary sources, as indicated by the Electricity Map. This tool also provides data on the average mass of equivalent CO₂ emissions per kWh consumed during each hour of the day Table 21. Carbon dioxide equivalent, as defined from the European Environment Agency, is a measure used to compare the emissions from various greenhouse gases based upon their global warming potential (GWP).

To estimate the amount of equivalent CO₂ emitted during the development of this master thesis, a standard electricity consumption value for a computer was used. On average, most of the computers use between 0.8 and 2.5 kWh per hour. The activities primarily took place in the morning, from 9 am to 1 pm. Considering five hours per day and 100 days as extent of the thesis work, the total amount of equivalent CO₂ emitted resulted to be between 3.8 and 11.9 kg CO_{2eq}.

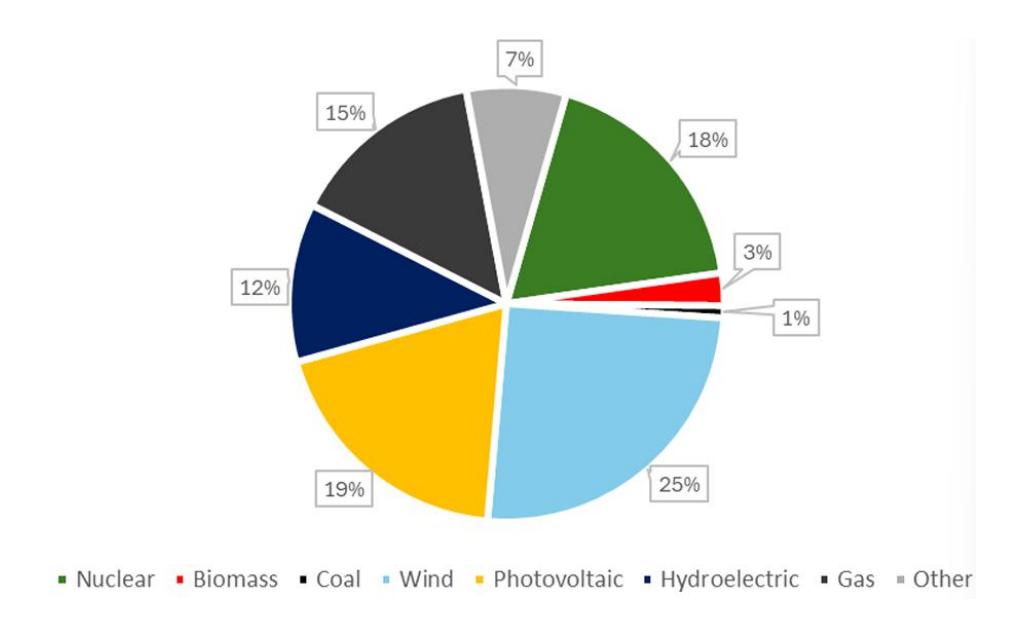


Figure 43. Energy mix of Spain (EMBER 2024.)

Table 21. Equivalent CO₂ emission per kWh during the morning hours.

Hour	Emissions (g CO _{2eq} /kWh)
From 9 a.m. to 10 a.m.	140
From 19 a.m. to 11 a.m.	129
From 11 a.m. to 12 a.m.	109
From 12 a.m. to 1 p.m.	97

Additional sources of emissions that should be considered include the energy required to power and cool the data centre systems that host the servers supporting the software. The use of the internet itself, involving the transmission and reception of data, also relies on communication networks, which have their own environmental impact. These elements, however, are difficult to estimate numerically without precise data from the software providers.

A.2 Economic sustainability

Quantifying the costs associated with the thesis work involves considering both human and material resources. Regarding material resources, the software tool utilized plays a significant role. Indeed, PHAST is a commercial software that requires a license, resulting in a financial expense.

In terms of human resources, the costs encompass the personnel involved in the project, including the student's own time spent on research, writing and analysis, as well as any expenses related to supervision or tutoring provided by academic supervisors. Estimating the number of hours contributed by each person involved is crucial for accurate cost assessment. For example, the student's personal involvement in the project averaged four hours per day, resulting in a total of 420 hours.

Additional material resources include the use of computer hardware, office supplies and other equipment necessary for simulations and data analysis. Indirect costs, such as electricity consumption for running the software and hardware, internet usage and other utilities, should be also considered.

A.3 Ethical implications

This thesis work responds to the growing need for safe and efficient H₂ transportation and usage, particularly in the context of the global shift towards sustainable energy solutions. Specifically, it addresses the needs of enhancing safety by identifying and calculating in a faster way the safety distances in case of an accidental jet fire scenario, improving efficiency of industrial processes and contributing to sustainability by advancing clean energy technologies.

This work adheres to the ethical standards and deontological codes relevant to engineering and scientific research. This involves accurately reporting and honestly interpreting all data and findings. Additionally, the work is committed to practices that support long-term environmental sustainability. Transparency is ensured in the methodologies employed, ensuring that all procedures utilized throughout the thesis work are explicitly described and documented, allowing others to comprehend and evaluate the work undertaken.

A.4 Relationship with the Sustainable Development Goals

The Sustainable Development Goals (SDGs), also known as the Global Goals, were adopted by the United Nations in 2015. United Nations aim to achieve 17 goals by 2030, addressing the global challenges we face, including those related to poverty, inequality, climate change, environmental degradation, peace and justice.

This thesis work contributes in part to the Sustainable Development Goals (SDGs) illustrated in Figure 44. Hydrogen, as previously mentioned, is a clean fuel because its combustion does not emit GHGs. When produced through sustainable methods (Green H₂), it serves as a source of clean energy. By analysing potential cases of horizontal HBNG jet fires from transmission pipelines and developing a predictive tool (MLFFNN) for assessing their consequences, this

research contributes to innovation in industrial processes and improvements in urban safety. Notably, it aligns with Goal 11 of the Sustainable Development Goals, which includes the objective of providing access to safe and sustainable transport systems.











Figure 44. SDGs related to the thesis work.

ANNEX B: PHAST models

B.1 Source models for pressure vessel leaks

The DISC model implemented in PHAST - DNV (DNV 2023) is a suite of instantaneous and continuous discharge models for hazardous chemicals stored in vessels. Following a leak in a vessel or in a pipe attached to a vessel, a discharge will occur to the atmosphere. In particular, the Orifice model is a conservative and initial-rate discharge model which predicts the worst-case initial discharge rate and the duration associated with this discharge rate. The chemical stored in the vessel may be vapour, liquid or two-phase. The model is illustrated in Figure 45 and describes the expansion from pre-release conditions to the orifice. The pre-release or initial conditions are determined from the user-specified storage conditions according to the scenario and other settings. Expansion from the orifice to atmospheric conditions is managed by the Atmospheric Expansion theory (ATEX) model (DNV 2023).

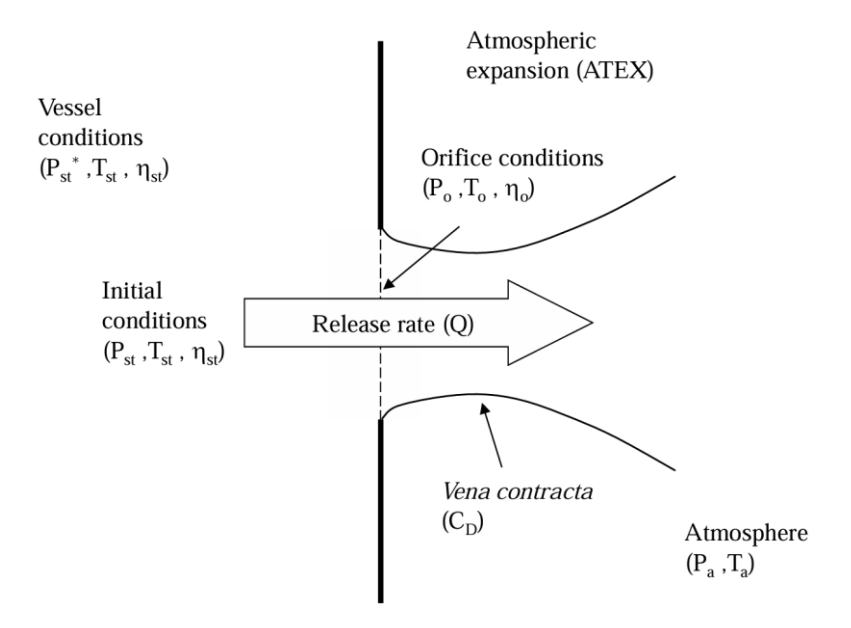


Figure 45. Orifice and atmospheric expansion conditions (DNV 2023).

The following equations are used to determine the orifice conditions. By conservation of energy, assuming initially the material is stagnant:

$$h(P_{st}, T_{st}, \eta_{st}) = h(P_o, T_o, \eta_o) + \frac{u_o^2}{2}$$
 (20)

Where: h stands for enthalpy (on the left side it is dependent on storage P_{st} , storage temperature T_{st} and mass liquid fraction η_{st} ; on the right side it is dependent on orifice P_o , orifice temperature T_o and orifice mass liquid fraction η_o), u_o is the orifice velocity.

By conservation of entropy s:

$$s(P_{st}, T_{st}, \eta_{st}) = s(P_o, T_o, \eta_o)$$
(21)

Note that during this isentropic expansion to the orifice, materials which are initially pure vapour or liquid can be forced to remain so by setting the model input 'Phase change upstream of orifice'. The default setting is 'Disallow liquid phase change', also referred to as the 'metastable liquid' approach. The assumption is that there is insufficient time for changes in phase before the material reaches the orifice.

The orifice pressure P_o equals the ambient pressure in case of unchoked flow, and is determined from the choke pressure in case of choked flow:

$$P_o = MAX(P_a, P_c) (22)$$

Where: P_a is the atmospheric pressure and P_c is the choke pressure at the orifice and is defined as the pressure at which the mass flux G_o through the orifice is maximized:

$$G_o = \frac{u_o}{v_o} \tag{23}$$

The specific volume v_o is calculated as:

$$v_o = \frac{\eta_o}{\rho_{Lo}} + \frac{(1 - \eta_o)}{\rho_{Vo}} \tag{24}$$

The mass release rate Q^* is then:

$$Q^* = A_0 G_0 \tag{25}$$

Where A_o is the orifice area.

This represents an idealized flow rate, but the frictional effect of convergent flow at the orifice (as represented by the vena contracta in Figure 45 effectively reduces this. The convention is to

achieve this by reducing orifice cross-sectional area $(A_v < A_o)$. The ratio of this reduction is the discharge coefficient C_D :

$$A_{\nu} = C_D A_0 \tag{26}$$

$$Q = A_v G_0 \tag{27}$$

The method used to calculate the discharge coefficient C_D is calculated as the ratio of the actual mass flow to that which could be passed through the full area of the orifice, with values in the range between 0.6 to 1. Finally, the release duration t_{rel} can be obtained as:

$$t_{rel} = \frac{M_{st}}{O} \tag{28}$$

For fixed duration runs (i.e. where the user input fixed duration > 0 in PHAST) orifice diameter is allowed to vary such that the release rate is sufficient to discharge the inventory in the specified time. As orifice state and mass flux are independent of orifice diameter, we may calculate G_o and C_D as described above, then use Equation (27) to determine release rate Q, and Equation (26) to determine vena contracta diameter.

B.1.1 Method of solution

The sequence of steps used to determine the orifice conditions is:

1. For a given P_o , temperature and liquid fraction are determined from the isentropic-expansion Equation (23). In terms of vapour (s_V) and liquid (s_L) entropies, the total entropy is:

$$s = \eta_L s_L(P, T) + (1 - \eta_L) s_V(P, T)$$
(29)

The leak scenario force vapour or liquid discharges to remain the same phase after expansion, in which cases the liquid fraction is set to one or zero. As liquid entropy is less than vapour entropy, whether the final state in single-phase can be determined from Equation (29):

$$s > s_V(P, T) \tag{30}$$

With $\eta_L = 0$ for vapor case.

2. Calculate orifice velocity from conservation-of-energy Equation(20).

- 3. Calculate the mass flux from Equation (25).
- 4. The orifice pressure is iterated until the mass flux is maximized, and P_o set according to Equation (22).
- 5. Calculate C_D and modified Q and A_V from Equation (26).
- 6. Calculate release duration from Equation (28).

B.2 Calculation of still air flame length parameters for non-hydrocarbons

The M-MPS model employs the *Kalghatgi*'s correlation derived from experiments on the vertical flames in still air to determine the still air flame length L_{B0} for non-hydrocarbon flames.

$$\left(\frac{D_s \beta}{L_{B0} W_{st}}\right)^{\frac{2}{3}} = 0.2 + 0.024 \xi(L_{B0})$$
(31)

Where: β Becker and Liang's flame constant, W_{st} mass fraction of fuel in a stoichiometric mixture with air, D_s combustion or effective source diameter, ξ Richardson number.

The mass fraction of fuel in a stoichiometric mixture with air, W_{st} can be calculated as:

$$W_{st} = \frac{M_w C_t}{M_w C_t + (1 - C_t) W_{air}}$$
 (32)

Where:

$$C_t = \frac{mole\ of\ fuel}{mole\ of\ fuel + moles\ of\ air} \tag{33}$$

$$A_{t} = \frac{mole\ of\ fuel + moles\ of\ air}{mole\ of\ combustion\ products} \tag{34}$$

For the adiabatic combustion temperature T_1 (K) Miller presented the following correlations for estimating adiabatic combustion temperature for mixtures containing flammable and inert gases:

$$T_1 = T_{1,fuel}(-0.7395CD_{equiv}^2 + 0.0366CD_{equiv} + 0.9972)$$
 (35)

$$T_{1,fuel} = 321.08H_{2\,equiv}^3 - 310.88H_{2\,equiv}^2 + 144.03H_{2\,equiv} + 2223$$
 (36)

$$CD_{equiv} = x_{CD} + 0.84x_{WA} + 0.59x_{N2}$$
 (37)

$$H_{2 equiv} = \frac{x_{H2 equiv}}{x_{H2 equiv} + x_{C1 equiv}}$$
(38)

$$x_{H2equiv} = x_{H2} + x_{CM} \tag{39}$$

$$x_{C1equiv} = x_{C1} + x_{C2} + x_{C3} + x_{C4} + x_{C.} (40)$$

Where: $T_{1,fuel}$ adiabatic combustion temperature for combustible materials (K), x_{CD} , x_{WA} , x_{N2} mole fractions of carbon dioxide, water vapor and nitrogen in the fuel mixture (respectively), $x_{H2equiv}$ sum of mole fractions of flammable non-hydrocarbons, $x_{C1equiv}$ sum of mole fractions of flammable hydrocarbons, x_{H2} , x_{CM} mole fractions of H₂ and carbon monoxide (respectively), x_{C1} , x_{C2} , x_{C3} , x_{C4} , $x_{C.}$ mole fractions of hydrocarbons.

B.3 Calculation of flame momentum and lift-off distances

The "frustum lift off", B_M , is defined as the distance along the hole axis from the hole to the point of intersection of the cone axis. For releases inclined vertically or at 45° to the horizontal, the momentum dominated flame length B_M for horizontal release is calculated from:

$$\frac{B_M}{L_{R0}} = MAX(0, MIN(e^{-0.13N_{Richardson}L_{B0}}, 1)$$
 (41)

Originally, the Miller model assumes jet flames to burn very close to the source with zero flame lift-off distance (B). This assumption is somewhat tenable for H_2 , given its high laminar burning velocity, wide flammability limits, hence, propensity to burn (high combustion reactivity/potential). For less reactive materials, e.g., hydrocarbons, field/experimental evidence on jet flames, suggest a finite (flame lift-off) distance exists between the release source and onset of visible combustion.

As such, the M-MPS model has been extended to support the modelling of a finite flame lift-off distance (*B*) given by:

$$B = 0.2B_M \tag{42}$$

B.4 Calculation of radiant heat fraction and radiation characteristics

Miller recommends the following correlation for determining the total heat radiating from the flame along the flame centrelines (Q_{rad}) :

$$Q_{rad} = F_{AP} m H_{COMB} (43)$$

Where F_{AP} is the flame radiant heat fraction along the flame centerline:

$$F_{AP} = MAX\{(x_{C1equiv}F_s + x_{H2equiv}F_{H2}), 0.05\}$$
(44)

 F_s and F_{H2} are given by:

$$F_s = 0.21e^{-0.00323v_j} + 0.11 (45)$$

$$F_{H2} = F_{corr}(0.1691 - 0.01ln(M_{flux}))$$
 (46)

Where for horizontal jet fire:

$$M_{flux} = \frac{4m}{pd_0^2} \tag{47}$$

$$F_{corr} = 1.36 + 0.076MIN\{10, L_f/h_{RC}\}$$
 (48)

$$h_{RC} = z_{Elev} + MAX(0, (0.66L_f - B_M) \sin(\alpha_{AP}))$$
(49)

The radiated heat is assumed to be generated from point sources evenly distributed along the flame centreline L_f . The amount of heat from each point source is linearly weighted with minimum values at each end and a maximum at the radiant centre of the flame, 2/3 along L_f .

ANNEX C: Grid consequences from PHAST HBNG jet fire simulations

The following table is one of the three "grid consequences" excel create using the simulator programme PHAST with input configuration Pressure Vessel + Leak in Miller model, for the simulation of a third of the 50,112 cases set by the parameter in Tables 12, 13 and 14. Indeed the storage temperature of the jet fire gases was -5 °C here, but were created the relative excel for 15 °C and 35 °C.

An approach to read the table could be the following:

- 1. Setting the material (gas mixture): CH₄, 5, 10, 20, 24, 30 %vol.
- 2. Fixing a pressure storage: 30, 45, 50, 60, 70, 80, 100, 150 barg.
- 3. Fixing each orifice diameter: 1, 5, 10, 20, 35, 50 mm.
- 4. Trying each one of the different weather conditions: Table 13 and Table 16.
- 5. Changing the pressure of storage and repeat point 3 and 4.
- 6. Repeat from point 2 to 5 for each composition.

For reasons of space, it was not possible to include all the 16,704 different cases and their results in Table 22 so only some of them are tabulated to let understand their disposition.

Table 22. Selected values of the Jet fire sheet from the grid consequence of a simulated Pressure Vessel + Leak with Miller/DNV model setup for HBNG horizontal jet fire cases with the input parameter in section 3.4.2.

Path	Scenario	Weather	Hole size (mm)	Material	Temper ature (input) (degC)	Pressure (input) (bar)	Height of interest (comin g from parame ters) (m)	Jet fire mass rate (kg/s)	Fla me lengt h (m)	Jet fire radiat ion intens ity level 1	Distan ce down wind to intensi ty level 1 (5 kW/m 2) (m)	Distan ce down wind to intensi ty level 2 (3 kW/m 2) (m)	Distan ce down wind to intensi ty level 3 (8 kW/m 2) (m)
Study1\Pressu re_vessel_ME THANE_30	Leak_30 _1	Lowesmi th_2012	1	METHAN E	-5	30	3,25	0.0039 8631	1,09 947	Param eter value	1.4171	1.5897 9	1.3468 9
Study1\Pressu re_vessel_ME THANE_30	Leak_30 _1	A-1 5_50	1	METHAN E	-5	30	3,25	0.0039 8631	1,09 624	Param eter value	1.4154 5	1.5905 1	1.3441 9
Study1\Pressu re_vessel_ME THANE_30	Leak_30 _50	Lowesmi th_2012	50	METHAN E	-5	30	3,25	9.9657 8	38,4 636	Param eter value	54.065 5	62.110 4	48.250 6
Study1\Pressu re_vessel_ME THANE_30	Leak_30 _50	A-1 5_50	50	METHAN E	-5	30	3,25	9.9657 8	38,2 978	Param eter value	54.820 7	63.206 7	48.773 8
Study1\Pressu re_vessel_ME THANE_45	Leak_45 _1	Lowesmi th_2012	1	METHAN E	-5	45	3,25	0.0060 6752	1,33 731	Param eter value	1.7324 3	1.9450 2	1.5805 1
Study1\Pressu re_vessel_ME THANE_45	Leak_45 _1	A-1 5_50	1	METHAN E	-5	45	3,25	0.0060 6752	1,33 359	Param eter value	1.7320 4	1.9492 4	1.5782 5
Study1\Pressu re_vessel_ME THANE_150	Leak_15 0_50	F-3 5_70	50	METHAN E	-5	150	3,25	58.975 3	86,2 619	Param eter value	125.54	145.91 4	110.66 4
Study1\Pressu re_vessel_ME THANE_150	Leak_15 0_50	F-3 5_90	50	METHAN E	-5	150	3,25	58.975 3	86,2 732	Param eter value	124.98 2	145.14 9	110.23 9
Study1\Pressu re_vessel_5_3 0	Leak_30 _1	Lowesmi th_2012	1	MIXTURE _5	-5	30	3,25	0.0038 8104	1,08 339	Param eter value	1.3952 9	1.5649 4	1.3313 5
Study1\Pressu re_vessel_5_3 0	Leak_30 _1	A-1 5_50	1	MIXTURE _5	-5	30	3,25	0.0038 8104	1,08 023	Param eter value	1.3936	1.5654 8	1.3287 7
Study1\Pressu re_vessel_30_ 150	Leak_15 0_50	F-3 5_70	50	MIXTURE _30	-5	150	3,25	43.299 6	73,7 71	Param eter value	108.58	125.80	96.092
Study1\Pressu re_vessel_30_ 150	Leak_15 0_50	F-3 5_90	50	MIXTURE _30	-5	150	3,25	43.299 6	73,7 808	Param eter value	108.12 7	125.18	95.753 2

ANNEX D: Results of the simulation in PHAST changing the storage temperature

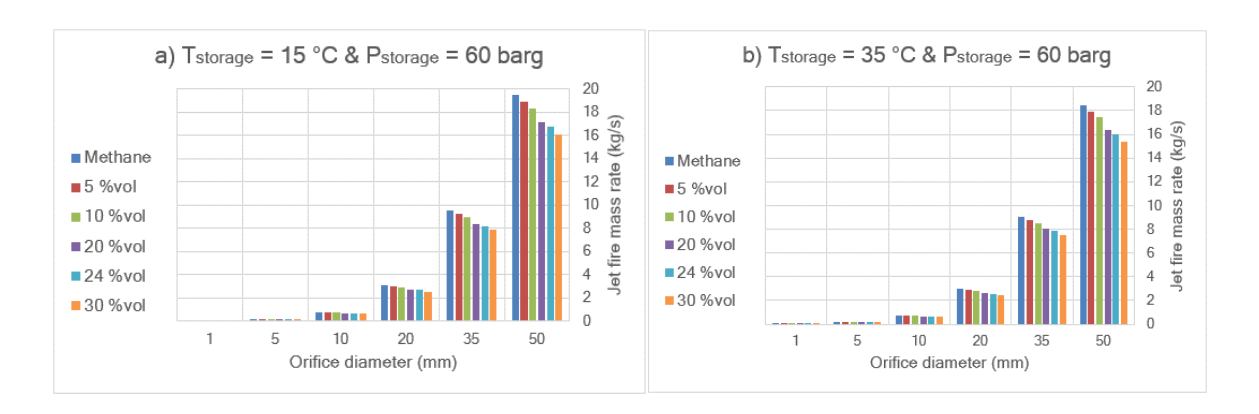


Figure 46. Jet fire mass rate (kg/s) from the grid consequence results of PHAST simulation of a setup jet fire with storage pressure 60 barg and storage temperature 15 °C (a) and 35 °C (b) at different orifice diameter (10, 20, 35, 50 mm) and different H₂ blended compositions (0, 5, 10, 20, 35, 50 %).

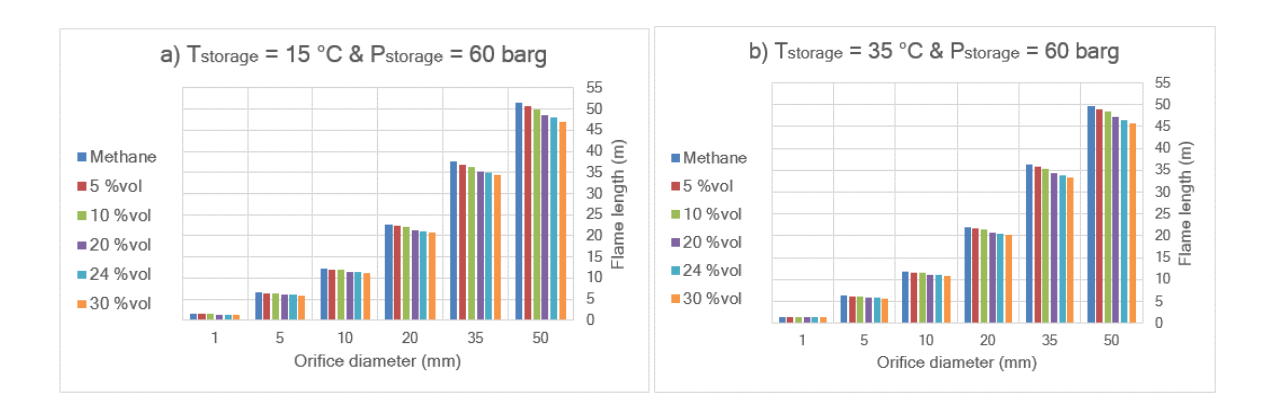


Figure 47. Flame length (m) from the grid consequence results of PHAST simulation of a setup jet fire with storage pressure 60 barg and storage temperature 15°C (a) and 35°C (b) at different orifice diameter (10, 20, 35, 50 mm) and different H₂ blended compositions (0, 5, 10, 20, 35, 50 %).

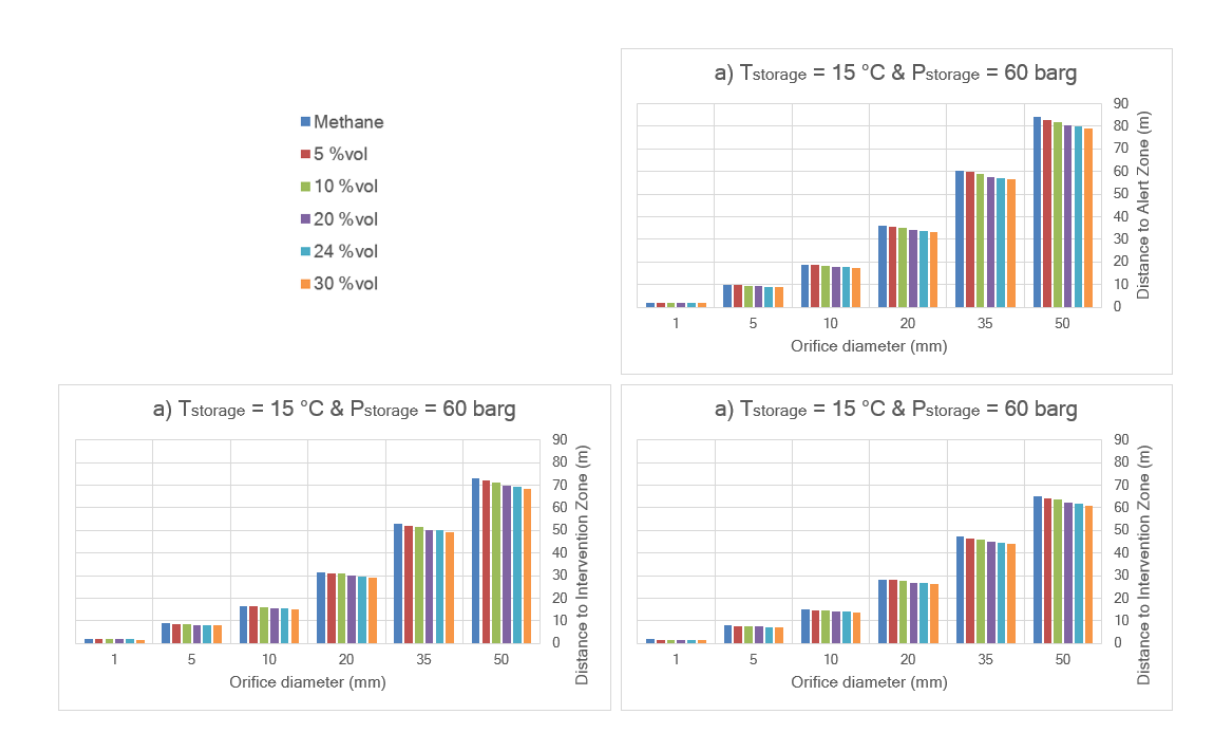


Figure 48. Distance crosswind to intensity level 3, 5, 8 kW/m² from the grid consequence results of PHAST simulation of a setup jet fire with storage pressure 60 barg and storage temperature 15°C at different orifice diameter (10, 20, 35, 50 mm) and different H₂ blended compositions (0, 5, 10, 20, 35, 50 %).

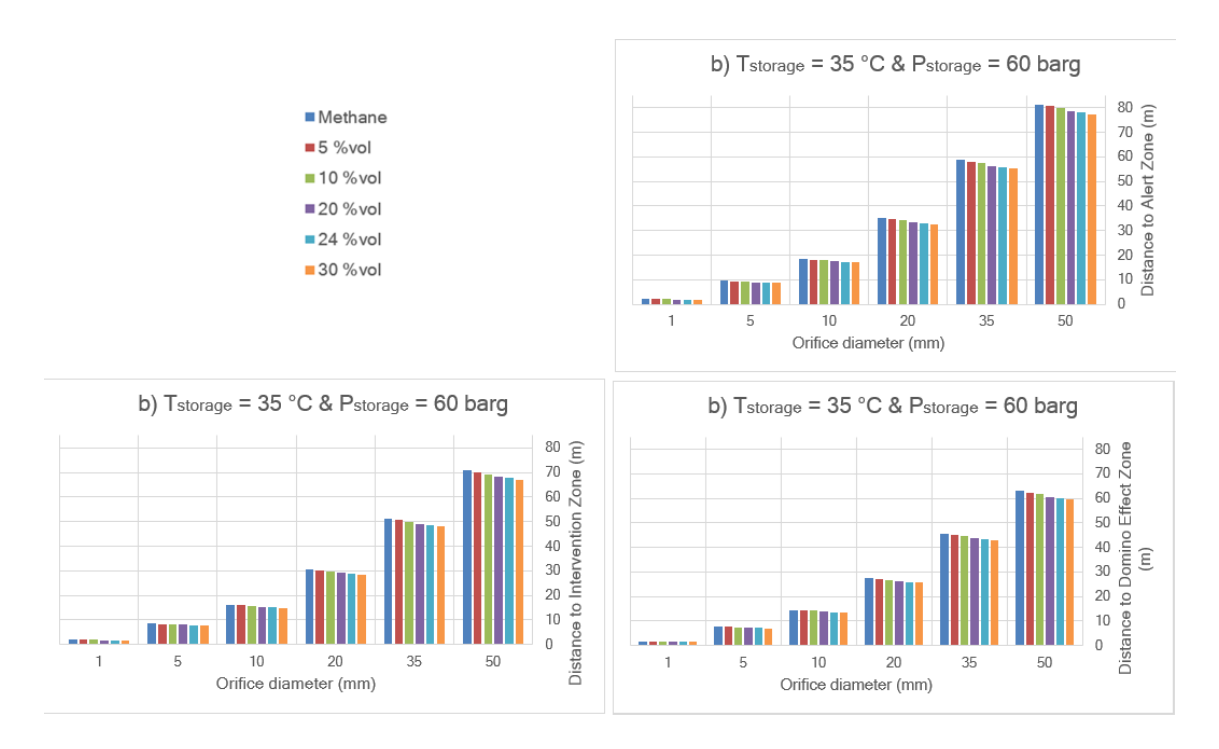


Figure 49. Distance crosswind to intensity level 3, 5, 8 kW/m² from the grid consequence results of PHAST simulation of a setup jet fire with storage pressure 60 barg and storage temperature 35°C at different orifice diameter (10, 20, 35, 50 mm) and different H₂ blended compositions (0, 5, 10, 20, 35, 50 %).

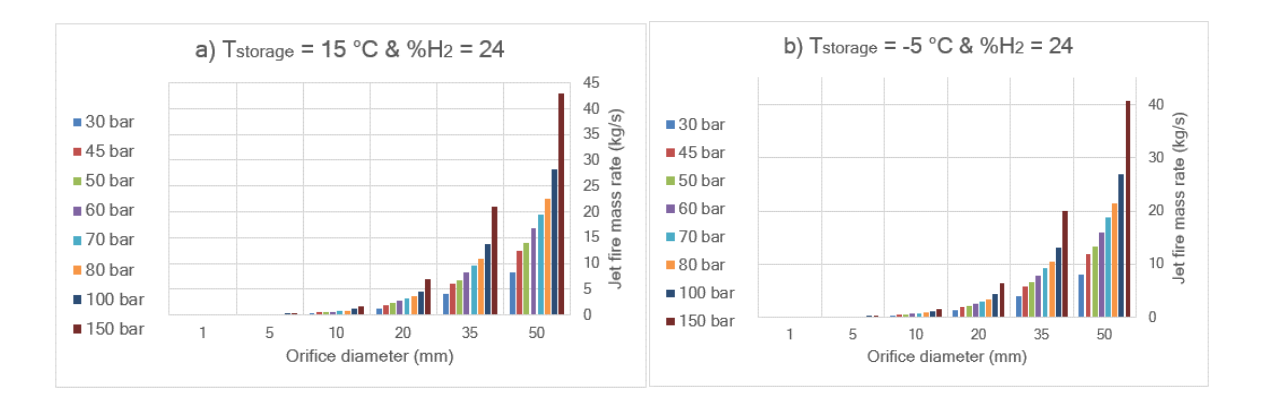


Figure 50. Jet fire mass rate (kg/s) from the grid consequence results of PHAST simulation of a setup jet fire with hydrogen blended compositions 24 %vol and storage temperature 15°C (a) and 35°C (b) at different orifice diameter (10, 20, 35, 50 mm) and different storage pressure (30, 45, 50, 60, 70, 80, 100, 150 barg).

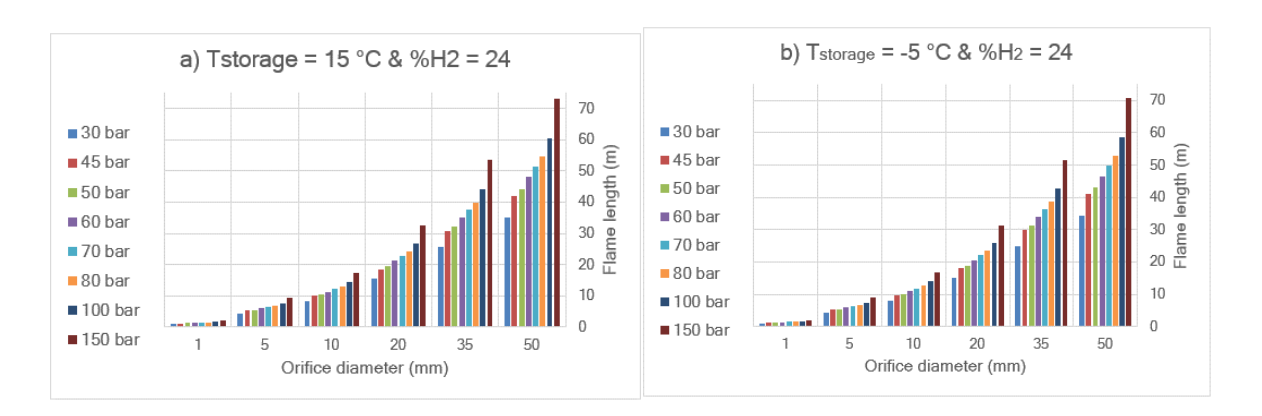


Figure 51. Flame length (m) from the grid consequence results of PHAST simulation of a setup jet fire with H₂ blended compositions 24 %vol and storage temperature 15°C (a) and 35°C (b) at different orifice diameter (10, 20, 35, 50 mm) and different storage pressure (30, 45, 50, 60, 70, 80, 100, 150 barg).

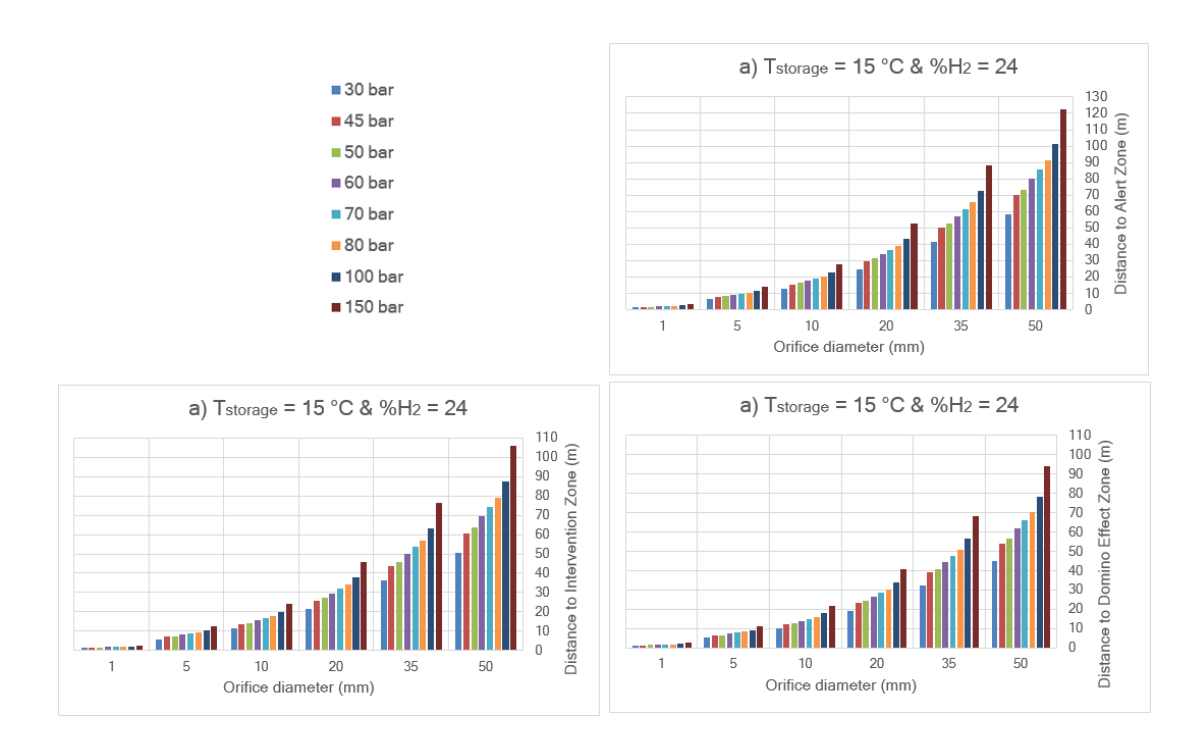


Figure 52. Distance crosswind to intensity level 3, 5, 8 kW/m² from the grid consequence results of PHAST simulation of a setup jet fire with H₂ blended compositions 24 %vol and storage temperature 15 °C at different orifice diameter (10, 20, 35, 50 mm) and different storage pressure (30, 45, 50, 60, 70, 80, 100, 150 barg).

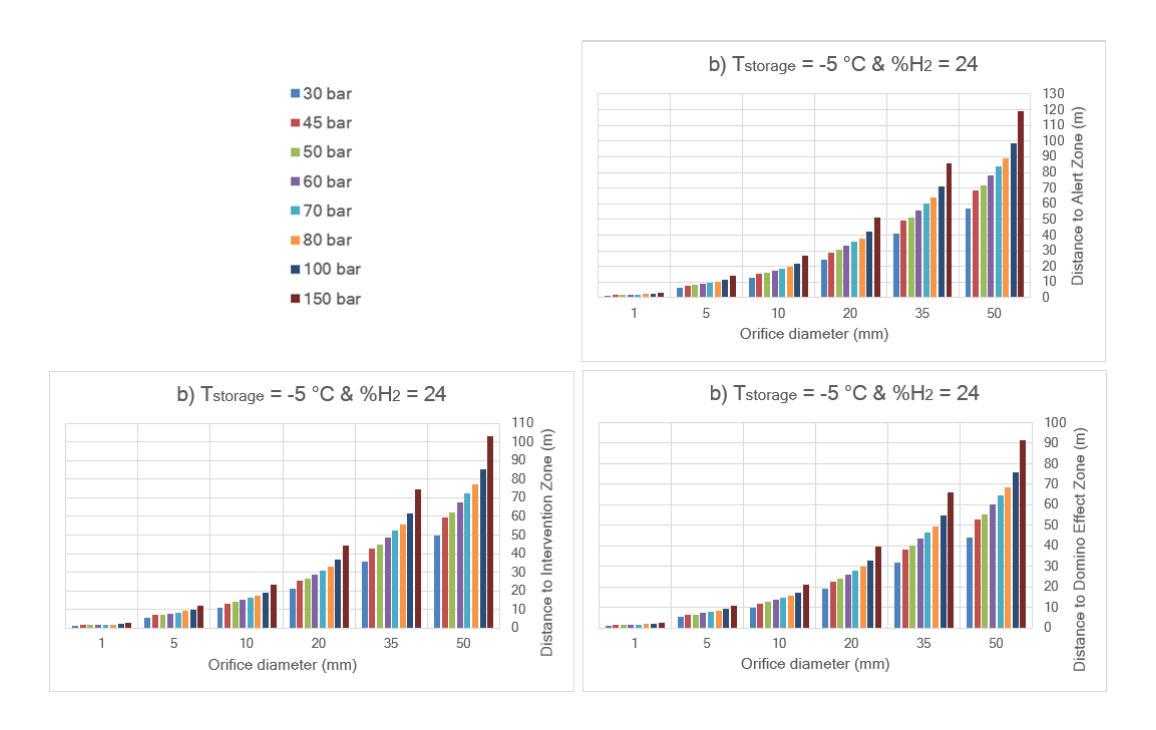


Figure 53. Distance crosswind to intensity level 3, 5, 8 kW/m² from the grid consequence results of PHAST simulation of a setup jet fire with H₂ blended compositions 24 %vol and storage temperature 35 °C at different orifice diameter (10, 20, 35, 50 mm) and different storage pressure (30, 45, 50, 60, 70, 80, 100, 150 barg).

References

AlHumaidan, Faisal S., Mamun Absi Halabi, Mohan S. Rana, and Mari Vinoba. 2023. 'Blue Hydrogen: Current Status and Future Technologies'. *Energy Conversion and Management* 283 (May):116840. https://doi.org/10.1016/j.enconman.2023.116840.

ATCO. 'Clean Energy Innovation Hub Lessions'. Accessed 5 June 2025 https://gas.atco.com/en-au/natural-gas/future-gas/clean-energy-innovation-hub-virtual-tour/clean-energy-innovation-hub.html.

Aziz, Muhammad, Agung Tri Wijayanta, and Asep Bayu Dani Nandiyanto. 2020. 'Ammonia as Effective Hydrogen Storage: A Review on Production, Storage and Utilization'. *Energies* 13 (12): 3062. https://doi.org/10.3390/en13123062.

Bickhard, Mark H. 1993. 'Representational Content in Humans and Machines'. *Journal of Experimental & Theoretical Artificial Intelligence* 5 (4): 285–333. https://doi.org/10.1080/09528139308953775.

Buffi, Marco, Matteo Prussi, and Nicolae Scarlat. 2022. 'Energy and Environmental Assessment of Hydrogen from Biomass Sources: Challenges and Perspectives'. *Biomass and Bioenergy* 165 (October):106556. https://doi.org/10.1016/j.biombioe.2022.106556.

Carvalho, Rui, Lubos Buzna, Flavio Bono, Eugenio Gutiérrez, Wolfram Just, and David Arrowsmith. 2009. 'Robustness of Trans-European Gas Networks'. *Physical Review E* 80 (1): 016106. https://doi.org/10.1103/PhysRevE.80.016106.

Casal, Joaquim. 2018a. 'Chapter 3 - Fire Accidents'. In *Evaluation of the Effects and Consequences of Major Accidents in Industrial Plants (Second Edition)*, edited by Joaquim Casal, 75–150. Elsevier. https://doi.org/10.1016/B978-0-444-63883-0.00003-4.

Casal, Joaquim. 2018b. 'Chapter 10 - Domino Effect'. In *Evaluation of the Effects and Consequences of Major Accidents in Industrial Plants (Second Edition)*, edited by Joaquim Casal, 405–37. Elsevier. https://doi.org/10.1016/B978-0-444-63883-0.00010-1.

Casal, Joaquim 2008. 'Evaluation of the Effects and Consequences of Major Accidents in Industrial Plants (Industrial Safety Series, 8), J., Elsevier B.V., Oxford, UK/Boston, MA (2008), 378pp.. *Journal of Loss Prevention in the Process Industries* 21 (4): 490–91. https://doi.org/10.1016/j.jlp.2008.01.001.

Chae, Min Ju, Ju Hyun Kim, Bryan Moon, Simon Park, and Young Soo Lee. 2022. 'The Present Condition and Outlook for Hydrogen-Natural Gas Blending Technology'. *Korean Journal of Chemical Engineering* 39 (2): 251–62. https://doi.org/10.1007/s11814-021-0960-8.

Choudhuri, A. 2000. 'Combustion Characteristics of Hydrogen–Hydrocarbon Hybrid Fuels'. *International Journal of Hydrogen Energy* 25 (5): 451–62. https://doi.org/10.1016/S0360-3199(99)00027-0.

Choudhuri, Ahsan R, and S R Gollahalli. n.d. 'Characteristics of Hydrogen–Hydrocarbon Composite Fuel Turbulent Jet flames'. https://doi.org/10.1016/S0140-6701(03)81872-6.

Cristello, Josmar B., Jaehyun M. Yang, Ron Hugo, Youngsoo Lee, and Simon S. Park. 2023. 'Feasibility Analysis of Blending Hydrogen into Natural Gas Networks'. *International Journal of Hydrogen Energy* 48 (46): 17605–29. https://doi.org/10.1016/j.ijhydene.2023.01.156.

Delvosalle, C.. 1996. 'Domino Effects Phenomena: Definition, Overview and Classification'. *European Seminar on Domino Effects, Leuven, Belgium, 1996.* https://cir.nii.ac.jp/crid/1573668925169070592.

Directorate General for Climate Action (European Commission). 2019. *Going Climate-Neutral by 2050:* A Strategic Long Term Vision for a Prosperous, Modern, Competitive and Climate Neutral EU Economy. Publications Office of the European Union. https://data.europa.eu/doi/10.2834/02074.

DNV. 2023. 'DISC Model Theory.Pdf'. Accessed 5 June 2025. https://mysoftware.dnv.com/download/public/phast/technical_documentation/03_discharge/DISC%20 Model%20Theory.pdf.

DNV. 2023. 'JFSH Jet Fire Model Theory.Pdf'. Accessed 5 June 2025. https://mysoftware.dnv.com/download/public/phast/technical_documentation/07_fire_models/JFSH% 20Jet%20Fire%20Model%20Theory.pdf.

DNV. 2023. 'JFSH Jet Fire Model Validation.Pdf'. n.d. Accessed 5 June 2025 https://mysoftware.dnv.com/download/public/phast/technical_documentation/07_fire_models/JFSH% 20Jet%20Fire%20Model%20Validation.pdf.

DNV. 'Consequence Analysis with Phast'. Accessed 5 June 2025. https://www.dnv.com/software/services/plant/consequence-analysis-phast/.

DNV. 'Phast Multi-Component Extension - Atmospheric Dispersion Modelling Software'. Accessed 9 June 2025. https://www.dnv.com/software/services/plant/phast-safeti-multi-component-add-on/.

Eia. 2021 'AEO_Narrative_2021.Pdf'. Accessed 5 June 2025. https://www.eia.gov/outlooks/aeo/pdf/AEO_Narrative_2021.pdf 'AHC-Hydrogen-Park-South-Australia-Public-Knowledge-Sharing-Report'. n.d.

El-Ghafour, S.A.A., A.H.E. El-dein, and A.A.R. Aref. 2010. 'Combustion Characteristics of Natural Gas—Hydrogen Hybrid Fuel Turbulent Diffusion Flame'. *International Journal of Hydrogen Energy* 35 (6): 2556–65. https://doi.org/10.1016/j.ijhydene.2009.12.049.

ENTSOG. 2015. 'The European Natural Gas Network' https://www.entsog.eu/sites/default/files/2018-10/ENTSOG CAP MAY2015 A0FORMAT.pdf.

Filonchyk, Mikalai, Michael P. Peterson, Lifeng Zhang, Volha Hurynovich, and Yi He. 2024. 'Greenhouse Gases Emissions and Global Climate Change: Examining the Influence of CO2, CH4, and N2O'. *Science of The Total Environment* 935 (July):173359. https://doi.org/10.1016/j.scitotenv.2024.173359.

Froeling, H.A.J., M.T. Dröge, G.F. Nane, and A.J.M. Van Wijk. 2021. 'Quantitative Risk Analysis of a Hazardous Jet Fire Event for Hydrogen Transport in Natural Gas Transmission Pipelines'. *International Journal of Hydrogen Energy* 46 (17): 10411–22. https://doi.org/10.1016/j.ijhydene.2020.11.248.

Galyas, Anna Bella, Laszlo Kis, Laszlo Tihanyi, Istvan Szunyog, Marianna Vadaszi, and Adam Koncz. 2023. 'Effect of Hydrogen Blending on the Energy Capacity of Natural Gas Transmission Networks'. *International Journal of Hydrogen Energy* 48 (39): 14795–807. https://doi.org/10.1016/j.ijhydene.2022.12.198.

GE VERNOVA 'Hydrogen for Power Generation'. Accessed 7 June 2025 https://www.gevernova.com/gas-power/future-of-energy.

Haeseldonckx, D, and W Dhaeseleer. 2007. 'The Use of the Natural-Gas Pipeline Infrastructure for Hydrogen Transport in a Changing Market Structure'. *International Journal of Hydrogen Energy* 32 (10–11): 1381–86. https://doi.org/10.1016/j.ijhydene.2006.10.018.

He, Juncai, Lin Li, Jinchao Xu, and Chunyue Zheng. 2020. 'ReLU Deep Neural Networks and Linear Finite Elements'. *Journal of Computational Mathematics* 38 (3): 502–27. https://doi.org/10.4208/jcm.1901-m2018-0160.

IChemE. 'Hydrogen Transport'. Accessed 7 June 2025. https://www.thechemicalengineer.com/features/hydrogen-transport/.

Idescat. 'Anuari Estadístic de Catalunya'. Accessed 31 May 2025. https://www.idescat.cat/indicadors/?id=aec&n=15193&t=199700&lang=en.

Inspectioneering. 2022. 'Asset Intelligence Report - A Primer on High Temperature Hydrogen Attack'. https://inspectioneering.com/airs/2022-11-09/10354/a-primer-on-high-temperature-hydrogen-attack-htha.

Isaac, Tommy. 2019. 'HyDeploy: The UK's First Hydrogen Blending Deployment Project'. *Clean Energy* 3 (2): 114–25. https://doi.org/10.1093/ce/zkz006.

Johnson, A D, H M Brightwell, and A J Carsley. n.d. 'A MODEL FOR PREDICTING THE THERMAL RADIATION HAZARDS FROM LARGE-SCALE HORIZONTALLY RELEASED NATURAL GAS JET FIRES', no. 134. https://www.icheme.org/media/12116/xii-paper-09.pdf.

Kong, Yingying, Yuxing Li, Sailei Wang, Hui Han, Pengfei Duan, Xinran Yu, and Jinke Han. 2024. 'Experimental Study on Jet Fire Characteristics of Hydrogen-Blended Natural Gas'. *International Journal of Hydrogen Energy* 49 (January):1250–60. https://doi.org/10.1016/j.ijhydene.2023.09.153.

Korb, B., S. Kawauchi, and G. Wachtmeister. 2016. 'Influence of Hydrogen Addition on the Operating Range, Emissions and Efficiency in Lean Burn Natural Gas Engines at High Specific Loads'. *Fuel* 164 (January):410–18. https://doi.org/10.1016/j.fuel.2015.09.080.

Kuczyński, Szymon, Mariusz Łaciak, Andrzej Olijnyk, Adam Szurlej, and Tomasz Włodek. 2019. 'Thermodynamic and Technical Issues of Hydrogen and Methane-Hydrogen Mixtures Pipeline Transmission'. *Energies* 12 (3): 569. https://doi.org/10.3390/en12030569.

Kurz, Rainer, Matt Lubomirsky, and Francis Bainier. 2020. 'Hydrogen in Pipelines: Impact of Hydrogen Transport in Natural Gas Pipelines'. In *Volume 9: Oil and Gas Applications; Organic Rankine Cycle Power Systems; Steam Turbine*, V009T21A001. Virtual, Online: American Society of Mechanical Engineers. https://doi.org/10.1115/GT2020-14040.

Lowesmith, Barbara Joan, and Geoffrey Hankinson. 2012. 'Large Scale High Pressure Jet Fires Involving Natural Gas and Natural Gas/Hydrogen Mixtures'. *Process Safety and Environmental Protection* 90 (2): 108–20. https://doi.org/10.1016/j.psep.2011.08.009.

Lowesmith, B.J., and G. Hankinson. 2013. 'Large Scale Experiments to Study Fires Following the Rupture of High Pressure Pipelines Conveying Natural Gas and Natural Gas/Hydrogen Mixtures'. *Process Safety and Environmental Protection* 91 (1–2): 101–11. https://doi.org/10.1016/j.psep.2012.03.004.

Luna, R. E., and H. W. Church. 1972. 'A Comparison of Turbulence Intensity and Stability Ratio Measurements to Pasquill Stability Classes', June. https://journals.ametsoc.org/view/journals/apme/11/4/1520-0450_1972_011_0663_acotia_2_0_co_2.xml.

MacGregor, Catherine. n.d. 'Key Figures as of 31 March 2025', no. 542 https://www.engie.com/.

Mashhadimoslem, Hossein, Ahad Ghaemi, Adriana Palacios, Ali Almansoori, and Ali Elkamel. 2023. 'Machine Learning Modelling and Evaluation of Jet Fires from Natural Gas Processing, Storage, and Transport'. *The Canadian Journal of Chemical Engineering* 101 (8): 4416–28. https://doi.org/10.1002/cjce.24805.

Melaina, M W, O Antonia, and M Penev. 2013. 'Blending Hydrogen into Natural Gas Pipeline Networks: A Review of Key Issues'. *Renewable Energy*. https://docs.nrel.gov/docs/fy13osti/51995.pdf.

Michał Lewak and Jarosław Tępiński. 2023. 'Application of Artificial Neural Networks for Mathematical Modelling of Horizontal Jet Fires'. *SAFETY & FIRE TECHNOLOGY* 62 (2): 34–48. https://doi.org/10.12845/sft.62.2.2023.2.

Miller, Derek. 2017. 'New Model for Predicting Thermal Radiation from Flares and High Pressure Jet Fires for Hydrogen and Syngas'. *Process Safety Progress* 36 (3): 237–51. https://doi.org/10.1002/prs.11867.

Mukherjee, Ushnik, Mohamed Elsholkami, Sean Walker, Michael Fowler, Ali Elkamel, and Amir Hajimiragha. 2015. 'Optimal Sizing of an Electrolytic Hydrogen Production System Using an Existing Natural Gas Infrastructure'. *International Journal of Hydrogen Energy* 40 (31): 9760–72. https://doi.org/10.1016/j.ijhydene.2015.05.102.

NATURALHY 'Preparing for the Hydrogen Economy by Using the Existing Natural Gas System as a Catalyst (NATURALHY) | Projekt | Fact Sheet | FP6'. n.d. CORDIS | European Commission. Accessed 19 May 2025. https://cordis.europa.eu/project/id/502661.

Pio Gianmaria, Carboni Mattia, Mocellin Paolo, Pilo Francesco, Vianello Chiara, Maschio Giuseppe, and Salzano Ernesto. 2022. 'Jet Fires of Hydrogen-Methane Mixtures'. *Chemical Engineering Transactions* 91:289–94. https://doi.org/10.3303/CET2291049.

Python. 'The Python Language Reference'. *Python Documentation*. Accessed 22 May 2025. https://docs.python.org/3/reference/index.html.

'PyTorch'. n.d. PyTorch (blog). Accessed 22 May 2025. https://pytorch.org/.

Remme, Uwe. 2024. 'Global Hydrogen Review 2024' https://www.iea.org/reports/global-hydrogen-review-2024.

Rödl, Anne, Christina Wulf, and Martin Kaltschmitt. 2018. 'Assessment of Selected Hydrogen Supply Chains—Factors Determining the Overall GHG Emissions'. In *Hydrogen Supply Chains*, 81–109. Elsevier. https://doi.org/10.1016/B978-0-12-811197-0.00003-8.

Schmura, E, M Klingenberg, and Concurrent Technologies Corporation. 2005. 'Existing Natural Gas Pipeline Materials and Associated Operational Characteristics' https://www.hydrogen.energy.gov/docs/hydrogenprogramlibraries/pdfs/progress05/v_g_1_schmura.pd f.

Speirs, Jamie, Paul Balcombe, Erin Johnson, Jeanne Martin, Nigel Brandon, and Adam Hawkes. 2018. 'A Greener Gas Grid: What Are the Options'. *Energy Policy* 118 (July):291–97. https://doi.org/10.1016/j.enpol.2018.03.069.

Sun, Yue, Jingyao Wang, Wen Zhu, Shuai Yuan, Yizhi Hong, M. Sam Mannan, and Benjamin Wilhite. 2020. 'Development of Consequent Models for Three Categories of Fire through Artificial Neural Networks'. *Industrial & Engineering Chemistry Research* 59 (1): 464–74. https://doi.org/10.1021/acs.iecr.9b05032.

Tong, Mingyu, Fuli Qin, and Jingrong Dong. 2023. 'Natural Gas Consumption Forecasting Using an Optimized Grey Bernoulli Model: The Case of the World's Top Three Natural Gas Consumers'. *Engineering Applications of Artificial Intelligence* 122 (June):106005. https://doi.org/10.1016/j.engappai.2023.106005.

Topolski, Kevin, Evan Reznicek, Burcin Erdener, Chris San Marchi, Joseph Ronevich, Lisa Fring, Kevin Simmons, Omar Fernandez, Bri-Mathias Hodge, and Mark Chung. 2022. 'Hydrogen Blending into Natural Gas Pipeline Infrastructure: Review of the State of Technology'. NREL/TP-5400-81704, 1893355, MainId:82477. https://doi.org/10.2172/1893355.

U.S. Department of Transportation 'Gas Distribution, Gas Gathering, Gas Transmission, Hazardous Liquids, Liquefied Natural Gas (LNG), and Underground Natural Gas Storage (UNGS) Annual Report

Data | PHMSA'. Accessed 8 June 2025. https://www.phmsa.dot.gov/data-and-statistics/pipeline/gas-distribution-gas-gathering-gas-transmission-hazardous-liquids.

U.S. Energy Information Administration. 2021. 'U.S. National Clean Hydrogen Strategy and Roadmap' https://www.hydrogen.energy.gov/docs/hydrogenprogramlibraries/pdfs/us-national-clean-hydrogenstrategy-roadmap.pdf?sfvrsn=c425b44f 5.

Western Australia. 2007. 1220 'Gas Exchangeability in Western Australia - Gas Quality Specifications of Interconnected Pipeline Systems'. https://www.erawa.com.au/cproot/6284/2/20071220%20Gas%20Exchangeability%20in%20Wester% 20Australia%20%20Gas%20Quality%20Specifications%20of%20Interconnected%20Pipeline%20Systems.pdf.

Zhang, Bo, Ning Xu, Haoran Zhang, Rui Qiu, Xuemei Wei, Zhuo Wang, and Yongtu Liang. 2024. 'Influence of Hydrogen Blending on the Operation of Natural Gas Pipeline Network Considering the Compressor Power Optimization'. *Applied Energy* 358 (March):122594. https://doi.org/10.1016/j.apenergy.2023.122594.

Zhang, Shuo, Yingbin Cao, Jiali Tang, Yu Zou, Huixian Shi, Ernesto Salzano, and Chao Chen. 2025. 'A Data-Driven Approach for Jet Fire Prediction of Hydrogen Blended Natural Gas Pipelines'. *Reliability Engineering & System Safety* 256 (April):110748. https://doi.org/10.1016/j.ress.2024.110748.

Zhong, Wei, Shuangli Wang, Tan Wu, Xiaolei Gao, and Tianshui Liang. 2024. 'Optimized Machine Learning Model for Fire Consequence Prediction'. *Fire* 7 (4): 114. https://doi.org/10.3390/fire7040114.

Ringraziamenti

Al termine di questo elaborato, è mio piacere dedicare uno spazio per ringraziare le persone che mi hanno sostenuto nel mio intero percorso universitario; in particolar modo in questi ultimi due anni ricchi di esperienze e di crescita.

Per prima cosa, vorrei ringraziare la mia relatrice Prof.ssa Micaela Demichela, per essere stata così gentile da accettare la mia proposta di essere seguito e rappresentato in questo lavoro.

Vorrei esprimere la mia gratitudine alla mia co-relatrice Alba Àgueda Costafreda e alla co-relatrice Artemis Papadaki per l'assistenza fornita durante tutto il lavoro dietro a questa tesi. Inoltre, desidero esprimere il mio sincero apprezzamento a tutti i membri dell'ufficio CERTEC presso l'Universitat Politècnica de Catalunya, per avermi accolto con disponibilità e calore, rendendo la mia esperienza in un ambiente di lavoro così stimolante davvero unica.

Una menzione d'onore va alla mia professoressa Stefania Specchia, che mi ha seguito durante tutto il periodo a Barcellona sempre con gentilezza e di buon grado.

Ringrazio di cuore i miei coinquilini Christine, Giancarlo, Marco, Maria e Teresa, per avermi sostenuto nei momenti quotidiani durante tutto l'anno all'estero. Grazie a loro, la convivenza in un paese nuovo è stata molto più leggera e ho riscoperto un lato di me, che temevo perduto.

Voglio esprimere la mia più profonda riconoscenza a tutti i miei colleghi, anzi a tutti i miei amici torinesi autoctoni e non, con cui ho condiviso appunti, progetti di gruppo, ma soprattutto risate ed affetto. A loro auguro i più radiosi futuri sia lavorativi che personali. Sono sicuro che le nostre strade si incroceranno di nuovo.

Un ringraziamento ai miei amici di Rovigo e dintorni: ai Latin Lover, ai Sempre Noi, agli Universitari Imbruttiti, ai compagni di Villadose e a tutti quelli che occupano un posto speciale nel cuore. È grazie a Voi se non importa in che posto mi trovi: ci sarà sempre una Casa a cui tornare.

Desidero ringraziare la mia famiglia dal profondo del cuore. Non tutte le decisioni ed i sacrifici sono stati semplici in questi anni, ma hanno permesso di raggiungere assieme, ed uniti, la soddisfazione di questo traguardo.

Infine, grazie alla mia nuova famiglia, gli *Ossos* e i *Cocos* del Rugby INEF Barcelona. Non solo mi hanno aiutato a imparare il castigliano, "i una mica de catalá", ma mi hanno accolto nella loro cultura e nella loro passione catalana.

Per ultimo, dedico tutta la mia carriera universitaria ai miei nonni, che mi hanno sempre appoggiato e protetto. Sono sicuro di averli resi orgogliosi.

Le vent se lève, il faut tenter de vivre (Paul Valéry)